

**SYNTHESIS AND GAS SORPTION STUDY OF MICROPOROUS METAL
ORGANIC FRAMEWORKS FOR HYDROGEN AND METHANE STORAGE**

by

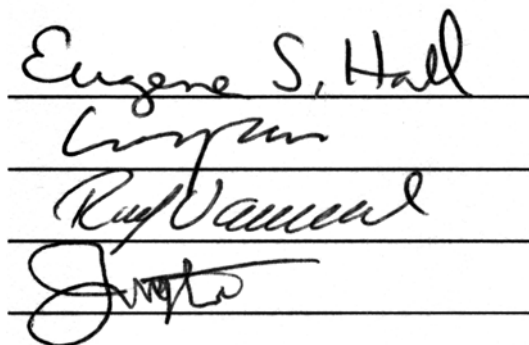
JEONGYONG LEE

A Dissertation submitted to the
Graduate School – New Brunswick
Rutgers, The State University of New Jersey
in partial fulfillment of the requirements
for the degree of
Doctor of Philosophy
Graduate Program in Chemistry and Chemical Biology

Written under the direction of

Professor Jing Li

and approved by



The block contains four handwritten signatures, each on a horizontal line. From top to bottom, the signatures are: Eugene S. Hall, Long (likely Long), Ray Vanecko, and Jing Li.

New Brunswick, New Jersey

October, 2007

ABSTRACT OF THE DISSERTATION

SYNTHESIS AND GAS SORPTION STUDY OF MICROPOROUS METAL ORGANIC FRAMEWORKS FOR HYDROGEN AND METHANE STORAGE

by

JEONGYONG LEE

Dissertation Director:

Professor Jing Li

One of the strategic goals of seeking for renewable energy sources/carriers that are clean and abundant is to replace fossil fuel with alternative fuel such as hydrogen gas. The U.S. Department of Energy has set forth specific cost and performance targets for utilizing hydrogen and natural gas for commercial purpose. In this study, a series of porous $[M(L)(P)_{0.5}]$ materials (where, $M^{2+} = \text{Zn, Co, Ni, Cu}$; L (or linker) = obba, bdc, ndc; P (or pillar) = bpy or ted) were synthesized via solvothermal reactions and evaluated on their ability of hydrogen and methane storage. By incorporating L groups with different length, microporous metal-organic framework (MOF) structures having controlled pore sizes were constructed. Single crystal X-ray diffraction study showed that they possess up to 60 % free space and the diameters of the pores are in the range of 3.5

Å ~ 9 Å. The tunable and permanent porosity and gas storage capacity of these materials were explored by low and high pressure sorption study. At low pressure high resolution argon sorption experiments revealed that these MOF materials have very high surface area, up to 3282 m²/g. The hydrogen sorption study showed that reversible hydrogen adsorption/desorption can be achieved with pore size larger than 6 Å. From the high pressure hydrogen study, a 5.48 wt% of hydrogen uptake was achieved at 77 K and ~60 bar on [Ni(ndc)(ted)_{0.5}], and 36 g/L of high volumetric density was also observed for [Zn(bdc)(ted)_{0.5}] at the same temperature and ~40 bar. The interaction between hydrogen and MOF materials was analyzed in terms of isosteric heat of adsorption. Generally, a range of 5.0 ~ 7.5 kJ/mol of heat of adsorption energy was found for the structures investigated. These findings suggest that physisorption is the primary force of hydrogen adsorption on the internal surface of MOF materials. Crystals of [Zn(bdc)(ted)_{0.5}] exhibit high methane storage capability at 298 K, as well as separation capability between hydrogen and methane gas, as several other selected MOF materials.

ACKNOWLEDGEMENTS

I would like to greatly thank Dr. Jing Li, who is my wonderful advisor, for her advice, support and careful guidance during my graduate studies. After joining her research group in August 2003, my graduate life at Rutgers was very enjoyable. Her guidance has led me to be a real scientist and independent researcher. I also gratefully thank my committee members, Dr. Gene Hall, and Dr. Ralf Warmuth, not only for serving on my thesis committee, but also for their valuable comments and constructive suggestions. I would like to express special thanks to external member, Dr. Long Pan for numerous enlightening discussions.

I also acknowledge Dr. Jacek Jagiello for helpful discussions about gas sorption measurements and Dr. Augie Venero and Mr. Marcelo Mancheno for their help in high pressure hydrogen sorption measurement. I would like to thank Dr. Thomas J. Emge and Dr. Xiaoying Huang for single crystal X-ray data collection and structure analysis. I am very happy collaborating with Dr. David H. Olson and I would like to thank him for hydrocarbon sorption data collection.

Many thanks to all my labmates; Dr. Wenhua Bi, Wooseok, Min, Princy and Ke. I specially thank to MOF subgroup fellows, Dr Kunhao Li, graduate students Sanhita, Hyuna, Gary and undergraduate student Will and Tom. It has been a pleasure to having lunch together periodically after informative subgroup discussion.

I would like to give my sincere thanks to my parents and in-law parents for their endless support, pray, love and sacrifice. I am also thankful to my brother, Jeongho and sister, Miyoung and all of my in-law brothers and sisters-in-law for their support and

love. I thank my friend JuPhil Cho for his constant friendship during initial hard time in United States. I would like to express my sincere thanks to all of *Cell-Church* friends for their support of pray and friendship.

Lastly, but most of all, I greatly thank SangSun, my wife and companion of my life, for her love, encouragement and for taking care of our lovely son YeChan and adorable daughter, June.

DEDICATION

To

My God and Families

TABLE OF CONTENTS

Abstract	ii
Acknowledgements	iv
Dedication	vi
Table of Contents	vii
List of Tables	x
List of Figures	xi
List of Acronyms	xvi
Chapter 1 Introduction	
1.1 Introduction	1
1.2 Hydrogen Storage in MOFs	4
1.3 Hydrogen Physisorption in MOFs	5
1.4. Important Characteristics of Metal-Organic Frameworks	7
1.4.1 Secondary Building Unit (SBU)	7
1.4.2 Catenation and Forbidden Catenation	9
1.5 Synthesis of MOFs	10
1.5.1 Solvothermal and Hydrothermal Reactions	12
1.5.2 Reactors for Synthesis of MOFs; Autoclave or Vial	13
1.5.3 Large Scale Synthesis of MOFs for High Pressure Gas Sorption Study	15
1.6. Literature Reviews on Hydrogen Sorption Study of MOFs	16
1.6.1 H ₂ Uptakes vs. Pore Size	16
1.6.2 H ₂ Volumetric Uptake vs. Pore Volume and Accessible Volume Fraction	18
1.6.3 H ₂ Uptake vs. Solvent Accessible Volume Fraction	18
1.6.4 H ₂ Uptakes vs. Surface Area	19
1.7 Literature Reviews on Methane Sorption Study of MOFs	20

1.8	Gas Adsorption Studies and Pore Properties of MOFs	21
1.8.1	Micropore Volume Calculation from Nitrogen and Argon Isotherms	24
1.8.2	Hydrogen Adsorption and Isothermic Heat of Adsorption, Q_{st}	26
1.9.	Research Objective	30
1.10	References	31
Chapter 2	Effect of pore size on hydrogen sorption of metal-organic frameworks at low pressure	
2.1	Introduction	38
2.2	Experimental	41
2.3	Results and Discussion	50
2.4	Conclusions	70
2.5	References	71
Chapter 3	High hydrogen adsorption capacity of $[M(bdc)(ted)_{0.5}] \cdot 2DMF \cdot 0.2H_2O$ system ($M=Zn^{2+}, Co^{2+}, Ni^{2+}, Cu^{2+}$)	
3.1.	Introduction	75
3.2	Experimental	76
3.3	Results and Discussion	79
3.4	Conclusions	90
3.5	References	91
Chapter 4	Exceptional high hydrogen uptake on microporous metal-organic frameworks and their methane storage capacity	
4.1.	Introduction	95
4.2	Experimental	97
4.2.1	Sample Preparations	97
4.2.2	Sorption Study and Experimental Conditions	106
4.3	Results and Discussion	113
4.4	Conclusions	122
4.5	References	123

Chapter 5	Summary of the Study	124
Appendices		126
Curriculum Vita		140

LIST OF TABLES

Table 1.1	Technical Targets of On-board Hydrogen Storage Systems by DOE	4
Table 1.2	Summary of Selected Hydrogen sorption studies	17
Table 1.3	The conversion factor between Liquid and Gas	26
Table 3.1	TGA results of $[M(\text{bdc})(\text{ted})_{0.5}] \cdot 2\text{DMF} \cdot 0.2\text{H}_2\text{O}$	84
Table 3.2	Porosity of $[M(\text{bdc})(\text{ted})_{0.5}]$ based on Ar sorption isotherm at 87 K	85
Table 3.3	The Q_{st} results of $[M(\text{bdc})(\text{ted})_{0.5}] \cdot 2\text{DMF} \cdot 0.2\text{H}_2\text{O}$	87
Table 4.1	Simulated peak position data of 12 by PXRD refinement	103
Table 4.2	Summary of the pore properties of argon and hydrogen sorption at low pressure and cryogenic temperatures	107
Table 4.3	The hydrogen uptake at elevated pressure and different temperatures	113

LIST OF FIGURES

Figure 1.1	An example of metal-organic framework structure of $[\text{Zn}(\text{bdc})(\text{ted})_{0.5}]$ and its pore (orange ball). In the figure, green denote Zn metal, O is red, C is gray and N is blue	3
Figure 1.2	Selected examples of SBUs (a, b, c) and their framework connectivity (a', b', c'). (a) $\text{Cu}_2\text{O}_2(\text{CO}_2)_4$ paddlewheel within $[\text{Cu}_3(\text{btc})_2(\text{H}_2\text{O})_3]_n$ or Cu-BTC (b) square $\text{Zn}_4\text{O}(\text{CO}_2)_6$ in MOF-5 (c) cubic $\text{Zn}_8(\text{SiO}_4)(\text{CO}_2)_{12}$ clusters in $[\text{Zn}_8(\text{SiO}_4)(\text{bdc})_6]_n$	8
Figure 1.3	Reduction of pore space by catenation; interpenetration results in minimizing pore size and interweaving with thickening pore walls may increase rigidity and thermal stability	9
Figure 1.4	(a) The SBU of an infinite Zn-OH-(2Zn)-OH-Zn chain, (b) the forbidden catenation structure $[\text{Zn}_3\text{O}(\text{OH})_2(\text{bpdc})_2] \cdot 4\text{DEF} \cdot 2\text{H}_2\text{O}$, (c) catenated 3D $[\text{Zn}_4\text{O}(\text{bpdc})_3] \cdot 7\text{DEF} \cdot 4\text{H}_2\text{O}$ and (d) noncatenation structures of 3D $[\text{Zn}_4\text{O}(\text{bpdc})_3] \cdot 12\text{DEF} \cdot \text{H}_2\text{O}$	11
Figure 1.5	The vial reaction and its recrystallization procedure to grow single crystals. Without opening the reaction vessel, the quality of the product can be examined under the microscope	14
Figure 1.6	The gravimetric H_2 uptake (left) and volumetric H_2 uptake (right) as a function of pore diameter	16
Figure 1.7	The volumetric H_2 uptake properties as a function of pore volume (left) and accessible volume fraction (right)	18

Figure 1.8	The gravimetric H ₂ uptake properties as a function of accessible volume fraction	18
Figure 1.9	The H ₂ uptake properties as a function of surface area in gravimetric scale (left) and in volumetric scale (right)	19
Figure 1.10	IUPAC classification of sorption isotherm types	22
Figure 1.11	(a) A set of H ₂ isotherms obtained at 77 K and 87 K for [Zn ₃ (bpdc) ₃ (bpy)] are used to find pressures p ₁ and p ₂ , (b) A plot of isosteric heat of adsorption, Q_{st} as a function of the H ₂ uptake	29
Figure 2.1	Top: The Zn ₃ unit of 1 . The two terminal (outer) Zn have a tetrahedral coordination sphere (Zn1) and the center Zn (Zn2) has an octahedral coordination sphere. Bottom: The Co ₃ unit of 2 . The two outer Co (Co1) have a trigonal bipyramidal coordination sphere, and the center Co (Co2) has an octahedral coordination sphere. Zn (green) and Co (pink), O (red), N (blue), C (gray), and H (white)	42
Figure. 2.2	Top: View of Structure 1 showing 1D channels. Bottom: View of Structure 2 showing the similar channels	44
Figure 2.3	The Ar adsorption (blue) and desorption (red) isotherms on 1 and 2 obtained at 87 K (a) in V (STP, cc/g) condition and (b) in V (Liq, cc/g) in the range of $0.3 < P/P^\circ < 0.8$ for pore volume calculation	52
Figure 2.4	(a) Pore size distribution of [Zn ₃ (bpdc) ₃ bpy] (1) and [Co ₃ (bpdc) ₃ bpy] (2) calculated from Horvath-Kawazoe (H-K) Model and (b) their hydrogen adsorption isotherms at 77 K and 87 K	54

Figure 2.5	Isosteric heat of H ₂ adsorption for 1 and 2 , respectively, as a function of the amount of hydrogen adsorbed	56
Figure 2.6	(a) The SBU (top) and three dimensional (3D) ultramicrochannel structure (bottom) of Cu(hfipbb)(H ₂ hfipbb) _{0.5} (3). In the figure, Cu is shown in cyan, F is shown in green, O is shown in red, C is shown in gray and H is omitted for clarity. (b) The Argon isotherm at 87 K and (c) hydrogen adsorption-desorption isotherms on 3 at 87 K	58
Figure 2.7	(a) The view of 1D open channel of 4 . along with crystal axis a (left) and axis b(right) In the figure, Zn is shown in green, N is shown in blue, O is shown in red, C is shown in gray and H is omitted for clarity. (b) The argon isotherm at 87K and (c) The hydrogen adsorption-desorption isotherms on [Zn ₂ (obba) ₂ (bpy)] (4) at 77 K and 87 K	61
Figure 2.8	The crystal structure of Cu ₃ (BTC) ₂ (H ₂ O) ₃ (5)	64
Figure 2.9	(a) The argon adsorption (Blue)-desorption(Red) isotherms of 5 at 87K and (b) HK pore size distribution showed two different size of pores	65
Figure 2.10	The hydrogen adsorption-desorption isotherms on 1-2 and 4-7 at 77 K. All solid marks of each isotherm denote adsorption and empty marks represent desorption	67
Figure 2.11	The adsorbed hydrogen density on 1-2 and 4-7 at 77 K. All solid marks of each isotherm denote adsorption and empty marks represent desorption	69
Figure 3.1	Views of the crystal structure of [M(bdc)(ted) _{0.5}] \cdot 2DMF \cdot 0.2H ₂ O (M = Zn, Co, Ni and Cu)	81

Figure 3.2	PXRD patterns of 8 ~ 11 (Zn, Co, Ni, Cu order from top to bottom) compared with the simulated pattern from the single crystal data of 8	83
Figure 3.3	The HK Pore size distribution for 8 ~ 11 calculated from Ar sorption isotherms at 87 K	86
Figure 3.4	(a) Hydrogen sorption isotherms of 8-11 at 77 K (solid marks for adsorption and open marks for desorption) and (b) Isosteric heat of adsorption, Q_{st} as a function of hydrogen loading	89
Figure 4.1	The photograph of green crystal of $[\text{Ni}(\text{ndc})(\text{ted})_{0.5}] \cdot 3\text{DMF} \cdot \text{H}_2\text{O}$ was taken under microscope with polarized light	101
Figure 4.2	The simulated powder X-ray diffraction pattern of $[\text{Ni}(\text{ndc})(\text{ted})_{0.5}] \cdot 3\text{DMF} \cdot \text{H}_2\text{O}$ (12) in a 2θ range of $3 \sim 50^\circ$	102
Figure 4.3	The PXRD pattern of $[\text{Ni}(\text{ndc})(\text{ted})_{0.5}] \cdot 3\text{DMF} \cdot \text{H}_2\text{O}$ depends on experimental stages	104
Figure 4.4	The TG and derivative curve of $[\text{Ni}(\text{ndc})(\text{ted})_{0.5}] \cdot 3\text{DMF} \cdot \text{H}_2\text{O}$ (12)	105
Figure 4.5	Effect of sample shape on hydrogen isotherm on $[\text{Zn}(\text{bdc})(\text{ted})_{0.5}]$ at 77 K	110
Figure 4.6	Effect of equilibrium time on hydrogen isotherm on Cu-BTC (top) and $[\text{Ni}(\text{ndc})(\text{ted})_{0.5}]$ (bottom) at elevated pressure	112
Figure 4.7	High pressure hydrogen isotherms at 77 K on selected MOF materials in gravimetric scale (wt%) as a function of pressure	114

Figure 4.8	High pressure hydrogen adsorption isotherms at 77 K on selected MOF materials in volumetric uptake (g/L) as a function of pressure	116
Figure 4.9	High pressure hydrogen adsorption isotherms at 298 K on selected MOF materials in gravimetric scale (wt%) as a function of pressure	118
Figure 4.10	High pressure dihydrogen sorption at 77 K as a function of the number of adsorption/desorption cycles	119
Figure 4.11	High pressure methane isotherms at 298 K in volumetric scale (STP, cc/g, top) and their separation capability (mg/g, bottom)	121
Figure 5.1	The summary of correlation between hydrogen uptake, pore size and surface area based on argon sorption studies at 87 K and high pressure hydrogen studies at 77 K	125

LIST OF ACRONYMS

bdc	benzene-1,4-dicarboxylate
BET	Brunauer-Emmett-Teller
bpdc	biphenyldicarboxylate,
bpy	4,4'-bipyridine
btc	benzene-1,3,5-tricarboxylate
DCM	dichloromethane
DEF	<i>N,N</i> -diethylformamide
DMA	<i>N,N</i> -dimethylethanamide
DMF	<i>N,N</i> -dimethylformamide
DOE	(United States) Department of Energy
EA	Elemental analysis
GFMOF	Guest free metal-organic framework
hfipbb	4,4'-(hexafluoroisopropylidene)-bis(benzoic acid)
MOF	Metal-organic framework
ndc	naphthalene-2,6-dicarboxylate
obba	4,4'-oxybisbenzoic acid
PXRD	Powder X-ray diffraction
RPM	Recyclable Rutgers Porous Material
SBU	Secondary building unit
tbip	5-tert-butylisophthalic acid
ted	triethylenediamine

TGA	thermogravimetric analysis
VDW	van der Waals

CHAPTER ONE

INTRODUCTION

1.1 Introduction

Metal-Organic Frameworks (MOFs) have been widely studied due to their fundamental importance and versatile application potential, such as gas separation and catalysis,¹⁻⁴ sensing devices,^{5, 6} ion exchange^{7, 8} optoelectronics^{9, 10} and negative thermal expansion.¹¹ Recently, there has been an increasing interest in utilizing MOF materials for on-board hydrogen storage.^{12, 13} As hydrogen has a very low gravimetric and volumetric density, it remains a great challenge to develop porous materials that are suitable for use as hydrogen storage media.

Metal-organic framework structures are composed of metals (as nodes) and ligands (as linkers) which form extended networks via coordinate bonds (Figure 1.1). These materials have been described in different terms such as coordination polymers¹⁴⁻¹⁶, hybrid organic-inorganic materials¹⁷, organic zeolite analogues² and metal-organic frameworks^{18, 19}. Each has its own focusing point. For example, the use of “coordination polymer” emphasizes the nature of bonding. On the other hand, “metal organic framework” stresses the composition.

The one-dimensional (1D), two-dimensional (2D)^{20, 21} or three-dimensional (3D) metal organic framework structures built by linking linear or nonlinear organic linkers and metal clusters^{16, 22-25} often lead to open voids that can hold molecules so called “*guest molecules*”. They are conventionally denoted outside of the bracket in the structural formula, e.g. in the $[\text{Zn}(\text{bdc})(\text{ted})_{0.5}] \cdot 2\text{DMF} \cdot 0.2\text{H}_2\text{O}$, the framework is $[\text{Zn}(\text{bdc})(\text{ted})_{0.5}]$ and it holds two DMF molecules and 0.2 water molecule as guest molecules within its pores. Most porous MOFs have their pore diameters less than 2 nm, and are said to be micropores. The most advantageous features of these materials are: well-characterized pores, small pore diameter, high micropore volume, and high surface area. Their pore structure can often be modified not only to adjust pore size and/or shape but also to enhance sorbate-sorbent interactions.

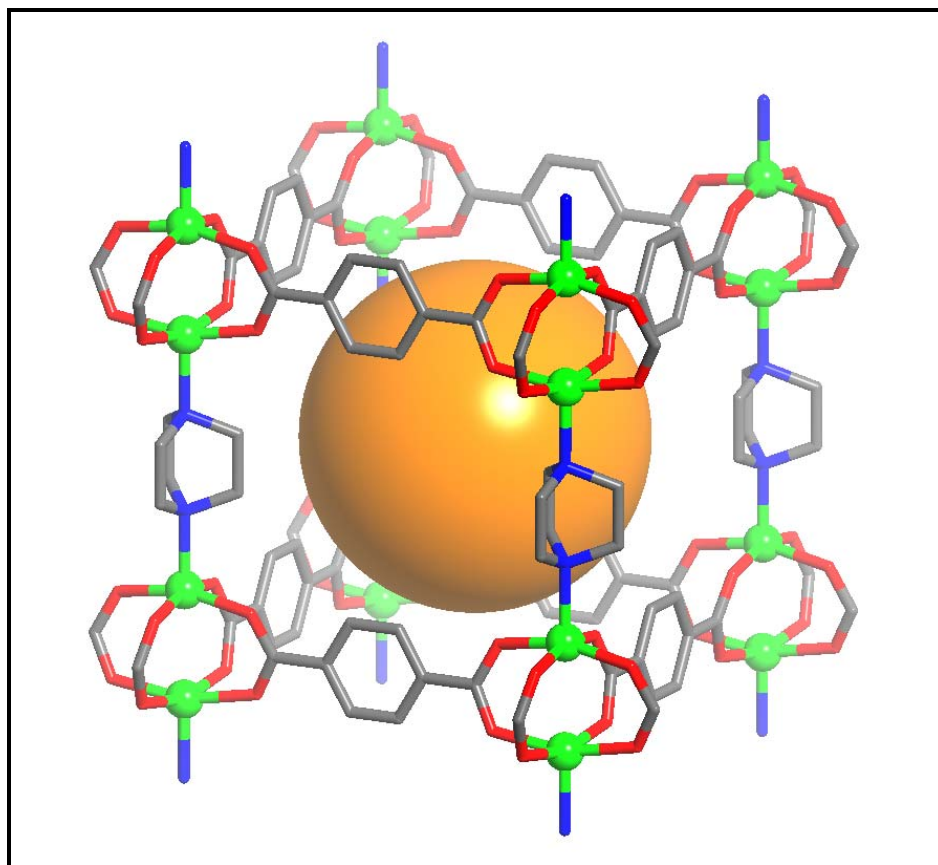


Figure 1.1 An example of metal-organic framework structure of $[\text{Zn}(\text{bdc})(\text{ted})_{0.5}]$ and its pore (orange ball). In the figure, green denote Zn metal, O is red, C is gray and N is blue.

1.2 Hydrogen Storage in MOFs

Hydrogen is an abundant and promising renewable energy carrier which can be used as an alternative fuel for transportation. Due to its very low boiling point, 20K, it can be stored in a liquid state at very low temperature or at high pressure. To achieve sufficient storage efficiency, the U.S. Department of Energy (DOE) has set targets, summarized in Table 1.1, for on-board hydrogen storage systems of 6 wt% and 45 g/L by year 2010 and 9 wt% and 81 g/L by year 2015 at ambient temperatures to enable a driving range of greater than 300 miles.

At the present time, conventional hydrogen storage methods include liquefaction of H₂ gas at -253°C or compression of H₂ gas with extremely high pressure, 350 atm or higher. However, these methods have critical disadvantages, such as very low efficiency of liquefaction and safety issues of compression, which make it difficult for them to become economically practical.²⁶⁻²⁸ Therefore, developing an effective and safe hydrogen storage method is required for hydrogen fuel cell technology.

Table 1.1 Technical Targets of On-board Hydrogen Storage Systems by DOE²⁹

Storage Parameter	Units	2007	2010	2015
System Gravimetric Capacity	kg H ₂ /kg	0.045	0.06	0.09
System Volumetric Capacity	kg H ₂ /L	0.036	0.045	0.081
Operating ambient temperature	°C	-20/50	-30/50	-40/60
Cycle Life	cycles	500	1000	1500
Max delivery pressure from tank	atm	100	100	100
System Fill Time (for 5kg)	min	10	3	2.5
Fuel Purity (H ₂ from Storage)	% H ₂	99.99 (dry basis)		

1.3 Hydrogen Physisorption in MOFs

Depending on the characteristics of the interaction between gas (hydrogen or methane) and porous solid materials (MOFs) or between gases, all adsorption processes can be grouped into two categories, physisorption or chemisorption. The bonding strength of physical adsorption is much weaker than that of the chemical sorption which is achieved through formation of chemical bonds. Due to the fact that physisorption is accompanied by low heats of adsorption, no disruptive structural changes occur at the surface during the adsorption process.

The distinctive feature of physical adsorption is that hydrogen molecules keep their molecular identity and unlike chemical sorption, multilayer coverage at the surface can take place. As the strength of the interaction of adsorbate/adsorbent is higher than that of adsorbate/adsorbate, the magnitude of the heat of adsorption is always monotonically decreased as the uptake amount of gas increases and physical adsorption is expected to be fully reversible due to the low heat of adsorption.

Great efforts to improve storage efficiency have led to important developments in metal hydrides.^{30, 31} In a metal hydride, hydrogen adsorption occurs on the surface of metals or alloys, at which point it dissociate into two atoms. The dissociation of molecular hydrogen results in chemical bonding between hydrogen and the metal or alloy and the formation of metal hydride. Relatively high hydrogen uptakes can be achieved in metal hydrides, however, the hydrogen release, desorption, process is very slow and generally requires high temperatures. That is the main drawback of these materials and the cycling capacity must be improved before this method can be used commercially.

The fast hydrogen release can be achieved with metal organic frameworks.^{32, 33} As the hydrogen is adsorbed by physisorption on the internal surface of MOFs, the molecular identity of hydrogen is retained. The desorption process of hydrogen is reversible under mild conditions. The adsorption studies on MOFs have shown that often there is a correlation between surface area and hydrogen uptake.

A number of investigations have been conducted to analyze the hydrogen binding sites in MOFs.³⁴⁻³⁹ Neutron scattering experiments on selected MOFs have allowed for the direct observation of hydrogen binding sites. The results demonstrate that there are two possible binding sites in $[\text{Zn}_4\text{O}(\text{bdc})_3]\cdot 7\text{DEF}\cdot 3\text{H}_2\text{O}$ or MOF-5 (bdc = benzenedicarboxylate); open metal sites and organic linkers. The Fourier-difference scattering-length density data clearly show that the H_2 molecules are located around metals. The hydrogen binding sites are indicated by different color regions, such as red, yellow and green. Amazingly MOF-5 is predicted to be capable of taking up to 11 wt% of hydrogen at low temperature.³⁷

Based on these data, several approaches are proposed to increase binding energy. As one hydrogen molecule can only interact with one organic linker in a large single pore, hydrogen binding power may be increased by having multiple number of smaller pores, thus allowing multiple interactions between single hydrogen molecule and aromatic ligands.^{13, 40} Therefore, a larger number of small pores are preferred over a small number of extremely large pores. With the advantages of fast hydrogen uptake/release and other characteristics mentioned above, highly porous MOFs are now being studied intensively to achieve the DOE targets.

Some promising results have been published for hydrogen storage with MOFs. In 2006, 7.5 wt% and 32 g/L of hydrogen uptake in porous $[\text{Zn}_4\text{O}(\text{btb})_2](\text{DEF})_{15}(\text{H}_2\text{O})_3$ or MOF-177 (btb=1,3,5-benzenetribenzoate, DEF=*N,N*-Diethylformamide) at 77 K and ~70 bar was reported by Wong-Foy et al.⁴¹ In addition, Yang and his coworkers reported enhancement of hydrogen uptake by the spillover method at room temperature.^{42, 43}

1.4. Important Characteristics of Metal-Organic Frameworks

In order to design and predict the structures of MOFs, it is essential to understand how the frameworks are constructed and how they achieve the structural stability.

1.4.1 Secondary Building Unit (SBU)

Most of the porous MOFs are built upon metal clusters, so called Secondary Building Units (SBUs). The SBUs serve as “nodes” and coordinate to organic linkers to form frameworks. Some examples of SBUs are drawn in Figure 1.2.^{32, 44, 45} It is a metal cluster connected by organic linkers. Examples of metal clusters include two metal cations and organic linkers as in Figure 1.2a, or four metal cations and linkers as in Figure 1.2b, or eight metal cations and linkers as in Figure 1.2c. Because of the large size of SBUs, the resultant structures of MOFs are usually porous and could have relatively large pores.⁴⁴⁻⁴⁶ Pore size can also be modified by introducing different length organic linkers, in general, longer and linear ligands give rise to frameworks with less stability. Notably, the cubic $\text{Zn}_8(\text{SiO}_4)(\text{CO}_2)_{12}$ clusters in Figure 1.2c' are connected via double organic linkers. As the frameworks of Figure 1.2c' were reinforced by doublet ligands, this material is significantly stabilized, stable to 500°C.⁴⁵

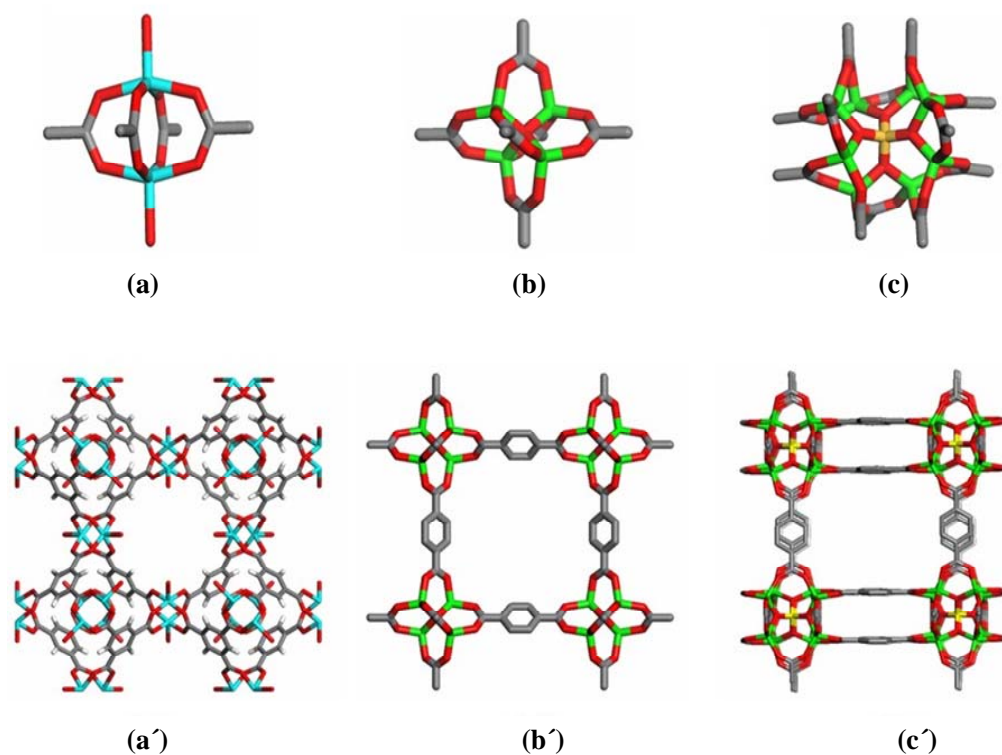


Figure 1.2 Selected examples of SBUs (a, b, c) and their framework connectivity (a', b', c'). (a) $\text{Cu}_2\text{O}_2(\text{CO}_2)_4$ paddlewheel within $[\text{Cu}_3(\text{btc})_2(\text{H}_2\text{O})_3]_n$ or Cu-BTC (b) square $\text{Zn}_4\text{O}(\text{CO}_2)_6$ in MOF-5 (c) cubic $\text{Zn}_8(\text{SiO}_4)(\text{CO}_2)_{12}$ clusters in $[\text{Zn}_8(\text{SiO}_4)(\text{bdc})_6]_n$. The compound is stable up to 500°C . The SBUs shown in (b) and (c) form vertices of cubes in (b') and (c'). Cyan Cu, Green Zn, Yellow Si, Gray C and Red O. (btc=1,3,5-benzenetricarboxylate)

1.4.2 Catenation and Forbidden Catenation

The use of long linkers to create larger pores may result in catenation. In such a case, two or more identical nets were formed in the open space of the other nets. Some examples of catenation are interpenetration and interweaving, as shown in Figure 1.3. The maximum displacement refers to “*interpenetration*” and the minimal displacement, “*interweaving*”.⁴⁷ As interpenetration reduces pore space, and thus, highly catenulate structures have low porosity. For this reason, multi-fold interpenetration has been a major obstacle in obtaining MOFs with high porosity. Although interweaving also results in reduced pore volume, the degree of such reduction is relatively small, and it is believed that interweaving can increase thermal stability of the frameworks by reinforce wall thickness.^{46, 48-50}

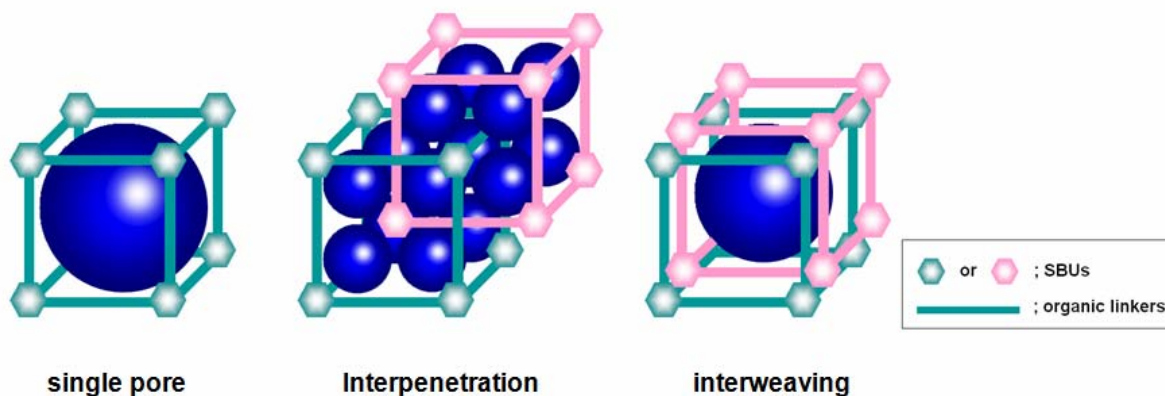


Figure 1.3 Reduction of pore space by catenation; interpenetration results in minimizing pore size and interweaving with thickening pore walls may increase rigidity and thermal stability.

Catenation may be prevented via several routes. One way is to construct 1D infinite chain SBU that forbid catenation. One nice example of this is the synthesis of $[\text{Zn}_3\text{O}(\text{OH})_2(\text{bpdc})_2] \cdot 4\text{DEF} \cdot 2\text{H}_2\text{O}$ or MOF-69A (bpdc = biphenyldicarboxylate) and

$[\text{Zn}_3\text{O}(\text{OH})_2(\text{ndc})_2]\cdot 4\text{DEF}\cdot 2\text{H}_2\text{O}$ or MOF-69B (ndc = 2,6-naphthalenedicarboxylate).⁵¹ The structure and topology of the 1D infinite chain SBU (Figure 1.4a) in the isostructural MOF-69A and B make the catenation impossible, thus leading to “forbidden catenation” structures (Figure 1.4b).

The exactly same 1D infinite chain SBU (Figure 1.4a) was observed on one of our unpublished crystal structures, $[\text{Zn}_{4.5}(\text{bdc})_3(\text{OH})_3]\cdot 3\text{DEF}$ (Reaction Code was YL1-86C). The 3 to 1 molar ratio of metal to ligand resulted in the SBU of $\text{Zn}_4\text{O}(\text{CO}_2)_6$ (Figure 1.2b), while a 3 to $0.7 \sim 0.3$ of metal to ligand molar ratio lead to infinite 1D chain SBU of Zn-OH-(2Zn)-OH-Zn like in Figure 1.4a. In addition, it is possible to make non-catenation structure via controlling the molar ratio by adding more ligands.^{50, 52}

Another reported example non-catenation structure was achieved by controlling the ratio of solutes to solvent in the Zn-bpdc system.^{19, 51} From the catenation structure of 3D $[\text{Zn}_4\text{O}(\text{bpdc})_3]\cdot 7\text{DEF}\cdot 4\text{H}_2\text{O}$ or IRMOF-9 (Figure 1.4c),¹⁹ a non-catenation 3D structure of $[\text{Zn}_4\text{O}(\text{bpdc})_3]\cdot 12\text{DEF}\cdot \text{H}_2\text{O}$ with the same framework (IRMOF-10, Figure 1.4d) can be achieved simply through a diluted reaction by adding more solvent.¹⁹ The only difference in the two structures is the amount of guest molecules due to the different sizes of their pores.

1.5 Synthesis of MOFs

Some reaction parameters are needed to be considered in order to reproduce the MOF materials. They are composition of the reactants, pH, reaction temperatures, time, and solubility. Most of the dicarboxylic acids used in MOF synthesis are first dissolved in a suitable solvent to be deprotonated before they can form bonds with metal cations.

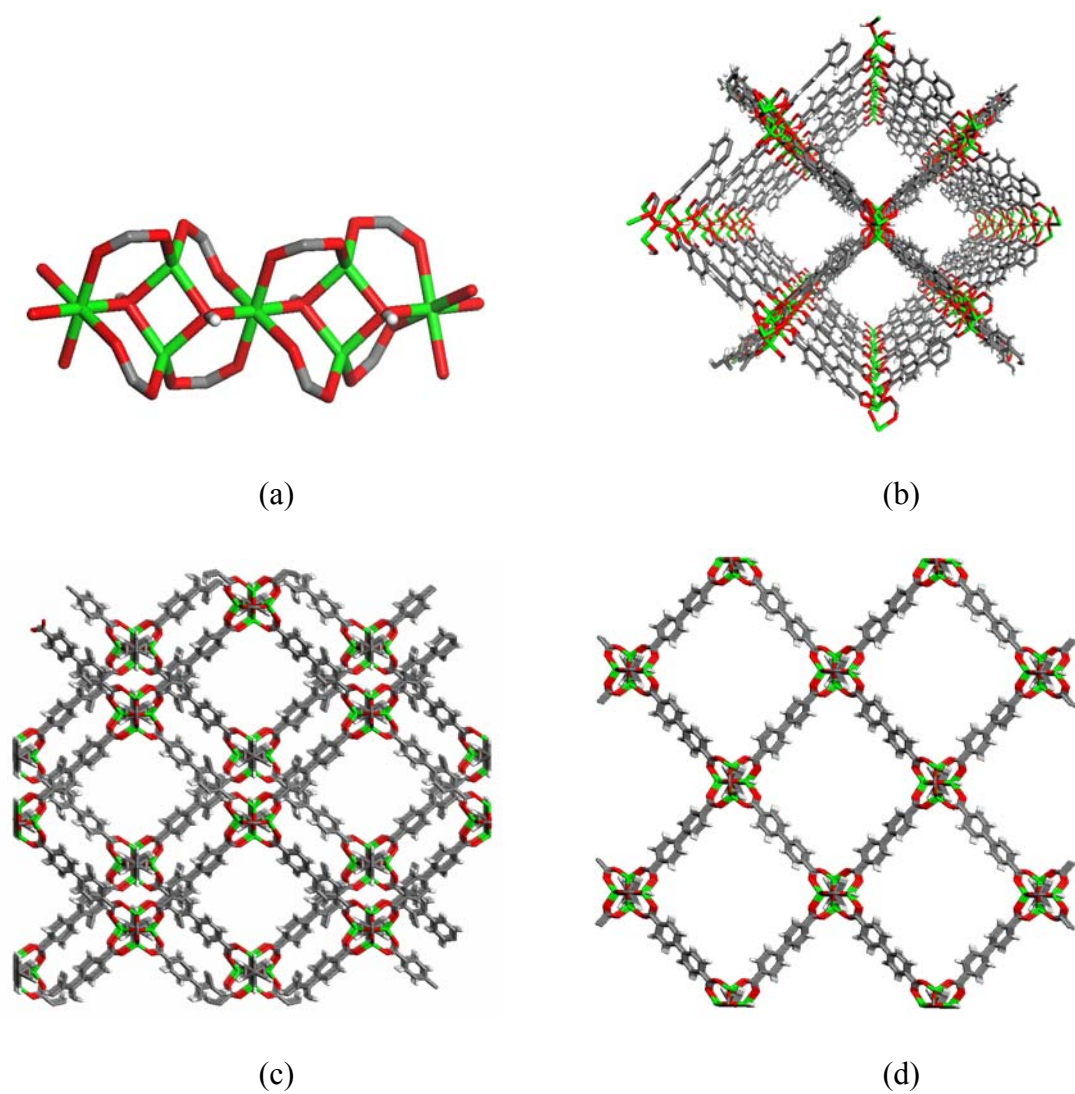


Figure 1.4 (a) The SBU of an infinite Zn-OH-(2Zn)-OH-Zn chain,⁵³ (b) the forbidden catenation structure $[\text{Zn}_3\text{O}(\text{OH})_2(\text{bpdc})_2] \cdot 4\text{DEF} \cdot 2\text{H}_2\text{O}$, (c) catenated 3D $[\text{Zn}_4\text{O}(\text{bpdc})_3] \cdot 7\text{DEF} \cdot 4\text{H}_2\text{O}$ ¹⁹ and (d) noncatenation structures of 3D $[\text{Zn}_4\text{O}(\text{bpdc})_3] \cdot 12\text{DEF} \cdot \text{H}_2\text{O}$ ¹⁹ (Zn in Green, O in red, N in Blue and H in white)

The deprotonation results in a decrease in pH and makes the solution acidic after the reaction. If the reactant mixture is too acidic, reaction may not proceed because the deprotonation of the carboxylic acid would be prohibited. Also, as mentioned earlier, changes in molar ratio of the reactants often give rise to structures with different connectivity and properties.

1.5.1 Solvothermal and Hydrothermal Reactions

The synthesis of MOFs can be carried out by solvothermal reaction, or hydrothermal reaction. Solvothermal reactions involve the use of a solvent (organic or inorganic) at elevated temperatures and pressures in a closed system, often in the vicinity of its critical point.⁵⁴⁻⁵⁷ When water is used as a solvent, the reactions are referred to as hydrothermal. Under solvo(hydro)thermal conditions, certain properties of the solvent, such as density, viscosity and diffusion coefficient change dramatically and the solvent behaves much differently from what is expected at ambient conditions. Consequently, the solubility, the diffusion process and the chemical reactivity of the reactants (usually solids) are greatly increased or enhanced, which enables the reactions to take place at a much lower temperature.⁵⁶ Selection of the solvent is very important, because some metal sources and organic linkers have very low solubility or are even insoluble. In order to increase the solubility, two or three solvents can be mixed or another solvent may be added to increase solubility. For example, $-\text{SiO}_4$ was incorporated in a Zn-dicarboxylate structure (Figure 1.2c and 1.2c') to improve its thermal stability. In order to accomplish this, NaOH was added to dissolve sodium metasilicate, $\text{Na}_2\text{SiO}_3 \cdot 9\text{H}_2\text{O}$, which is soluble only in NaOH.

In most of these reactions, reactants were dissolved or partially dissolved in the beaker by adding more fresh solvent and by ultrasonic treatment in a warm tap water bath before transferring them into reaction vessels.

1.5.2 Reactors for Synthesis of MOFs; Autoclave or Vial

Teflon-lined autoclaves or glass vials are often used as reaction vessels. Autoclaves are good for reactions at relative high temperatures (above 150°C), while vials can be used at relative low temperatures and for reactions that are not sensitive to air. By using vials as reaction vessel, we can physically observe reactions occurring in real time.

It is useful to have the capability of monitoring a reaction and to seek the best reaction conditions, such as time and temperature. For reaction setup and recrystallization of the products, vials have an advantage compared to an autoclave. The vial reaction setup and recrystallization procedures are described in Figure 1.5. In addition, the products can be examined under a microscope while being kept inside the vial, thus are free from contamination. Using vials is convenient to mix the reactants and treat the mixture by ultrasonic radiation to maximize their solubility around 50°C of water bath.

After a reaction is completed at certain temperature, four different situations may result, as shown in Figure 1.5 in the case of 1-4. The case 1 is the best when single crystals of suitable sizes result after the first trial reaction. However, the recrystallization process is required to obtain suitable crystals for Case 2 and 3, and it can be achieved by a slow evaporation of the solvents. It typically takes from a week to a couple of months. Detail procedures of syntheses will be given in each section.

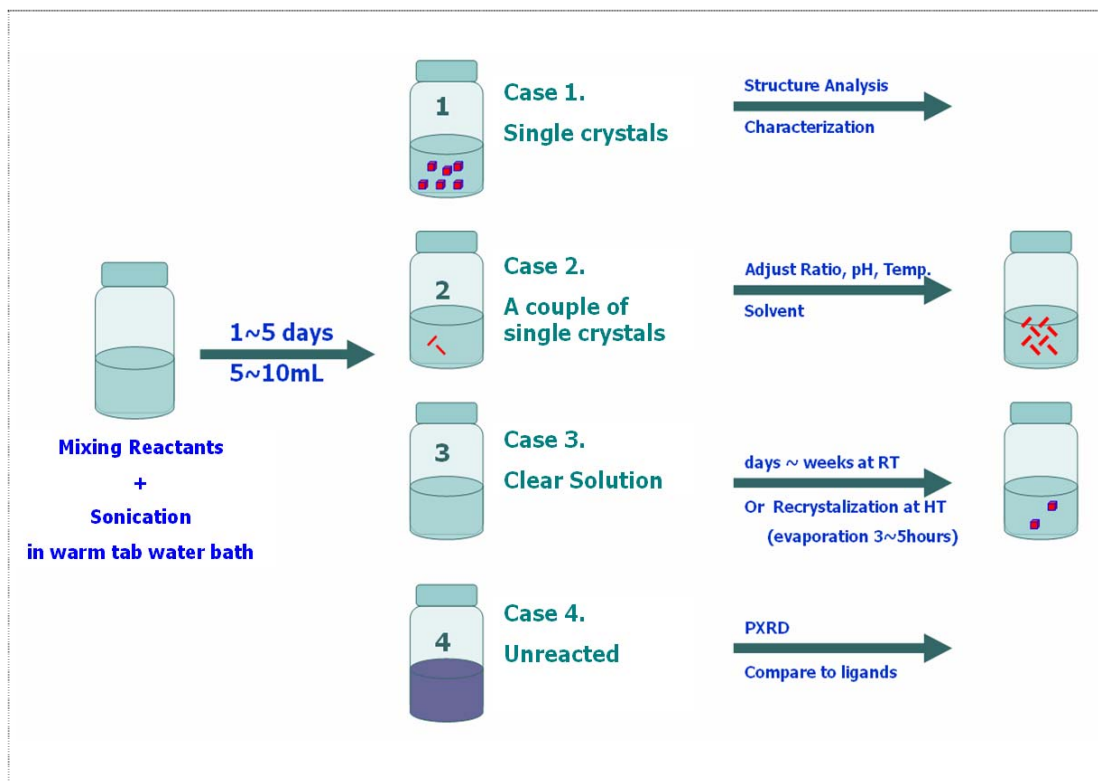


Figure 1.5 The vial reaction and its recrystallization procedure to grow single crystals. Without opening the reaction vessel, the quality of the product can be examined under the microscope.

1.5.3 Large Scale Synthesis of MOFs for High Pressure Gas Sorption Study

A relatively large sample amount, typically 300 mg ~ 800 mg (guest molecules removed), is required to insure reasonable and reproducible data for high pressure sorption studies.

It was observed that the reactant solubility is an important factor to achieve pure samples at the gram scale. Typically, the reactants were dissolved in the solvent in a beaker. Subsequently the mixture was sonicated in the warm water bath (50~60°C) until all solid particles had disappeared followed by adding more solvents and/or nitric acid to get a clear solution. Then, the mixture was transferred into either a reaction bottle or a Teflon-lined autoclave for further reaction.

1.6 Literature Reviews on Hydrogen Sorption Study of MOFs

Much research prior to this work has been conducted on hydrogen sorption and the results, and are summarized in Table 1.2. The hydrogen uptakes are analyzed as a function of pore size, free pore volume and surface area.

1.6.1 H₂ Uptakes vs. Pore Size

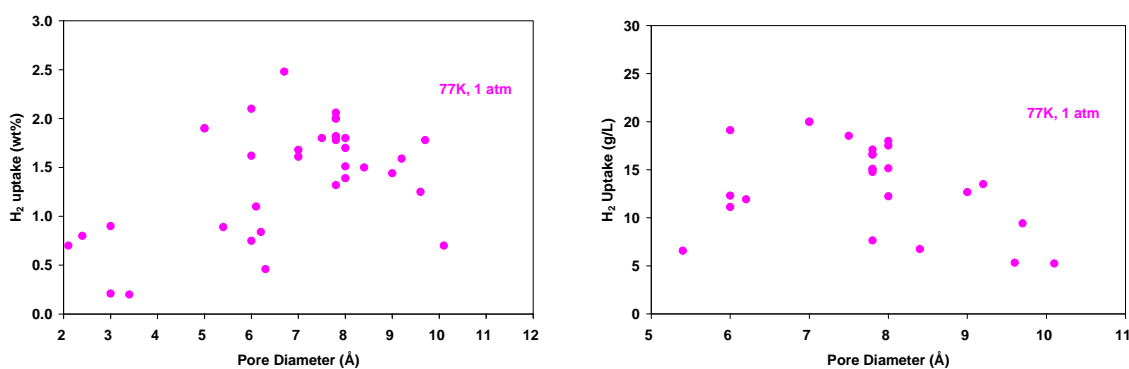


Figure 1.6 The gravimetric H₂ uptake (left) and volumetric H₂ uptake (right) as a function of pore diameter

Based on the data available, it is found that at 77 K and low pressure (1 atm) in general, there is no trend in the hydrogen uptake (gravimetric density or wt%) as pore size increases (Fig. 1.6, left). However, the volumetric uptake of adsorbed hydrogen (g/L, Fig. 1.6, right) increases for pore diameters (5-7 Å) then decreases with larger pore size (7 Å <) at 77 K and 1 atm.

Table 1.2 Summary of Selected Hydrogen sorption studies

Material	[1] Free / fixed diameters	[2] Pore volume [cm ³ /g]	Accessible volume fraction ^[3]	Apparent surface area ^[4] [m ² /g]	H ₂ uptake [wt%]	Conditions	[5] H ₂ Uptake [g/L]	Refs.
Zn ₄ O(bdc) ₃ , IRMOF-1	7.8 / 15.2	1.19	0.59	3362	1.32	77K, 1atm	8	58, 59
Zn ₄ O(bdc) ₃ , IRMOF-1	/ 15.2	1.19	0.59		1.00	RT, 20 bar	6	32
Zn ₄ O(bdc) ₃ , IRMOF-1	/ 15.2	1.19	0.59		1.65	RT, 48 atm	10	13
Zn ₄ O(R ⁶ -bdc) ₃ , IRMOF-6	5.9 / 15.2	0.93	0.50	2636	1.00	RT, 10 bar	7	19, 32
Zn ₄ O(ndc) ₃ , IRMOF-8	8.4 / 18.0	0.52	0.66	1466	1.50	77K, 1atm	7	58
Zn ₄ O(ndc) ₃ , IRMOF-8	/	0.52			2.00	RT, 10 atm	9	19
Zn ₄ O(hpdc) ₃ , IRMOF-11	6 / 12.4	0.68	0.40	1911	1.62	77K, 1atm	12	58
Zn ₄ O(tmbdc) ₃ , IRMOF-18	5.4 / 13.8	0.53	0.42	1501	0.89	77K, 1atm	7	58
Zn ₄ O(bt) ₂ , MOF-177	9.6 / 11.8	1.61	0.63	4526	1.25	77K, 1atm	5	58
Al(OH)(bdc), MIL-53(Al)	6.4 / 6.4		0.29	1,590	3.80	77K, 16 bar		60
Cr(OH)(bdc), MIL-53(Cr)	6.6 / 6.6		0.29	1,590	3.10	77K, 16 bar		60, 61
Mn(HCO ₂) ₂	3 / 4.7		0.10	297	0.90	77K, 1atm		12
Cu ₂ (hfipbb) ₂ (H ₂ hfipbb)	4 / 5.7	0.07			0.21	77K, 1atm		62
Cu ₂ (hfipbb) ₂ (H ₂ hfipbb)	3 / 4.7	0.07	0.03		1.00	RT, 48 atm		13
Ni(cyclam)(bpydc)	6.1 / 7.6	0.33	0.18	817	1.10	77K, 1atm		15
Zn ₂ (bdc) ₂ (dabco)	7.8 / 9.5		0.45	1450	2.00	77K, 1atm	18	63
Zn ₂ (bdc) ₂ (dabco)	7.8 / 9.5	0.75	0.62	1450	2.00	77K, 1atm	17	64
Zn ₂ (bdc) ₂ (tmbdc)(dabco)	/ 6	0.59	0.45	1100	2.10	77K, 1atm	19	64
Zn ₂ (tmbdc) ₂ (dabco)	/ 8	0.50	0.55	920	1.80	77K, 1atm	18	64
Zn ₂ (ndc) ₂ (dabco)	/	0.52		1000	1.70	77K, 1atm	16	64
Zn ₂ (tfbdc) ₂ (dabco)	7.5 / 11	0.57	0.55	1070	1.80	77K, 1atm	19	64
Zn ₂ (tmbdc) ₂ (bpy)	8.0 / 10	0.62	0.48	1120	1.70	77K, 1atm	12	64
Ni ₂ (bpy) ₃ (NO ₃) ₄ (M)	2.4 / 4.0	0.18	0.05		0.80	77K, 1atm		65
Ni ₂ (bpy) ₃ (NO ₃) ₄ (E)	2.1 / 4.2	0.15	0.05		0.70	77K, 1atm		65
Ni ₃ (btc) ₂ (3-pic) ₆ (pd) ₃	8.5 / 10.7	0.63	0.30		2.10	77K, 14 bar		65
Zn ₄ O(L ¹) ₃	3.8 / 7.8	0.20	0.21	502	1.12	RT, 48 atm		40
Zn ₄ O(L ²) ₃	3.8 / 5.4	0.13	0.17	396	0.98	RT, 48 atm		40
Cu ₂ (pzdc) ₂ (pyz), CPL-1	3.4 / 5.0		0.04		0.20	89K, 1atm		66
Cu ₂ (bptc), MOF-505	6.7 / 10.1	0.63	0.37	1830	2.48	77K, 1atm		35
Co[Fe(CN) ₆]NO	/	0.37		523	2.60	77K, 1atm		67
Ni[Fe(CN) ₆]NO	/	0.32		634	2.66	77K, 1atm		67
Mn ₃ [(Co(CN) ₆) ₂]	/	1.19		870	1.60	77K, 1.2atm	19	68
Fe ₃ [(Co(CN) ₆) ₂]	/	1.21		770	1.40	77K, 1.2atm	17	68
Co ₃ [(Co(CN) ₆) ₂]	/	1.27		800	1.50	77K, 1.2atm	19	68
Ni ₃ [(Co(CN) ₆) ₂]	/	1.29		560	1.40	77K, 1.2atm	18	68
Cu ₃ [(Co(CN) ₆) ₂]	/	1.39		730	1.80	77K, 1.2atm	25	68
Zn ₃ [(Co(CN) ₆) ₂]	/	1.29		720	1.40	77K, 1.2atm	18	68
Zn ₄ O(bdc) ₃ , MOF5	/	1.19		3400	1.50	77K, 1.2atm	9	68
[Zn ₃ (bpdca) ₃ bpy]-4DMF-H ₂ O	/ 11	0.33	0.41	774	1.50	77K, 1atm	15	25, 62
[Co ₃ (bpdca) ₃ bpy]-4DMF-H ₂ O	/ 11	0.38	0.41	917	1.98	77K, 1atm	18	25, 69
[Co ₃ (bpdca) ₃ bpy]-4DMF-H ₂ O	/ 11	0.38	0.41	917	3.00	RT, 13 atm	35	25, 69
Cu ₃ (BTC) ₂ (H ₂ O) ₃	/ 9	0.40	0.59	629	1.44	77K, 1atm	13	62
Zn(tbip)	/ 6.0	0.14	0.21	242	0.75	77K, 1atm	11	70
Zn(tbip)	/ 6.0	0.14			1.61	RT, 48 atm	24	70
Zn ₄ O(NTB) ₂ 3DEF-EtOH	/	0.42	0.40	1121	1.90	77K, 1atm		69
Mg ₃ (NDC) ₃	6.3 / 7.1			190	0.46	77K, 1.2atm		71

[1] Calculated by Cerius² software, [2] Calculated from N₂ adsorption data collected at 77K using the DA(Dubinin-Radushkevich) method, [3] Calculated by Cerius² software and using a probe radius of 1.45Å, which corresponds to the kinetic diameter of H₂, [4] Calculated from N₂ adsorption data collected at 77K using the Langmuir model, [5] calculated from (gravimetric uptakes X density after removal of guest molecules)

bdc=benzene-1,4-dicarboxylate, R6-bdc=1,2-dihydrocyclobutylbenzene-3,6-dicarboxylate, ndc=naphthalene-2,6-dicarboxylate, hpdc=4,5,9,10-tetrahydropyrene-2,7-dicarboxylate, tmbdc=2,3,5,6-tetramethylbenzene-1,4-dicarboxylate, btb=benzene-1,3,5-tribenzoate, hfipbb= 4,4'-(hexafluoroisopropylidene)bisbenzoate, cyclam =1,4,8,11-tetraazacyclotetradecane, bpydc=2,2'-bipyridyl-5,5'-dicarboxylate, dabco =1,4-diazabicyclo[2.2.2]octane, bpy =4,4'-bipyridine, btc =benzene-1,3,5-tricarboxylate, 3-pic=3-picoline, pd =1,2-propanediol, L1=6,6'-dichloro-2,2'-diethoxy-1,1'-binaphthyl-4,4'-dibenzoate, L2=6,6'-dichloro-2,2'-dibenzoyloxy-1,1'-binaphthyl-4,4'-dibenzoate, bptc=biphenyl-3,3',5,5'-tetracarboxylate, tbip=5-tert-butyl isophthalic acid, ntib=4,4',4''-nitrotrisbenzoic acid, def=N,N'-diethylformamide, tfbdc=tetrafluoroterephthalate, tatb=4,4',4''-s-triazine-2,4,6-triyl-tribenzoate.

1.6.2 H₂ Volumetric Uptake vs. Pore Volume and Accessible Volume Fraction

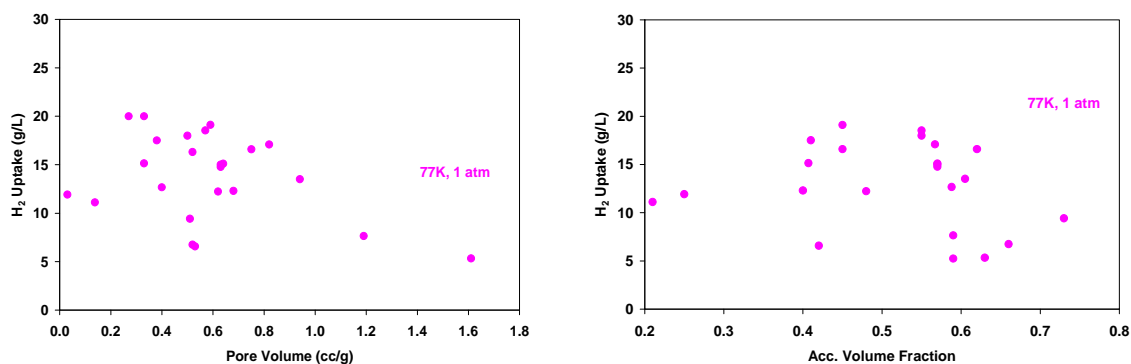


Figure 1.7 The volumetric H₂ uptake properties as a function of pore volume (left) and accessible volume fraction (right)

No clear correlations between hydrogen volumetric uptake and pore volume (or Acce. Volume) are found, as shown in Fig. 1.7. In both plots, most values obtained at 1 atm condition are in the region under 20 g/L or 0.02g/cc which is much lower than density of liquid hydrogen, 0.03~0.08 g/cc or 30~80g/L.

1.6.3 H₂ Uptake vs. Solvent Accessible Volume Fraction

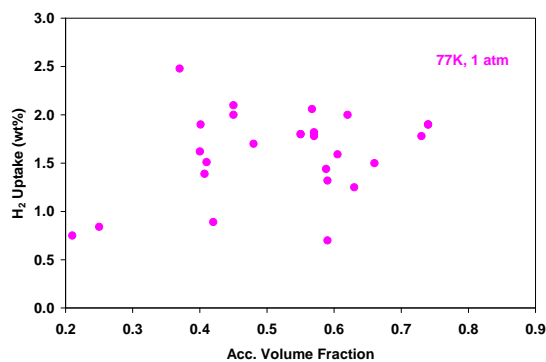


Figure 1.8 The gravimetric H₂ uptake properties as a function of accessible volume fraction.

The plot of hydrogen uptake vs. accessible volume fraction is made based on the Table 1.2. No strong correlation is found between hydrogen uptakes and solvent accessible volume at 1 atmospheric pressure and 77 K, although it seems the relatively high hydrogen uptake is achieved above ~35 % of free volume based on the existing data.

1.6.4 H₂ Uptakes vs. Surface Area

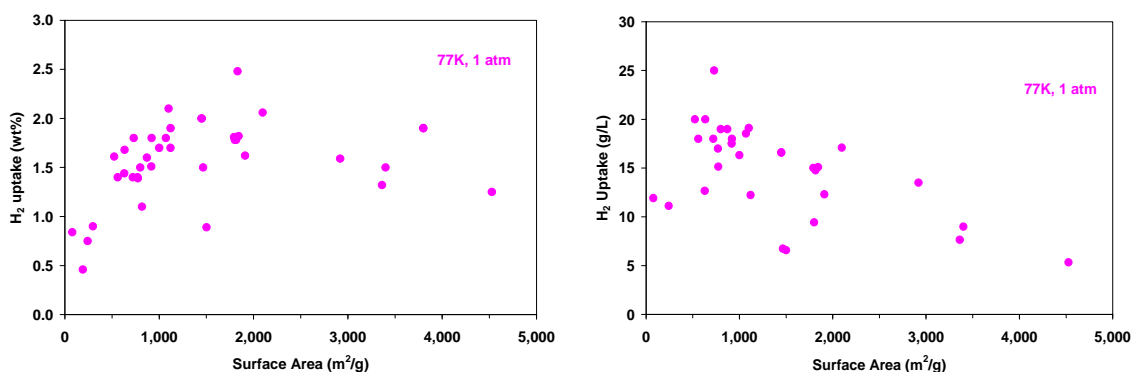


Figure 1.9 The H₂ uptake properties as a function of surface area in gravimetric scale (left) and in volumetric scale (right).

Although a weak correlation is observed between the H₂ uptakes and surface area below 1500 m²/g, other region of the plot at low pressure (1 atm) does not show a clear relation between hydrogen uptake and surface area. A comparison at high pressure is not attempted due to the lack of data.

Based on the literature review on hydrogen adsorption, the starting line of this dissertation study was built. The MOF materials for hydrogen storage should have at least 6 Å size pores and 30 % or more free volume fraction as well as higher surface area.

1.7 Literature Reviews on Methane Sorption Study of MOFs

Metal-Organic Frameworks (MOFs) have also been studied as methane storage media due to their permanent porosity and tunable pore properties.^{19, 59, 72-74} The boiling point of methane is -162°C at 1 atmosphere and it is a main component of natural gas. It is also one of the promising candidates of alternative fuels for replacing gasoline and diesel for automobile. Natural gas is currently stored as compressed natural gas (CNG) at 207 bar in the pressure containers requiring an expensive compression procedure.

The U.S. Department of Energy (DOE) defined the methane storage target as 150 v/v (STP; 298 K and 1 atm) at 35 bar per volume of the storage vessel in 1993.⁷³ The porous absorbent materials have been studied for methane storage⁷³ and 200 (v/v) volumetric (defined as volume of the gas divided by volume of the tank) and 20% gravimetric (defined as the weight of the adsorbed gas divided by the weight of the adsorbant) storage capability have been reported at pressure between 500 and 700 psig on activated carbon.⁷³

In 2002, Eddaoudi et al. showed that IRMOF-6 took 240 cc (STP)/g high capacity of methane at 36 atm and two years later Dören et al. simulated even higher storage capacity (271 cc/g, STP at 35 bar) on IRMOF-14. Earlier theoretical studies have shown that around 8 Å of pore diameter is optimal pore diameter for methane storage^{72, 75} therefore two adsorbed layers of methane could be accommodated in the pore.

1.8 Gas Adsorption Studies and Pore Properties of MOFs

The IUPAC⁷⁶ proposed that pores are divided into three classes by their pore width. The pore width can be defined as the distance between opposite walls in case of a slit shape of the pore and as the diameter in the case of a cylindrical shape of the pore. Thus, *Micropore* is a pore of internal width less than 2 nm; *Mesopore* is a pore of internal width between 2 and 50 nm; and *Macropore*, a pore of internal width greater than 50 nm. In the micropore range, it is further divided into two subclasses; *Ultramicropore*: pore width smaller than 0.7 nm and *Supermicropore*: pore width in the range from 0.7 nm to 2 nm. Most of the pores in MOFs fall in the range of micropores.

An understanding of the pore properties and surface area of porous materials can be achieved by gas adsorption studies. The term “adsorption” can be described as the enrichment of certain gases such as nitrogen (N₂), argon (Ar) and hydrogen (H₂), on the interfacial layer.⁷⁶ In the gas sorption we can consider the gas/solid interface. The solid or porous material is called the adsorbent and the gas, which is capable of being adsorbed, is called the adsorbate.⁷⁶ The amount of adsorbate gases on the solid surface can be measured over a wide range of relative pressure P/P° , or the ratio of measuring pressure (P) and saturated pressure (P°) of the adsorbate gas at analysis temperature, at constant temperature and the amount adsorbed as a function of relative pressure is called the adsorption isotherm. Similarly, desorption isotherms can be collected by measuring the quantities of gas removed from the solid surface as the relative pressure is lowered. In the case of the volumetric method, the adsorption isotherm is obtained point by point by measuring the equilibrium pressure of the adsorbent at the given volume. All isotherms can be classified into one of the five types shown in Figure 1.10.

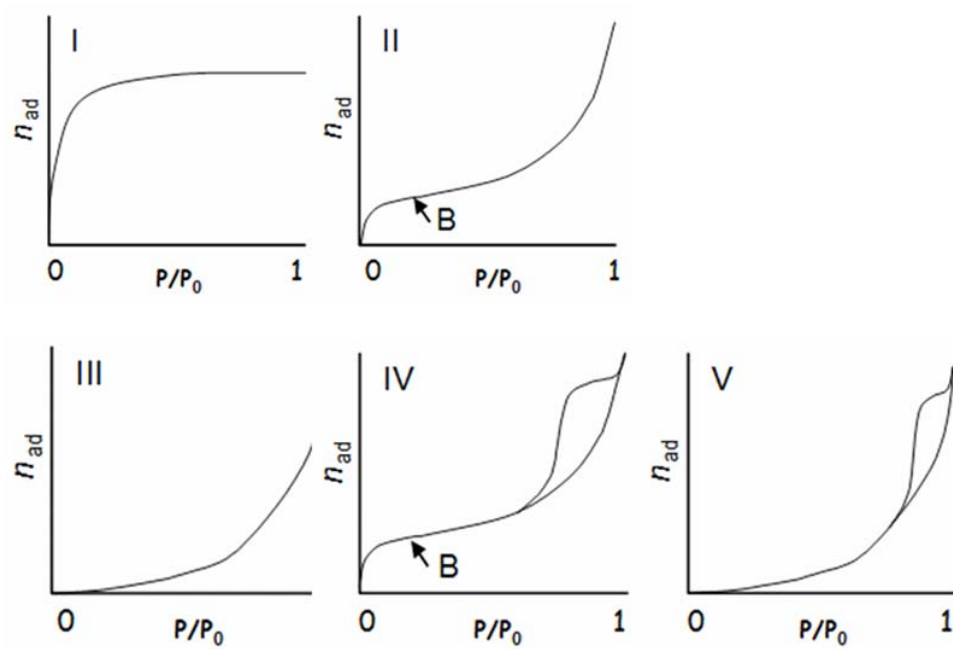


Figure 1.10 IUPAC classification of sorption isotherm types.⁷⁶

Type I or Langmuir isotherms are reversible and concave to the P/P° axis and the quantity of the adsorbed adsorbate approaches a limiting value as $P/P^\circ = 1$. The plateau region is observed when the adsorption is limited to only a few molecular layers. Because of the narrow pore width in microporous materials, micropore filling and high uptakes are observed at relatively low pressure. This often results in type I isotherm.

Type II isotherms are observed in case of mesoporous or macroporous adsorbent. These isotherms often have an inflection point (point B), which indicates the stage where the monolayer coverage is complete and multilayer adsorption begins to occur.

Type III isotherms are convex to the P/P° axis over its entire range and no inflection point is observed. This indicates that the adsorbate/adsorbent interactions are relatively weak and the interaction of adsorbate/adsorbate is more important. But this type of isotherm is not common.

Type IV isotherms are typical in mesoporous materials. The characteristic feature of this type of isotherm is the hysteresis loop, which is associated with capillary condensation in mesopores and which is indicated by the steep slope at higher relative pressure. The plateau region right after the steep slope indicates complete pore filling. The initial part of the type IV isotherm follows the same path as in case of the type II isotherm.

Type V isotherms are not common. This type shows pore condensation and hysteresis at relatively high pressure, however the path at low relative pressure follows the same path as the type III.

Type I, II and III isotherms are generally reversible, however microporous materials having type I isotherms can exhibit hysteresis. Type IV and V usually exhibit a hysteresis

loop between adsorption and desorption isotherms at relatively high pressure. In some cases, porous materials show low-pressure hysteresis, which may be observable at very low relative pressure. This low-pressure hysteresis may be associated with the change in volume of the adsorbent. If swelling occurs in the adsorbent at low relative pressure, the adsorbent can hold more adsorbates in its pores. Low-pressure hysteresis can be observed in the irreversible uptake of adsorbate molecules in pores if the pore width of the adsorbent has a similar size as that of the adsorptive molecules.

1.8.1 Micropore Volume Calculation from Nitrogen and Argon Isotherms

In order to interpret isotherms collected on the microporous materials at cryogenic temperature, a thermodynamic assumption has been developed. As the adsorbed nitrogen at liquid nitrogen temperature (77 K) and the adsorbed argon at liquid argon temperature (87 K) on microporous materials are liquid-like fluids, it is assumed that adsorbed adsorbates essentially have the same properties as a bulk liquid at those cryogenic temperatures. Based on this assumption and the ideal gas state equation, the density of each adsorbate can be calculated as shown below.

If the liquid phase is set to state 1 and the gas phase to state 2, the mole number of each phase, n_1 and n_2 , can be expressed by equation (1) and (2)

$$n_1 = \frac{W_1}{M_w} = \frac{(V_1 \times d_1)}{M_w} \quad (1)$$

$$n_2 = \frac{W_2}{M_w} = \frac{(V_2 \times d_2)}{M_w} \quad (2)$$

(where W = weight, M_w = Molecular weight, V = Volume and d = density)

Since $n_1 = n_2$, equation (3) can be obtained.

$$(V_1 \times d_1) = (V_2 \times d_2) \text{ or } \frac{V_1}{V_2} = \frac{d_2}{d_1} \text{ or } V_1 = \frac{d_2}{d_1} \times V_2 \quad (3)$$

Since the relative density of liquid nitrogen⁷⁷ is 0.81 g/mL against that of water, 1.0 g/mL, the volume of the liquid-like fluid on the surface of microporous materials can be calculated from its adsorbed volume of nitrogen, which is collected at liquid nitrogen temperature.

$$\frac{V_1}{V_2} = \frac{d_2}{d_1} = \frac{28.01 \text{ g} / 22,400 \text{ mL}}{0.81 \text{ g} / \text{mL}} = 0.001544 \quad (4)$$

or

$$V_1 = 0.001544 \times V_2 \quad (5)$$

or

$$V_{Liq} (\text{cc} / \text{g}) = 0.001544 \times V_{STP} (\text{cc} / \text{g}) \quad (5')$$

By multiplying the conversion factor to adsorbed volume, V_{ads} (STP, cc/g), the adsorbed liquid volume, V_{ads} (Liq, cc/g), can be calculated. The conversion factors for other gases were calculated in the same way and are listed in Table 1.3.

Table 1.3 The conversion factor between Liquid and Gas⁷⁸

Metric Units			Boiling Point		Gas Phase Properties			Liquid Phase Properties	
			@ 101.325 kPa		@ 0° C & @ 101.325 kPa			@ B.P., & @ 101.325 kPa	
			Temp.	Latent Heat of Vaporization	Specific Gravity	Specific Heat (Cp)	Density	Specific Gravity	Specific Heat (Cp)
Gas	M.W.	Conversion factor	°C	kJ/kg	Air = 1	kJ/kg ° C	kg/m ³	Water = 1	kJ/kg ° C
H ₂	2.02	0.001288	-252.8	446	0.07	14.34	0.08988	0.071	9.668
N ₂	28.01	0.001544	-195.8	199.1	0.97	1.04	1.2506	0.81	2.042
Ar	39.95	0.001274	-185.9	162.3	1.39	0.523	1.7837	1.4	1.078
CH ₄	16.04	0.001279	-161.5	509.91	0.56	2.207	0.717	0.425	3.481
CO ₂	44.01	0.001276	-78.5	571.3	1.539	0.85	1.9769	1.18 [#]	--
O ₂	32.00	0.001284	-183	213	1.113	0.9191	1.429	1.14	1.669
CO	28.01	0.001284	-191.5	215.8	0.9736	1.037	1.2504	0.79	--

[#] Triple point

Based on the liquid volume in the converted isotherms, the pore volume of microporous materials can be estimated under the assumption that the bulk properties of liquid-like fluid are the same as those of its liquid. In practice, the micropore volume can be read from the isotherm plot of V_{liq} (cc/g) versus relative pressure (P/P°). The obtained micropore volume from the plot was confirmed with the results of volume calculation using the commercially available software containing various developed calculation models such as Dubinin-Radushkevich (DR)⁷⁹, Dubinin-Astakhov (DA)⁸⁰ and Horvath-Kawazoe (HK) method.⁸¹

1.8.2 Hydrogen Adsorption and Isostatic Heat of Adsorption, Q_{st}

To evaluate the capability of hydrogen storage in microporous materials, hydrogen sorption isotherms can be measured at cryogenic temperatures using liquid nitrogen or liquid argon as coolant. In the hydrogen sorption, the quantity of adsorbed hydrogen by

the microporous materials can be used to calculate the gravimetric density of hydrogen directly. The strength of sorbent-sorbate interactions can be estimated by the isosteric heat of adsorption (Q_{st}).

The isosteric heat of adsorption (Q_{st}) is a differential quantity based on the Clausius-Clapeyron equation (6).⁸² It is related to the energy of H₂ adsorption and can be considered a measure of the extent of adsorbent-adsorbate interactions in a porous material.

$$\ln p = -\frac{Q_{st}}{R} \cdot \frac{1}{T} + C \quad (6)$$

The Q_{st} values can be calculated using hydrogen adsorption isotherms measured at different temperatures. The meaning of the term “*isosteric*” is equal surface coverage at different temperatures. Therefore, at least two isotherms, obtained at different temperatures, are needed to calculate the Q_{st} . If more than three set of isotherms are available, Q_{st} can be calculated from the slope of the plot of $\ln p$ vs. $1/T$. So far, isotherms taken at two temperatures (77 K and 87 K) were used for Q_{st} calculations at cryogenic temperatures.

By introducing of two different temperatures (T_1 , T_2) and pressures (p_1 , p_2) into equation (6) and rearranging, equation (7) or (8) can be obtained.

$$\ln p_1 - \ln p_2 = -\frac{Q_{st}}{R} \left[\frac{1}{T_1} - \frac{1}{T_2} \right] \quad (7)$$

or

$$Q_{st} = -R \times \frac{\ln(P_1/P_2)}{\left[\frac{1}{T_1} - \frac{1}{T_2} \right]} \quad (8)$$

One set of isotherms for $[\text{Zn}_3(\text{bpdc})_3(\text{bpy})]$ was collected at two cryogenic temperatures. The results are shown in Figure 1.11. From the selected point of coverage on both isotherms in Figure 1.11a, values of pressure can be obtained from the abscissa. By plugging the temperature and pressure values (P_1 and P_2) into equation (8), one obtains a point of isosteric heat of adsorption. A set of Q_{st} calculated in this manner is plotted in Figure 1.11b. These plots are also useful in estimating the extent of interactions between adsorbate and adsorbent or between adsorbates themselves. Since the strength of solid/gas interaction in the first layer is always stronger than gas/gas interaction in the second layer (if any), the Q_{st} values are expected to decrease monotonically as a function of H_2 loading.

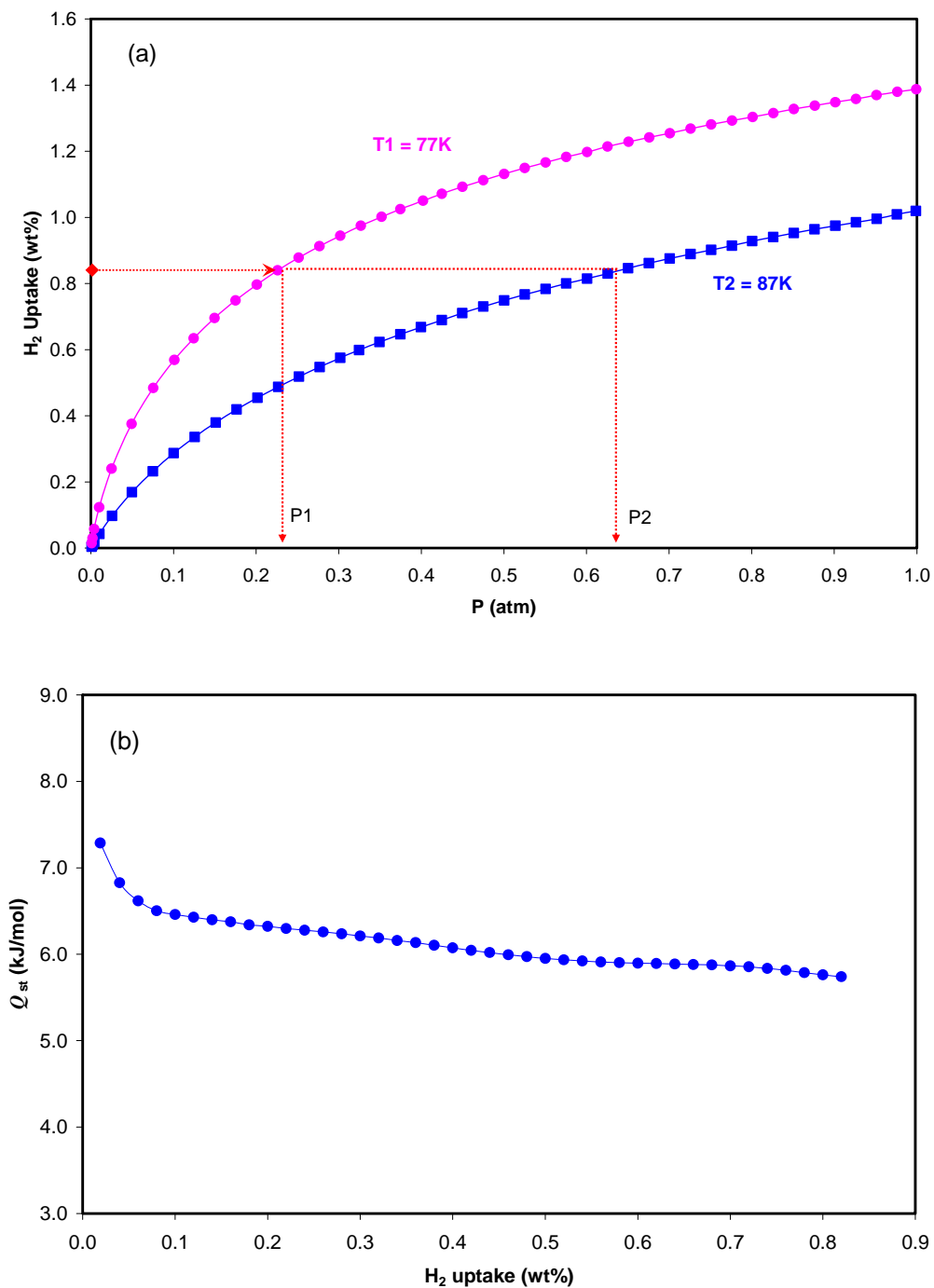


Figure 1.11 (a) A set of H_2 isotherms obtained at 77K and 87K for $[Zn_3(bpd c)_3(bpy)]$ are used to find pressures p_1 and p_2 , (b) A plot of isosteric heat of adsorption, Q_{st} as a function of the H_2 uptake.

1.9 Research Objective

The goal of my research project is to design and synthesize novel microporous MOFs with different pore size as storage media for hydrogen and methane.

To achieve this goal, three different approaches have been implemented. Firstly, new porous MOF materials have been developed by introducing new organic linkers and pillars that modify pore structures of known structure types leading to enhance hydrogen uptake. Secondly, pore properties such as pore diameter, micropore volume, surface area and pore size distribution have been characterized. Lastly, the interaction between hydrogen and MOFs has been interpreted based on isosteric heats of hydrogen adsorption from both low and high pressure gas sorption studies.

1.10 References

1. Cho, S.-H.; Ma, B.; Nguyen, S. T.; Hupp, J. T.; Albrecht-Schmitt, T. E., A metal-organic framework material that functions as an enantioselective catalyst for olefin epoxidation. *Chem. Comm.* **2006**, (24), 2563-2565.
2. Sawaki, T.; Aoyama, Y., Immobilization of a Soluble Metal Complex in an Organic Network. Remarkable Catalytic Performance of a Porous Dialkoxyzirconium Polyphenoxide as a Functional Organic Zeolite Analogue *Journal of the American Chemical Society* **1999**, 121, 4793-4798.
3. Seo, J. S.; Whang, D.; Lee, H.; Jun, S. I.; Oh, J.; Jeon, Y. J.; Kim, K., A homochiral metal-organic porous material for enantioselective separation and catalysis. *Nature* **2000**, 404, (6781), 982-986.
4. Wang, Q. M.; Shen, D.; Bülow, M.; Lau, M. L.; Deng, S.; Fitch, F. R.; Lemcoff, N. O.; Semanscin, J., Metallo-organic molecular sieve for gas separation and purification *Microporous and Mesoporous Materials* **2002**, 55, (2), 217-230.
5. Albrecht, M.; Lutz, M.; Spek, A. L.; van Koten, G., Organoplatinum crystals for gas-triggered switches. *Nature* **2000**, 406, (6799), 970-974.
6. Beauvais, L. G.; Shores, M. P.; Long, J. R., Cyano-Bridged Re_6Q_8 (Q = S, Se) Cluster-Cobalt(II) Framework Materials: Versatile Solid Chemical Sensors. *J. Am. Chem. Soc.* **2000**, 122, (12), 2763-2772.
7. Min, K. S.; Suh, M. P., Silver(I)-Polynitrile Network Solids for Anion Exchange: Anion-Induced Transformation of Supramolecular Structure in the Crystalline State. *J. Am. Chem. Soc.* **2000**, 122, (29), 6834-6840.
8. Yaghi, O. M.; Li, H., T-Shaped Molecular Building Units in the Porous Structure of $\text{Ag}(4,4'\text{-bpy})\cdot\text{NO}_3$. *J. Am. Chem. Soc.* **1996**, 118, (1), 295-296.
9. Dong, Y. B.; Jin, G. X.; Smith, M. D.; Huang, R. Q.; Tang, B.; zur Loye, H. C., $[\text{Ag}_2(\text{C}_{33}\text{H}_{26}\text{N}_2\text{O}_2)(\text{H}_2\text{O})_2(\text{SO}_3\text{CF}_3)_2]\cdot 0.5\text{C}_6\text{H}_6$: A Luminescent Supramolecular Silver(I) Complex Based on Metal-Carbon and Metal-Heteroatom Interactions. *Inorg. Chem.* **2002**, 41, (19), 4909-4914.
10. Evans, O. R.; Lin, W., Crystal Engineering of Nonlinear Optical Materials Based on Interpenetrated Diamondoid Coordination Networks. *Chem. Mater.* **2001**, 13, (8), 2705-2712.
11. Dubbeldam, D.; Walton, Krista S.; Ellis, Donald E.; Snurr, Randall Q., Exceptional Negative Thermal Expansion in Isoreticular Metal-Organic Frameworks. *Angew. Chem.* **2007**, 119, (24), 4580-4583.

12. Dybtsev, D. N.; Chun, H.; Yoon, S. H.; Kim, D.; Kim, K., Microporous manganese formate: a simple metal-organic porous material with high framework stability and highly selective gas sorption properties. *J. Am. Chem. Soc.* **2004**, 126, (1), 32-33.
13. Pan, L.; Sander, M. B.; Huang, X.; Li, J.; Smith, M.; Bittner, E.; Bockrath, B.; Johnson, J. K., Microporous metal organic materials: promising candidates as sorbents for hydrogen storage. *J. Am. Chem. Soc.* **2004**, 126, (5), 1308-1309.
14. Uemura, K.; Matsuda, R.; Kitagawa, S., Flexible microporous coordination polymers. *Journal of Solid State Chemistry* **2005**, 178, (8), 2420-2429.
15. Lee, E. Y.; Suh, M. P., A robust porous material constructed of linear coordination polymer chains: reversible single-crystal to single-crystal transformations upon dehydration and rehydration. *Angew. Chem. Int. Ed.* **2004**, 43, (21), 2798-2801.
16. Kitagawa, S.; Kitaura, R.; Noro, S.-i., Functional Porous Coordination Polymers. *Angew. Chem. Int. Ed.* **2004**, 43, (18), 2334-2375.
17. Forster, P. M.; Thomas, P. M.; Cheetham, A. K., Biphasic Solvothermal Synthesis: A New Approach for Hybrid Inorganic-Organic Materials. *Chem. Mater.* **2002**, 14, (1), 17-20.
18. Yaghi, O. M.; O'Keeffe, M.; Ockwig, N. W.; Chae, H. K.; Eddaoudi, M.; Kim, J., Reticular synthesis and the design of new materials. *Nature* **2003**, 423, (6941), 705-714.
19. Eddaoudi, M.; Kim, J.; Rosi, N.; Vodak, D.; Wachter, J.; O'Keeffe, M.; Yaghi, O. M., Systematic design of pore size and functionality in isorecticular MOFs and their application in methane storage. *Science* **2002**, 295, (5554), 469-72.
20. Lee, E.; Kim, J.; Heo, J.; Whang, D.; Kim, K., A Two-Dimensional Polyrotaxane with Large Cavities and Channels: A Novel Approach to Metal-Organic Open-Frameworks by Using Supramolecular Building Blocks. *Angew. Chem. Int. Ed.* **2001**, 40, (2), 399-402.
21. Pan, L.; Kelly, S.; Huang, X.; Li, J., Unique 2D metalloporphyrin networks constructed from iron(II) and meso-tetra(4-pyridyl)porphyrin. *Chem Commun (Camb)* **2002**, (20), 2334-2335.
22. Ciurtin, D. M.; Smith, M. D.; Loye, H.-C. z., [Cu(pyrazine-2-carboxylate)₂]₂Cd₄I₈: unprecedented 1-D serpentine inorganic chains and regular 2-D metal-organic square grids in a 3-D framework. *Chem. Comm.* **2002**, (1), 74-75.
23. Liu, Y. H.; Lu, Y. L.; Wu, H. C.; Wang, J. C.; Lu, K. L., [Cd^{II}(bpdc)·H₂O]_n: A Robust, Thermally Stable Porous Framework through a Combination of a 2-D Grid and a

Cadmium Dicarboxylate Cluster Chain ($H_2bpdca = 2,2'$ -Bipyridyl-4,4'-dicarboxylic Acid). *Inorg. Chem.* **2002**, 41, (9), 2592-2597.

24. Yi, L.; Ding, B.; Zhao, B.; Cheng, P.; Liao, D. Z.; Yan, S. P.; Jiang, Z. H., Novel Triazole-Bridged Cadmium Coordination Polymers Varying from Zero- to Three-Dimensionality. *Inorg. Chem.* **2004**, 43, (1), 33-43.

25. Lee, J. Y.; Pan, L.; Kelly, S. P.; Jagiello, J.; Emge, T. J.; Li, J., Achieving High Density of Adsorbed Hydrogen in Microporous Metal Organic Frameworks. *Advanced Materials* **2005**, 17, (22), 2703-2706.

26. Ogden, J. M., Prospects for building a hydrogen energy infrastructure. *Annual Review of Energy and the Environment* **1999**, 24, (1), 227-279.

27. Ritter, J. A.; Ebner, A. D.; Wang, J.; Zidan, R., Implementing a hydrogen economy. *Materials Today* **2003**, 6, (9), 18-23.

28. Züttel, A., Materials for hydrogen storage. *Materials Today* **2003**, 6, (9), 24-33.

29. DOE, (a) Hydrogen, Fuel Cells, & Infrastructure Technologies Program: Multi-year Research, Development, and Demonstration Plan; U.S. Department of Energy, February 2005, Chapter 3, <http://www.eere.energy.gov/hydrogenandfuelcells/mypp/>. (b) Basic Research Needs for the Hydrogen Economy, report of the Basic Energy Sciences Workshop on Hydrogen Production, Storage, and Use, U.S. Department of Energy, May 13-15, 2005, <http://www.sc.doe.gov/bes/>.

30. Bowman Jr, R. C.; Fultz, B., Theme Article - Metallic Hydrides I: Hydrogen Storage and Other Gas-Phase Applications. *MRS. Bull* **2002**, 27, 688.

31. Sandrock, G., A panoramic overview of hydrogen storage alloys from a gas reaction point of view. *Journal of Alloys and Compounds* **1999**, 293-295, 877-888.

32. Rosi, N. L.; Eckert, J.; Eddaoudi, M.; Vodak, D. T.; Kim, J.; O'Keeffe, M.; Yaghi, O. M., Hydrogen storage in microporous metal-organic frameworks. *Science* **2003**, 300, (5622), 1127-1129.

33. Sagara, T.; Ortony, J.; Ganz, E., New isoreticular metal-organic framework materials for high hydrogen storage capacity. *The Journal of Chemical Physics* **2005**, 123, (21), 214707.

34. Rowsell, J. L.; Spencer, E. C.; Eckert, J.; Howard, J. A.; Yaghi, O. M., Gas adsorption sites in a large-pore metal-organic framework. *Science* **2005**, 309, (5739), 1350-1354.

35. Chen, B.; Ockwig, N. W.; Millward, A. R.; Contreras, D. S.; Yaghi, O. M., High H₂ Adsorption in a Microporous Metal-Organic Framework with Open Metal Sites. *Angew. Chem. Int. Ed.* **2005**, 44, (30), 4745-4749.
36. Rowsell, J. L.; Eckert, J.; Yaghi, O. M., Characterization of H₂ binding sites in prototypical metal-organic frameworks by inelastic neutron scattering. *J. Am. Chem. Soc.* **2005**, 127, (42), 14904-14910.
37. Yildirim, T.; Hartman, M. R., Direct Observation of Hydrogen Adsorption Sites and Nanocage Formation in Metal-Organic Frameworks. *Physical Review Letters* **2005**, 95, (21), 215504-4.
38. Reineke, T. M.; Eddaoudi, M.; Fehr, M.; Kelley, D.; Yaghi, O. M., From Condensed Lanthanide Coordination Solids to Microporous Frameworks Having Accessible Metal Sites. *J. Am. Chem. Soc.* **1999**, 121, (8), 1651-1657.
39. Yang, Q.; Zhong, C., Molecular Simulation of Adsorption and Diffusion of Hydrogen in Metal-Organic Frameworks. *J. Phys. Chem. B* **2005**, 109, (24), 11862-11864.
40. Kesanli, B.; Cui, Y.; Smith, M. R.; Bittner, E. W.; Bockrath, B. C.; Lin, W., Highly Interpenetrated Metal-Organic Frameworks for Hydrogen Storage. *Angew. Chem. Int. Ed.* **2005**, 44, (1), 72-75.
41. Wong-Foy, A. G.; Matzger, A. J.; Yaghi, O. M., Exceptional H₂ Saturation Uptake in Microporous Metal-Organic Frameworks. *J. Am. Chem. Soc.* **2006**, 128, (11), 3494-3495.
42. Li, Y.; Yang, R. T., Significantly Enhanced Hydrogen Storage in Metal-Organic Frameworks via Spillover. *J. Am. Chem. Soc.* **2006**, 128, (3), 726-727.
43. Lachawiec, A. J.; Qi, G.; Yang, R. T., Hydrogen Storage in Nanostructured Carbons by Spillover: Bridge-Building Enhancement. *Langmuir* **2005**, 21, (24), 11418-11424.
44. Chui, S. S.; Lo, S. M.; Charmant, J. P.; Orpen, A. G.; Williams, I. D., A chemically functionalizable nanoporous material. *Science* **1999**, 283, (5405), 1148-1150.
45. Yang, S. Y.; Long, L. S.; Jiang, Y. B.; Huang, R. B.; Zheng, L. S., An Exceptionally Stable Metal-Organic Framework Constructed from the Zn₈(SiO₄) Core. *Chem. Mater.* **2002**, 14, (8), 3229-3231.
46. Chen, B.; Eddaoudi, M.; Hyde, S. T.; O'Keeffe, M.; Yaghi, O. M., Interwoven metal-organic framework on a periodic minimal surface with extra-large pores. *Science* **2001**, 291, (5506), 1021-1023.

47. Rowsell, J. L. C.; Yaghi, O. M., Metal-organic frameworks: a new class of porous materials. *Microporous and Mesoporous Materials* **2004**, 73, (1-2), 3-14.
48. Reineke, T. M.; Eddaoudi, M.; Moler, D.; O'Keeffe, M.; Yaghi, O. M., Large Free Volume in Maximally Interpenetrating Networks: The Role of Secondary Building Units Exemplified by $\text{Tb}_2(\text{ADB})_3[(\text{CH}_3)_2\text{SO}]_4 \cdot 16[(\text{CH}_3)_2\text{SO}]$. *J. Am. Chem. Soc.* **2000**, 122, (19), 4843-4844.
49. Eddaoudi, M.; Moler, D. B.; Li, H.; Chen, B.; Reineke, T. M.; O'Keeffe, M.; Yaghi, O. M., Modular chemistry: secondary building units as a basis for the design of highly porous and robust metal-organic carboxylate frameworks. *Acc Chem Res* **2001**, 34, (4), 319-330.
50. Sun, D.; Ma, S.; Ke, Y.; Collins, D. J.; Zhou, H. C., An Interweaving MOF with High Hydrogen Uptake. *J. Am. Chem. Soc.* **2006**, 128, (12), 3896-3897.
51. Rosi, N. L.; Eddaoudi, M.; Kim, J.; O'Keeffe, M.; Yaghi, O. M., Infinite secondary building units and forbidden catenation in metal-organic frameworks. *Angew. Chem. Int. Ed.* **2002**, 41, (2), 284-287.
52. Ma, S.; Sun, D.; Ambrogio, M.; Fillinger, J. A.; Parkin, S.; Zhou, H. C., Framework-Catenation Isomerism in Metal-Organic Frameworks and Its Impact on Hydrogen Uptake. *J. Am. Chem. Soc.* **2007**, 129, (7), 1858-1859.
53. Lee, J.; Huang, X.; Li, J., Infinite Zn-OH-(2Zn)-OH-Zn chain framework *Unpublished results in our group* **2005**.
54. Sheldrick, W. S.; Wachhold, M., Solventothermal Synthesis of Solid-State Chalcogenidometalates. *Angew. Chem. Int. Ed.* **1997**, 36, (3), 206-224.
55. Rabenau, A., The Role of Hydrothermal Synthesis in Preparative Chemistry. *Angew. Chem. Int. Ed.* **1985**, 24, (12), 1026-1040.
56. Laudise, R. A., Hydrothermal Synthesis of Crystals. *C&EN* **1987**, September 28, 30-43.
57. Laudise, R. A., *Progress in Inorganic Chemistry*. Interscience Publishers: New York, 1962; Vol. 3.
58. Rowsell, J. L. C.; Millward, A. R.; Park, K. S.; Yaghi, O. M., Hydrogen Sorption in Functionalized Metal-Organic Frameworks. *J. Am. Chem. Soc.* **2004**, 126, (18), 5666-5667.
59. Düren, T.; Snurr, R. Q., Assessment of Isorecticular Metal-Organic Frameworks for Adsorption Separations: A Molecular Simulation Study of Methane/*n*-Butane Mixtures. *J. Phys. Chem. B* **2004**, 108, (40), 15703-15708.

60. Férey, G.; Latroche, M.; Serre, C.; Millange, F.; Loiseau, T.; Percheron-Guégan, A., Hydrogen adsorption in the nanoporous metal-benzenedicarboxylate $M(OH)(O_2C-C_6H_4-CO_2)(M = Al^{3+}, Cr^{3+})$, MIL-53. *Chem. Comm.* **2003**, 24, 2976 - 2977.
61. Millange, F.; Serre, C.; Férey, G., Synthesis, structure determination and properties of MIL-53as and MIL-53ht: the first CrIII hybrid inorganic-organic microporous solids: $Cr^{III}(OH) \cdot \{O_2C-C_6H_4-CO_2\} \cdot \{HO_2C-C_6H_4-CO_2H\}_x$ *Chem Commun (Camb)* **2002**, (8), 822-823.
62. Lee, J.; Li, J.; Jagiello, J., Gas sorption properties of microporous metal organic frameworks. *Journal of Solid State Chemistry* **2005**, 178, (8), 2527-2532.
63. Dybtsev, D. N.; Chun, H.; Kim, K., Rigid and flexible: a highly porous metal-organic framework with unusual guest-dependent dynamic behavior. *Angew. Chem. Int. Ed.* **2004**, 43, (38), 5033-5036.
64. Chun, H.; Dybtsev, D. N.; Kim, H.; Kim, K., Synthesis, X-ray Crystal Structures, and Gas Sorption Properties of Pillared Square Grid Nets Based on Paddle-Wheel Motifs: Implications for Hydrogen Storage in Porous Materials. *Chemistry - A European Journal* **2005**, 11, (12), 3521-3529.
65. Zhao, X.; Xiao, B.; Fletcher, A. J.; Thomas, K. M.; Bradshaw, D.; Rosseinsky, M. J., Hysteretic Adsorption and Desorption of Hydrogen by Nanoporous Metal-Organic Frameworks. *Science* **2004**, 306, (5698), 1012-1015.
66. Kubota, Y.; Takata, M.; Matsuda, R.; Kitaura, R.; Kitagawa, S.; Kato, K.; Sakata, M.; Kobayashi, T. C., Direct Observation of Hydrogen Molecules Adsorbed onto a Microporous Coordination Polymer. *Angew. Chem. Int. Ed.* **2005**, 44, (6), 920-923.
67. Culp, J. T.; Matranga, C.; Smith, M.; Bittner, E. W.; Bockrath, B., Hydrogen Storage Properties of Metal Nitroprussides $M[Fe(CN)_5NO]$, ($M = Co, Ni$). *J. Phys. Chem. B* **2006**, 110, (16), 8325-8328.
68. Kaye, S. S.; Long, J. R., Hydrogen Storage in the Dehydrated Prussian Blue Analogues $M_3[Co(CN)_6]_2$ ($M = Mn, Fe, Co, Ni, Cu, Zn$). *J. Am. Chem. Soc.* **2005**, 127, (18), 6506-6507.
69. Lee, E. Y.; Jang, S. Y.; Suh, M. P., Multifunctionality and crystal dynamics of a highly stable, porous metal-organic framework $[Zn_4O(NTB)_2]$. *J. Am. Chem. Soc.* **2005**, 127, (17), 6374-6381.
70. Pan, L.; Parker, B.; Huang, X.; Olson, D. H.; Lee, J. Y.; Li, J., $Zn(tbip)$ ($H_2tbip = 5$ -tert-Butyl Isophthalic Acid): A Highly Stable Guest-Free Microporous Metal Organic Framework with Unique Gas Separation Capability. *J. Am. Chem. Soc.* **2006**, 128, (13), 4180-4181.

71. Dinca, M.; Long, J. R., Strong H₂ Binding and Selective Gas Adsorption within the Microporous Coordination Solid Mg₃(O₂C-C₁₀H₆-CO₂)₃. *J. Am. Chem. Soc.* **2005**, 127, (26), 9376-9377.
72. Cracknell, R. F.; Gordon, P.; Gubbins, K. E., Influence of pore geometry on the design of microporous materials for methane storage *J. Phys. Chem* **1993**, 97, (2), 494-499.
73. Wegrzyn, J.; Gurevich, M., Adsorbent storage of natural gas. *Applied Energy* **1996**, 55, (2), 71-83.
74. Düren, T.; Sarkisov, L.; Yaghi, O. M.; Snurr, R. Q., Design of New Materials for Methane Storage. *Langmuir* **2004**, 20, (7), 2683-2689.
75. Matranga, K. R.; Stella, A.; Myers, A. L.; Glandt, E. D., Molecular Simulation of Adsorbed Natural Gas. *Separation Science and Technology* **1992**, 27, (14), 1825 - 1836.
76. Sing, K. S. W.; Everett, D. H.; Haul, R. A. W.; Moscou, M.; Pierotti, R. A.; Rouquerol, J.; Siemieniewska, T., Reporting Physisorption Data for Gas/Solid Systems with special Reference to the Determination of Surface Area and Porosity. *Pure Appl. Chem* **1985**, 57, (4), 603-619.
77. NIST, <http://www.nist.gov/>.
78. UIGI, Physical Properties of Industrial Gases and Common Industrial Chemicals. http://www.uigi.com/physical_prop_m.html.
79. Dubinin, M. M.; Radushkevich, L. V., D-R method. *Dokl. Akad. Nauk. SSSR* **1947**, 55, 331.
80. Dubinin, M. M.; Astakhov, V. A., D-A method. *Adv.Chem.Series* **1970**, 102, 69.
81. Horvath, G.; Kawazoe, K., Method for Calculation of Effective Pore Size Distribution in Molecular Sieve Carbon. *J. Chem. Eng. Jpn.* **1983**, 16, (6), 470-475.
82. Clark, A., *Theory of Adsorption and Catalysis*. Academic Press: New York, 1970.

CHAPTER TWO

EFFECT OF PORE SIZE ON HYDROGEN SORPTION OF METAL- ORGANIC FRAMEWORKS AT LOW PRESSURE

2.1 Introduction

There has been an increasing interest in the exploitation of porous materials for possible applications in the area of on-board hydrogen storage. Research in this area is highly challenging due to the fact that hydrogen has a very low gravimetric and volumetric density. Thus, all existing hydrogen storage methods, including compressed gas, liquefaction, metal hydrides and porous carbon-based adsorbents, have various difficulties that must be overcome before large-scale commercialization can be considered.¹ The development of new storage materials that significantly increase hydrogen storage capability also becomes imperative.

Hydrogen is the most abundant element in the universe and has great potential to become one of the dominant energy carriers in the future.^{2, 3} Moreover, the sole byproduct of its reaction with oxygen to generate energy is water, an environmentally clean species. This is another significant advantage of hydrogen and it makes it superior to petroleum or other energy systems being used currently.⁴ However, due to its low volumetric energy density, adequate storage of hydrogen becomes a key issue that must

be addressed if the hydrogen economy is to be developed. The question is how to pack hydrogen into a space as small as possible without using excessively high pressure or very low temperatures. This need has led to an intense search for efficient storage materials. Unfortunately, none of the current developments is good enough for commercialization.¹

A sub-group of MOFs that contain pores with dimensions less than 2 nm (often in the range of several angstroms) is designated as microporous metal organic frameworks or MMOFs. They exhibit similar sorption properties to other porous materials characteristic of physisorption, including carbonaceous, silica and alumina. However, they also demonstrate some apparent advantageous features over these systems.⁵ For example, the MMOFs incorporate metals that are likely to interact with adsorbed hydrogen more strongly than other types of sorbents. They contain perfectly ordered channels that allow hydrogen to effectively access the interior space. The synthesis is simple, highly reproducible and cost-effective. Furthermore, the crystal structures and pore properties of MMOFs can be systematically modified to improve hydrogen uptake. A very recent simulation work has highlighted Li-doped metal-organic frameworks as promising candidates.⁶

The hydrogen adsorption in MOFs is achieved by associated adsorption, therefore the molecular identity of hydrogen is kept during the adsorption/desorption process. However not many studies have been conducted on the binding energy between hydrogen and MOF materials. In this chapter, ultra high resolution low pressure gas sorption properties of several MMOFs and their binding energy will be investigated in terms of

isosteric heats of adsorption based on isotherms obtained at two different cryogenic temperatures.

The materials presented in this chapter have three dimensional (3D) micro porous structures, such as $[\text{Zn}_3(\text{bpdc})_3\text{bpy}] \cdot 4\text{DMF} \cdot \text{H}_2\text{O}$ (**1**) (bpdc = biphenyldicarboxylate, bpy = 4,4'-bipyridine, DMF = N,N- dimethylformamide) and $[\text{Co}_3(\text{bpdc})_3\text{bpy}] \cdot 4\text{DMF} \cdot \text{H}_2\text{O}$ (**2**); 3D $[\text{Cu}(\text{hfipbb})(\text{H}_2\text{hfipbb})_{0.5}]$ (**3**) (H_2hfipbb = 4,4-(hexafluoroisopropylidene)-bis(benzoic acid); 3D $[\text{Zn}_2(\text{obba})_2(\text{bpy})] \cdot \text{DMF}$ (**4**) or $[\text{Zn}_2(\text{obba})_2(\text{bpy})] \cdot \text{DMA}$ (**4'**) (DMA= N,N- dimethylacetamide, obba = 4,4'-oxybisbenzoic acid); $[\text{Cu}_3(\text{BTC})_2(\text{H}_2\text{O})_3]$ (**5**) (BTC = benzene-1,3,5-tricarboxylate). All of these materials have one-dimensional open channels but different pore size. For comparison purposes, the sorption properties of the two non porous 2D layered structures of $\text{Co}(\text{ox})(\text{bpy})$ (**6**) ($\text{ox} = \text{C}_2\text{O}_4^{2-}$) and $\text{Ni}(\text{ox})(\text{bpy})$ (**7**) that do not contain open channels are also presented.

2.2 Experimental

Preparation of $[\text{Zn}_3(\text{bpdc})_3\text{bpy}]\cdot 4\text{DMF}\cdot \text{H}_2\text{O}$ (**1**) and $[\text{Co}_3(\text{bpdc})_3\text{bpy}]\cdot 4\text{DMF}\cdot \text{H}_2\text{O}$ (**2**).

Both **1** and **2** were prepared via solvothermal reactions described in our earlier work.^{7, 8} $\text{Zn}(\text{NO}_3)_2\cdot 6\text{H}_2\text{O}$ (98%, Acros), $\text{Co}(\text{NO}_3)_2\cdot 6\text{H}_2\text{O}$ (99%, Acros), bpdc (Aldrich, 99%+), bpy (Acros, 98%), and DMF (Fischer, 99%+ Reagent Grade) were used as received without further purification.

Column-like colorless crystals of **1** were obtained by reaction of $\text{Zn}(\text{NO}_3)_2\cdot 6\text{H}_2\text{O}$ (0.059 g) with bpdc (0.048 g) and bpy (0.031g) in 10 mL of DMF in the molar ratio of 1:1:1 at 150°C for 72 hours. Reactants were mixed in a Teflon-lined autoclave and heated in an oven at a constant temperature. After the reaction, the autoclave was cooled down naturally to room temperature. The solution was filtered and the product was washed three times with 10 mL of fresh DMF and the crystals were dried at 50°C for 5 minute under vacuum to remove surface solvent. Purple-colored column shaped crystals of **2** grew during the reaction of $\text{Co}(\text{NO}_3)_2\cdot 6\text{H}_2\text{O}$ (0.020g) with bpdc (0.025g) and bpy (0.016g) in DMF (5mL) at 150°C for 72 hours. The same filtering and drying conditions of **1** were applied to **2** for characterization and gas adsorption studies.

Single X-ray diffraction showed that the crystal structure of **1** is different but closely related to $[\text{Co}_3(\text{bpdc})_3\text{bpy}]\cdot 4\text{DMF}\cdot \text{H}_2\text{O}$ (**2**).⁷ The structure of **1** possesses two crystallographically independent zinc centers (Zn1 and Zn2).⁸ Two Zn1 and one Zn2 form a tri-nuclear metal cluster $[\text{Zn}_3(\text{bpdc})_6(\text{bpy})_2]$. As shown in Figure 2.1 (top), this building block is composed of one octahedral metal (Zn2) located at the center and two tetrahedral metals (Zn1) situated at two ends.

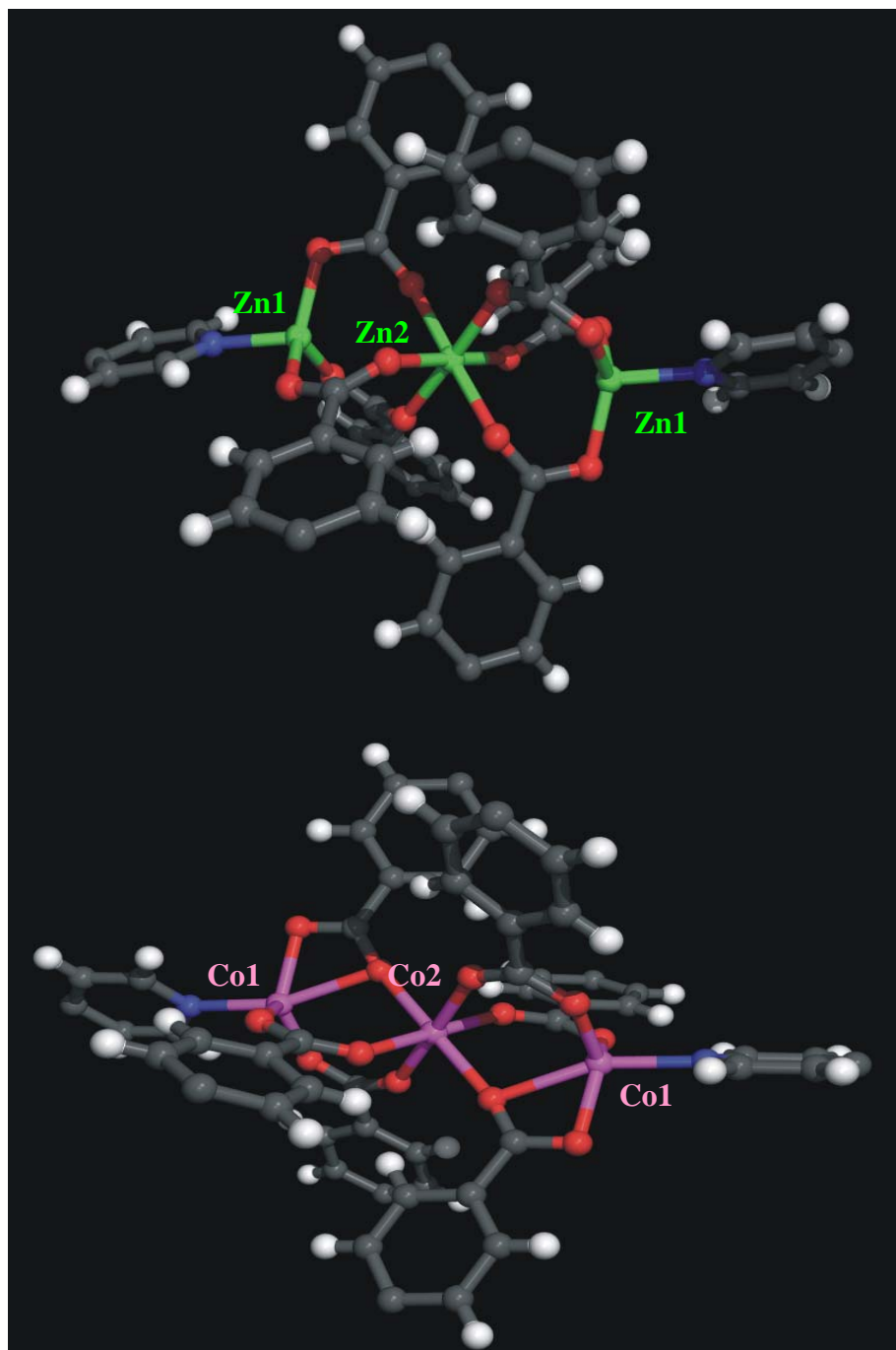


Figure 2.1 Top: The Zn₃ unit of **1**. The two terminal (outer) Zn have a tetrahedral coordination sphere (Zn1) and the center Zn (Zn2) has an octahedral coordination sphere. Bottom: The Co₃ unit of **2**. The two outer Co (Co1) have a trigonal bipyramidal coordination sphere, and the center Co (Co2) has an octahedral coordination sphere. Zn (green) and Co (pink), O (red), N (blue), C (gray), and H (white).

The metal nodes are connected to adjacent nodes by the carboxylate groups of the six bpdc ligands located in the equatorial plane to form two-dimensional (2D) double layers. The remaining two apical positions of the Zn1 are bound to nitrogen atoms of bpy to give rise to a three-dimensional (3D) pillared framework. Two such identical interpenetrating networks are interpenetrated to generate 1D channels as shown in Figure 2.2 (top). These 1D channels possess a unique internal surface structure, in that they are composed of alternating large diameter cages ($\sim 10.6 \times 10.6 \times 5$ Å, calculated based on van der Waals radius of carbon) and smaller windows (triangular in shape with an effective maximum dimension of ~ 8 Å). They are similar but not identical to those in **2**.⁷ The channels are filled with four DMF molecules and one water molecule as guests.

The most obvious difference in the structures of **1** and **2** is in the coordination number of the outer metals of the M3 unit, which is 4 for **1** and 5 for **2**, even though the 5th coordination of **2** has a Co-O bond length of 2.32 Å, which is rather long, the corresponding 5th Zn-O coordination distance is too long (2.8 Å) to be considered a bond. The other 3 metal-oxygen bonds of the outer metals are in the range of 1.94-1.95 Å for **1** and 1.94-2.01 Å for **2**, respectively. However, this difference in coordination number does not cause any striking difference in the overall motif and topology of the structure, because the same twists and rotations of the bpdc ligands in **1** are achieved in **2**, without a 5th Zn-O bond on each outer metal. Thus the crystal packing motif is nearly the same (i.e., nearly isomorphous) in **1** and **2**. On the other hand, based upon the unit cell packing diagram without solvent molecules (see Figure 2.2), **1** appears to have the 6-membered rings rotated somewhat more into the channel than **2** does. Thus the channels in **1** have more atoms “sticking into the voids”.

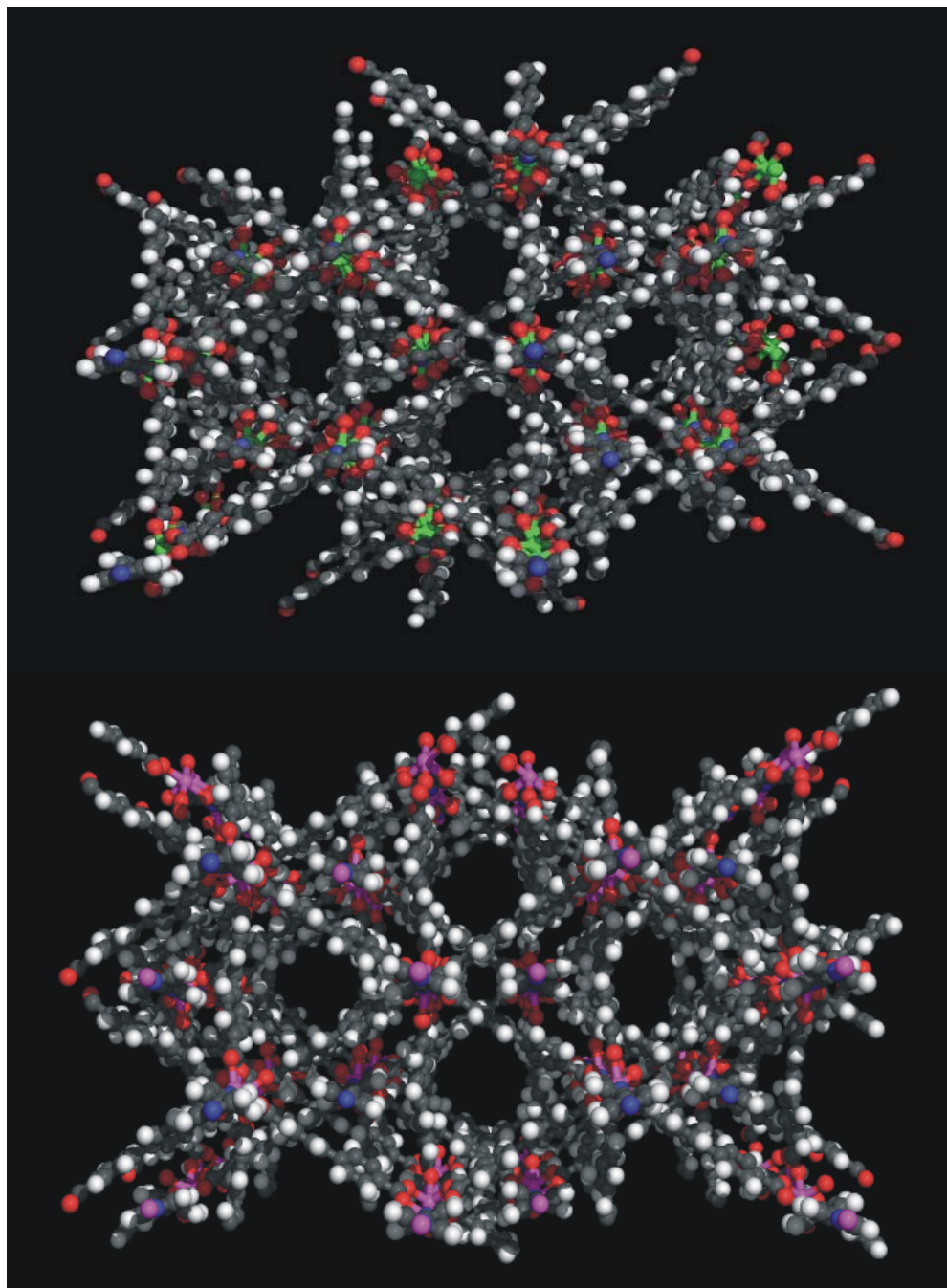


Figure. 2.2 Top: View of Structure **1** showing 1D channels. Bottom: View of Structure **2** showing the similar channels. The color codes are same as in Figure 2.1.

These rotational differences between the ligands of **1** and **2** are also evident in the side-by-side diagrams of the (closest ring) coordination spheres of **1** and **2** shown in Figure 2.1. Examination of key torsional angles for adjacent 6-membered rings and metal atoms quantifies these differences. Also indicative of conformational differences that lead to a different accessible volume in **1** and **2** are the dihedral angles between 6-membered rings whose centers-of-mass are inversion related (through the central metal atom) in the respective coordination spheres of **1** and **2**. This analysis was achieved using the SOLV routine in PLATON.^{9, 10} The volumes of potential solvent area (SA) were found to be 2658 Å³ (40.7 %) and 2812 Å³ (42.4 %) for **1** and **2**, respectively. SA is sometimes termed “accessible volume”.

Preparation of [Cu(hfipbb)(H₂hfipbb)_{0.5}] (3**).**

Cu(NO₃)₂·3H₂O (99%, Acros) and H₂hfipbb (Aldrich, 99%) were used as received without further purification. Column-shaped blue crystals of **3** were synthesized by the method described in an earlier paper of our group.⁵ Cu(NO₃)₂·3H₂O (0.024 g, 0.1 mmol) with excess H₂hfipbb (0.122 g, 0.31 mmol) in 5 mL of deionized water were mixed and placed in an oven at 160°C for 3 days. The molar ratio of the reaction components was 1:3.1. Excess H₂hfipbb was removed by repeatedly washing of the product with 10 mL of fresh DMF, followed by drying the product in an oven at 50°C under vacuum for five minute. As this compound has no guest molecule in the framework, it is designated as a guest-free metal-organic framework (GFMOF) and in general, thermally stable to ~400°C.¹¹ Compound **3** is thermally stable to 350°C confirmed by TG analysis.

Preparation of $[\text{Zn}_2(\text{obba})_2(\text{bpy})]\cdot\text{DMF}$ (**4**).

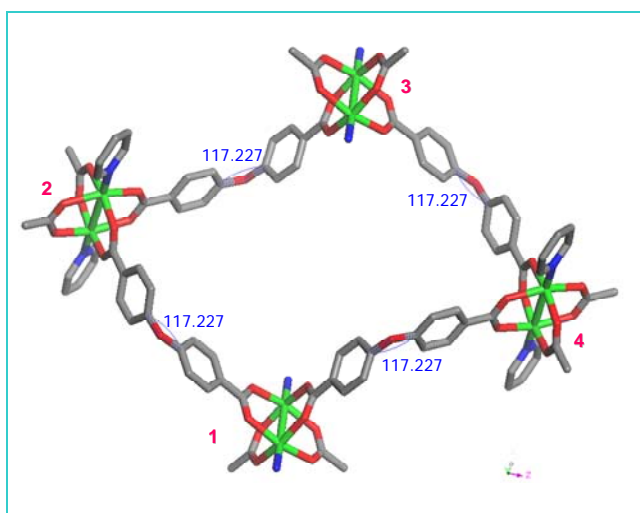
$\text{Zn}(\text{NO}_3)_2\cdot 6\text{H}_2\text{O}$ (98%, Acros) , H_2obba (Aldrich, 99%) and bpy (Acros, 98%) were used as received without any purification. Novel cube like transparent crystals of **4** were synthesized by solvothermal reaction. $\text{Zn}(\text{NO}_3)_2\cdot 6\text{H}_2\text{O}$ (0.116 g, 0.39 mmol), obba (0.104 g, 0.40mmol) and bpy (0.064 g, 0.41 mmol) were dissolved in 10 mL of DMF in a 20 mL vial. The solution in the vial was sonicated for 10 minute and the vial was placed in an oven at 100°C for 27 hours. Then, the product was filtered, washed with fresh DMF, followed by drying the product in an oven at 50°C under vacuum for five minute. A 0.102 g of single crystals was obtained, which corresponds to an approximately 30% yield. The same crystals could be obtained from a DMA solution having the same composition of reactants under the same reaction conditions.

Single crystal X-ray diffraction on the new crystals was performed on an automated Enraf-Nonius CAD4 diffractometer with graphite monochromated $\text{MoK}\alpha$ (or $\text{CuK}\alpha$) radiation. The structure analyses were carried out using SHELX97 or SHELXTL software packages. Powder X-ray diffraction (PXRD) of samples was performed on a Rigaku D/M-2200T automated diffraction system (Ultima+). The structure analyses were carried out using JADE (Version 3.0, 1996) software packages.

$[\text{Zn}_2(\text{obba})_2\text{h}(\text{bpy})]\cdot\text{DMF}$ (**4**) crystallizes in the orthorhombic crystal system with space group $Pcca$. The cell parameters are $a=16.749 \text{ \AA}$, $b=11.065 \text{ \AA}$, $c=22.419 \text{ \AA}$, $\alpha=90^\circ$, $\beta=90^\circ$, and $\gamma=90^\circ$, respectively. The unit cell volume and crystal density were calculated to be 4154.9 \AA^3 and 1.395 Mg/m^3 , respectively. The solvent accessible free volume after removal of guest molecules is about 24 % of unit cell volume^{9, 10} 8.5 % of practical

weight loss was observed in TGA, which corresponds to the loss of one DMF molecule (theoretical value is 8.4 %).

Removal of the guest molecules in **4** results in a three-dimensional (3D) porous structure and the SBU is a paddle-wheel $\text{Zn}_2(\text{COO})_4(\text{bpy})_2$ unit as shown in Scheme 1. Each paddle-wheel SBU is linked by obba to form a distorted 2D net. The C-O-C angle of the obba molecules in the 2D net is 117.227° . Each SBU is connected to another SBU via bpy to give rise to a 3D framework. Two pairs of SBU in diagonal position (i.e 1-3 and 2-4 in scheme 1) have very different direction. The SBUs of pair 2 and 4 are pointing nearly up and down ward while the SBUs of pair 1 and 3 are pointing out of the paper plane. The closest C-C distance between lateral obbas of 2D net was measured $\sim 10\text{\AA} \times \sim 18\text{\AA}$. Since this structure is doubly interpenetrated and another SBU is connected to SBU3 and SBU4 and located in the center of this 2D net. Thus, actual pore size is almost half of that of the 2D net, i.e. approximately $\sim 5\text{ \AA}$ with consideration of the VDW's radius of carbon.



Scheme 1. The paddle-wheels of $\text{Zn}_2(\text{COO})_4(\text{bpy})_2$ SBU and the resultant 2D net. (Zn; green, O; red, C;gray and N;blue. H is omitted for clarity)

Preparation of $[\text{Cu}_3(\text{BTC})_2(\text{H}_2\text{O})_3]$ (**5**).

The preparation of $[\text{Cu}_3(\text{BTC})_2(\text{H}_2\text{O})_3]$ (**5**) was a slight modification of the synthesis reported by Chui et al.¹² $\text{Cu}(\text{NO}_3)_2 \cdot 3\text{H}_2\text{O}$ (98%, Aldrich) and trimesic acid or BTC (Aldrich, 95%) were used as received without further purification. Blue crystals of **5** were obtained from the reaction of $\text{Cu}(\text{NO}_3)_2 \cdot 3\text{H}_2\text{O}$ (0.435 g, 1.8 mmol) dissolved in 6 mL of de-ionized water with trimesic acid or BTC (0.110 g, 0.5 mmol) dissolved in 6 mL of ethanol. Subsequently, the solution was transferred into a Teflon-lined autoclave and heated in an oven at 353 K for 19 hours. The synthesis of **5** by Chui et al. at 453 K under hydrothermal conditions also generated a Cu_2O phase as impurity.¹² The lowering of the reaction temperature improved crystal quality without producing impurities.^{13, 14}

Preparation of 2D $[\text{Co}(\text{ox})(\text{bpy})]$ (**6**) and $[\text{Ni}(\text{ox})(\text{bpy})]$ (**7**).

CoCl_2 (Alfa Aesar, 99+%), NiCl_2 (Alfa Aesar, 99+%), bpy (Acros, 98%), and $\text{Na}_2\text{C}_2\text{O}_4$ (Alfa Aesar, 99%) were used as received without further purification. Coral plate crystals of **6** were prepared by a hydrothermal reaction of CoCl_2 (0.1297 g), bpy (0.1562 g), sodium oxalate (0.1340 g), and H_2O (8 mL) in a molar ratio of 1:1:1 at 170°C for 4 days.¹⁵

Light blue plate crystals of **7** were grown from the hydrothermal solution reaction containing NiCl_2 (0.1296 g), bpy (0.1562 g), sodium oxalate (0.1340 g), and H_2O (8 mL) in the molar ratio of 1:1:1. Under identical experimental conditions the reactions generated single-phased polycrystalline compounds of **6** and **7**.

Gas Sorption Measurements

The gas adsorption-desorption experiments were conducted using an automated micropore gas analyzer Autisorb-1 MP (Quantachrome Instruments). The cryogenic temperatures were controlled using liquid argon and liquid nitrogen at 87 K and 77 K, respectively. The initial outgassing process for each sample was carried out under vacuum at 373 K for 16~18 hours. About 0.05~0.10 g of activated samples were used for gas sorption studies. The weight of each sample was recorded before and after outgassing to confirm of the removal of guest molecules. The outgassing procedure was repeated with the same sample for an hour after collection of each isotherm. The total analysis times were ca. 60~130 hours for Ar sorption and 7~9 hours for hydrogen sorption. Ultra high purity of compressed H₂ gas (UHP 5.0) and nitrogen gas (UHP 5.0) were used for analysis. The pore properties including pore volume, pore size, and surface area were analyzed using the Autosorb v1.50 software.

2.3 Results and Discussion

Gas Sorption of $[\text{Zn}_3(\text{bpdc})_3\text{bpy}]$ (**1**) and $[\text{Co}_3(\text{bpdc})_3\text{bpy}]$ (**2**).

To experimentally evaluate the pore characteristics of the two structures and to analyze their hydrogen adsorption properties, as well as to understand the differences in their pore structures, extensive gas adsorption studies were performed at cryogenic temperatures (77 K and 87 K). The purity of both polycrystalline samples was confirmed by PXRD and their thermal stability was validated by thermogravimetric (TG) analysis.

Both compounds showed clearly a two-stage weight loss at $\sim 200^\circ\text{C}$ and $\sim 400^\circ\text{C}$. The weight loss around 200°C was 21% for **1** and 22% for **2**, respectively, in agreement with the calculated amount of guest molecules. The start of decomposition of **1** and **2** occurred at 384°C and 400°C , respectively, which was confirmed by the PXRD analysis.

Ar was selected for the characterization of pore properties of both **1** and **2** mainly for the following reasons. First of all, Ar has a smaller kinetic diameter (3.4 Å) than N_2 (3.64 Å), and thus, Ar can penetrate smaller pores.¹⁶ Secondly, interactions of Ar with solids are non-specific, while the N_2 molecule has a permanent quadrupole moment and thus interacts specifically with external electric field of the solid. These interactions increase the effective adsorption energy of N_2 and shift adsorption isotherms of N_2 to lower relative pressures compared to Ar. Specific interactions of N_2 contribute also to its smaller diffusion rates into micropores. Such an effect becomes significant for structures having very small pore diameters.

The Ar adsorption-desorption isotherms of both compounds are depicted in Figure 2.3a. A PXRD analysis was performed on all samples before and after the adsorption

measurements to ensure the purity and structure integrity. The results obtained are highly reproducible and represent a well defined measure of the hydrogen and argon adsorption capacity. The argon sorption follows a typical Type I isotherm with an estimated BET surface area of 793 and 779 m²/g for **1** and **2**, respectively. Both compounds showed a tiny hysteresis at $P/P^\circ > 0.4$ atm which is typically a result of intercrystalline voids in other MOF material.¹⁴ Both compounds also exhibited a rather large low pressure hysteresis at $P/P^\circ < 0.05$ for **2** and $P/P^\circ < 0.05$ for **1**, with that in **2** much more significant. This is believed to originate from the change in volume of the adsorbent.^{17, 18}

The micropore volume can be estimated from Figure 2.3b. It was determined by the least square method in the pressure range of $0.3 < P/P^\circ < 0.8$, and the values were 0.31cc/g for **1** and 0.34cc/g for **2**, respectively. The micro pore volume, which was calculated based on their argon isotherm data, is consistent with above observations, giving values of 0.32 cc/g for **1** and 0.38 cc/g for **2** (at $P/P^\circ = 0.95$) , respectively.

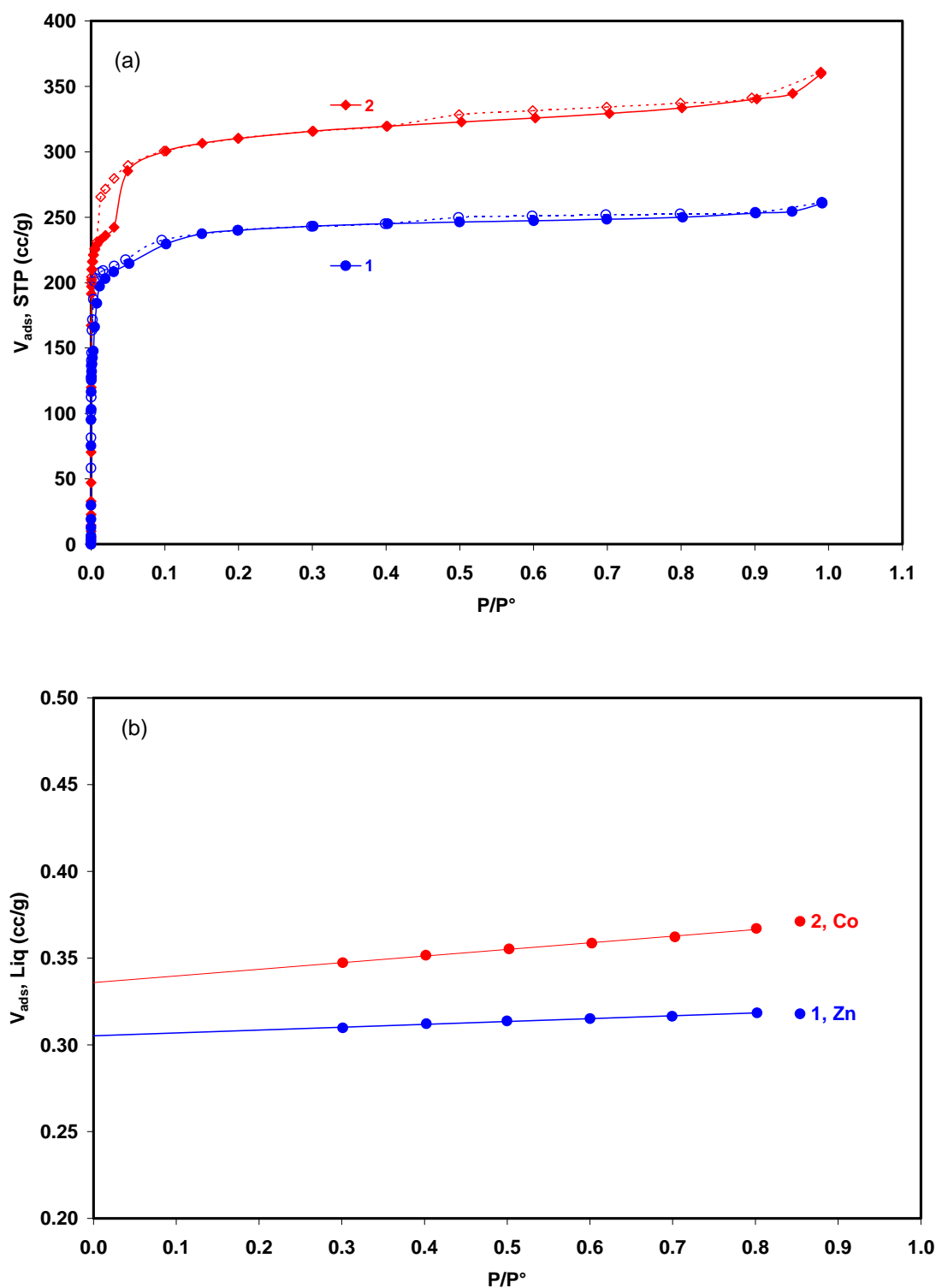


Figure 2.3 The Ar adsorption (blue) and desorption (red) isotherms on **1** and **2** obtained at 87K (a) in V (STP, cc/g) condition and (b) in V (Liq, cc/g) in the range of $0.3 < P/P^\circ < 0.8$ for pore volume calculation.

Depicted in Figure 2.4a is the pore size distribution based on the Horvath-Kawazoe (H-K) model.¹⁹ This analysis shows that two types of pores exist in **1**. A large portion of these pores have a pore diameter ~ 6.5 Å, which falls in the range of ultramicropores (pore diameter < 7 Å). A small portion of the pores have a pore diameter of about 10 Å, falling in the range of supermicropores (pore diameter within 7-20 Å). These data are consistent with the dimensions estimated based on the single crystal structure of **1**. Similarly, the Horvath-Kawazoe (H-K) model gives two types of pores for **2**: ultramicropores (diameters ~ 6.9 Å) and supermicropores (diameters ~ 15 Å).¹⁸ While we expect a small difference in their supermicropore dimension because of the difference in the channel structures of **1** and **2**, in which the 6-membered rings consisting of the internal wall of the 1D channels in **1** are rotated somewhat more into the channels than they are in **2**, so that the channels in **1** have more atoms “sticking into the voids”, resulting in a reduced pore dimension, the pore diameter of 15 Å determined from the H-K model is significantly larger than that estimated from the crystal structure of **2**.

The hydrogen adsorption-desorption isotherms for **1** and **2** at 77 K and 87 K are plotted in Figure 2.4b. It is interesting to see a difference in the hydrogen uptake in the two structures even though their main open channels have very similar size. The Co structure (**2**) adsorbs more hydrogen than the Zn structure (**1**) at both temperatures and all pressure levels. This difference is in agreement with the difference of total micropore volume obtained from Ar adsorption data. At 87 K and 1 atm, the values are 1.02 and 1.13 wt% for **1** and **2**, respectively. At 77 K, they are 1.39 and 1.51 wt% for **1** and **2**, respectively. No hysteresis was observed in these hydrogen isotherms.

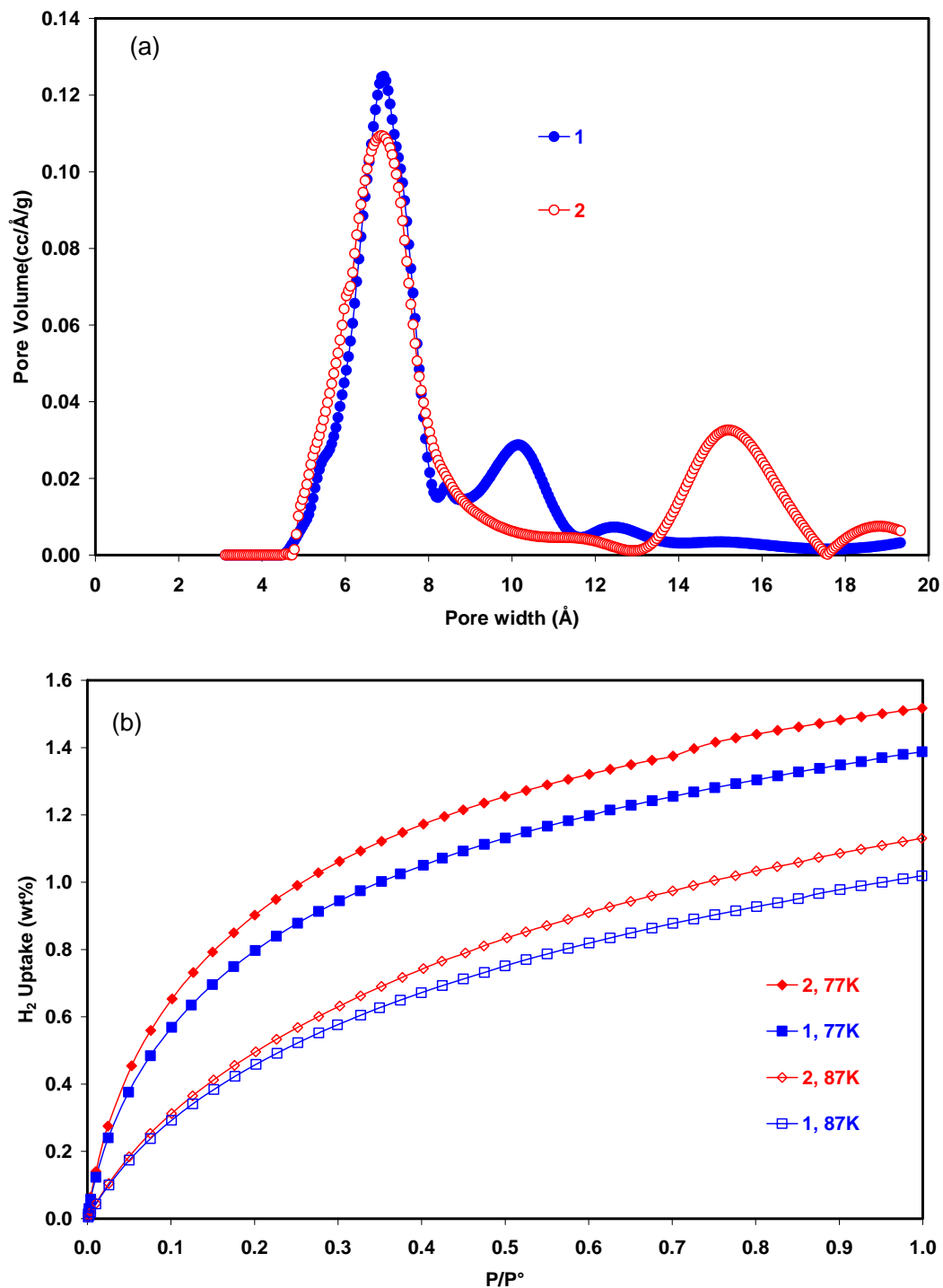


Figure 2.4. (a) Pore size distribution of [Zn₃(bpdc)₃bpy] (1) and [Co₃(bpdc)₃bpy] (2) calculated from Horvath-Kawazoe (H-K) Model and (b) their hydrogen adsorption isotherms at 77 K and 87 K.

Note that the hydrogen uptakes at these temperatures are among the highest gravimetric densities of porous metal organic structures reported thus far.²⁰⁻²⁵ The amount of hydrogen adsorbed in both **1** and **2** are much higher than those of ZSM-5 (0.7 wt%)^{26, 27} and H-SSZ-13 (1.28 wt%).²⁸ The latter was recently reported to have the highest uptake value of hydrogen among zeolite materials. It is also worth noting that the densities of the adsorbed H₂ at 77 K and 1 atm are 0.040-0.042 g/cc in **1** and **2**, calculated based on the estimated pore volumes using Ar sorption data at 87 K. These values represent the highest densities of H₂, obtained at 77 K and 1 atm, in any porous metal organic framework structures reported thus far²⁰⁻²⁵ and are slightly lower than those of liquid H₂ (e.g. 0.053 g/cc at 30 K and 8.1 atm, or 0.03 g/cc at critical point 33 K and 13 atm).²⁹ The isosteric heat of adsorption (Q_{st}) is a differential quantity based on the Clausius-Clapeyron equation.³⁰ It is related to the energy of H₂ adsorption and can be considered a measure of the extent of sorbent-sorbate interactions in a porous material. The Q_{st} values can be calculated using hydrogen adsorption isotherms measured at different temperatures. A calculation of the isosteric heat of hydrogen adsorption in both **1** and **2** using 77 K and 87 K isotherms was performed. The calculated Q_{st} data represent the first set for metal carboxylate framework structures and they are plotted in Figure 2.5. The Q_{st} values are higher for **2** than for **1** over the weight range of 0.05~0.82%, indicative of somewhat stronger sorbent-sorbate interactions, and thus, higher energy of hydrogen adsorption, in **2**. However, the Q_{st} values at lowest coverage are very close to each other and are 7.1 kJ/mol for **2**, and 7.3 kJ/mol for **1**, respectively. The Q_{st} values of both **1** and **2** decrease as the hydrogen uptake increases.

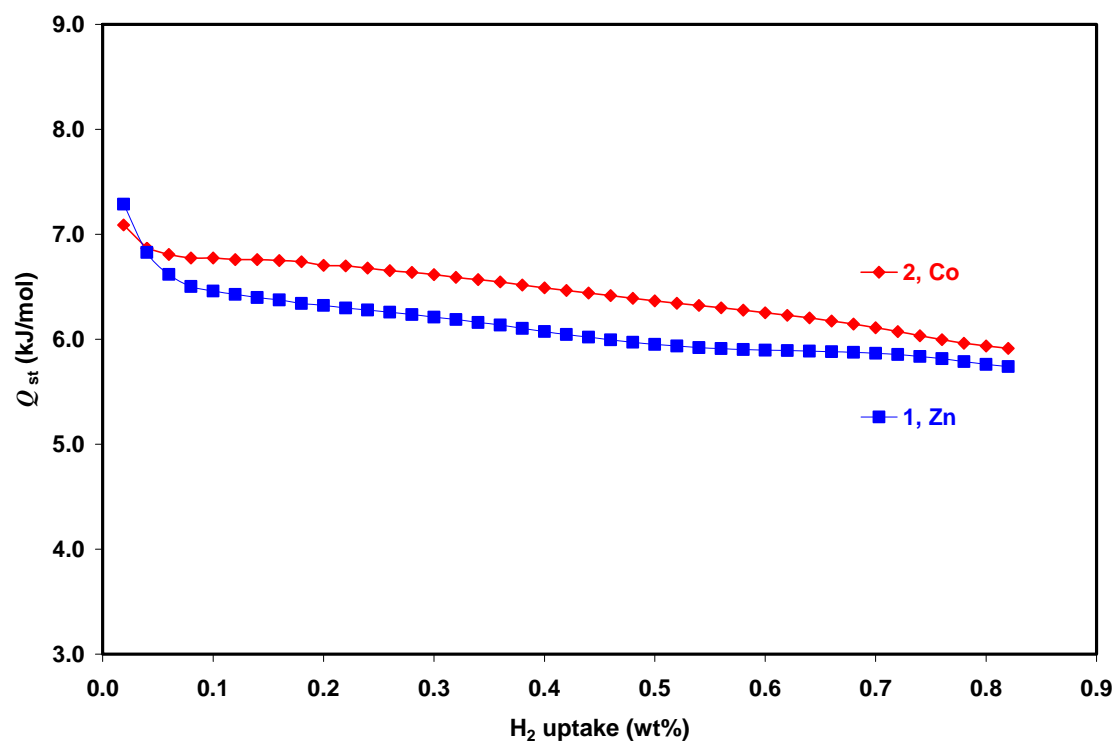


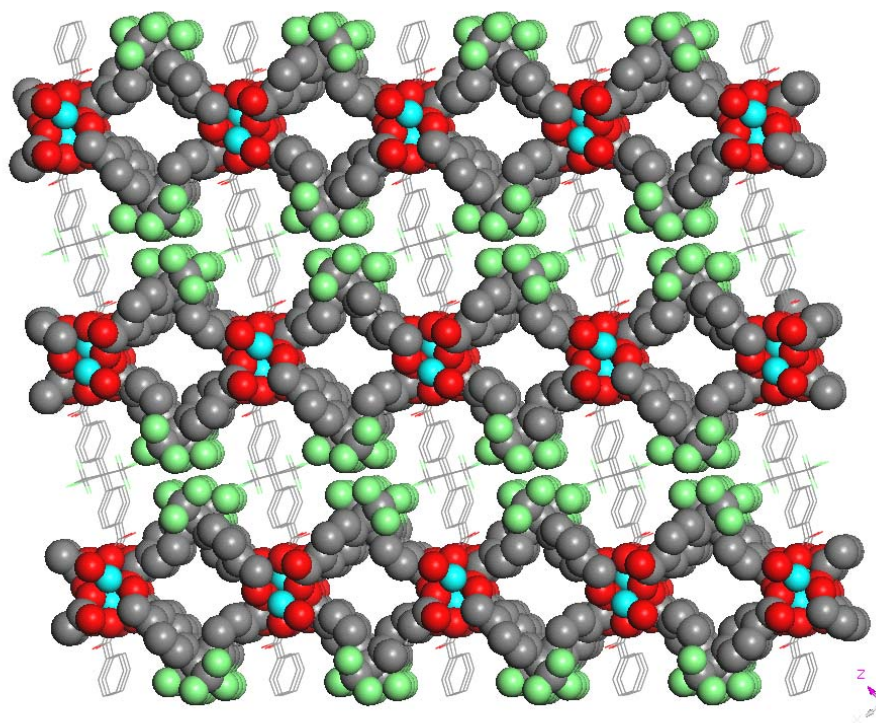
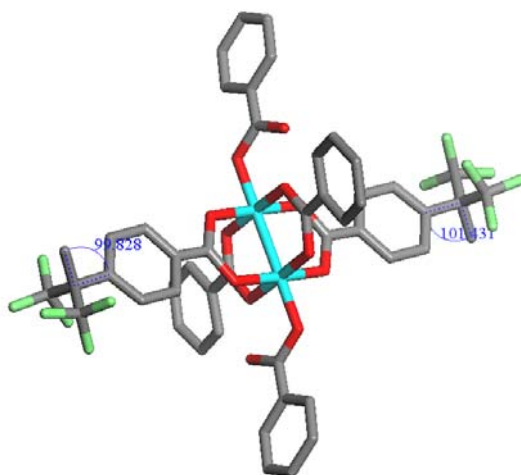
Figure 2.5 Isosteric heat of H₂ adsorption for **1** and **2**, respectively, as a function of the amount of hydrogen adsorbed.

Gas Sorption of [Cu(hfipbb)(H₂hfipbb)_{0.5}] (**3**)

The SBU and crystal structure of **3** are shown in Figure 2.6a. The SBU of **3** is a di-copper paddle wheel and the SBU connected to other SBU to form diamond shape of 1D open ultramicrochannel layer via two hfipbb ligands, which are bent with an angle (C-C(CF₃)₂-C) of 99.8° and 101.4° in horizontal direction. The ultramicrochannels are formed by alternating smaller windows and larger cages. These open channel layers are connected to another open channel layer via H₂hfipbb ligand, which has a 103.7° angle in C-C(CF₃)₂-C to form 3D frameworks. The dimensions of the small windows are ~3.5×3.5 Å (calculated based on the van der Waals radius of carbon), and the dimensions of the larger cages are ~5.1×5.1 Å.

The 20 m²/g of BET surface area and 0.03 cc/g of pore volume were obtained based on argon isotherm at 87 K as shown in Figure 2.6b. The hydrogen adsorption-desorption isotherms were measured on **3** at two cryogenic temperatures, 77 K and 87 K. However, isotherm at 87 K is only plotted in Figure 2.6c because isotherm at 77 K shows slightly less hydrogen uptake than that of isotherm at 87 K in the pressure range above P/P°=0.05 to P/P°=1.0. Strong hysteresis was observed at all pressure levels and the extent decreases as the temperature increases. This behavior is very different from that of **1** and **2** and is most likely a result of much smaller pore dimensions in **3**.⁸ The maximum value of hydrogen uptake is 0.23 wt% at 87 K and 1 atm. Note that the density of adsorbed hydrogen at 87 K is 0.033 g/cc, as calculated based on the estimated pore volume of 0.07 cc/g.⁵ The relatively smaller *Q*_{st} compared to those of **1** and **2** was obtained to be 4.24 kJ/mol at the lowest H₂ uptake at 0.006 wt%, indicating weak interaction between H₂ and compound **3**.

(a)



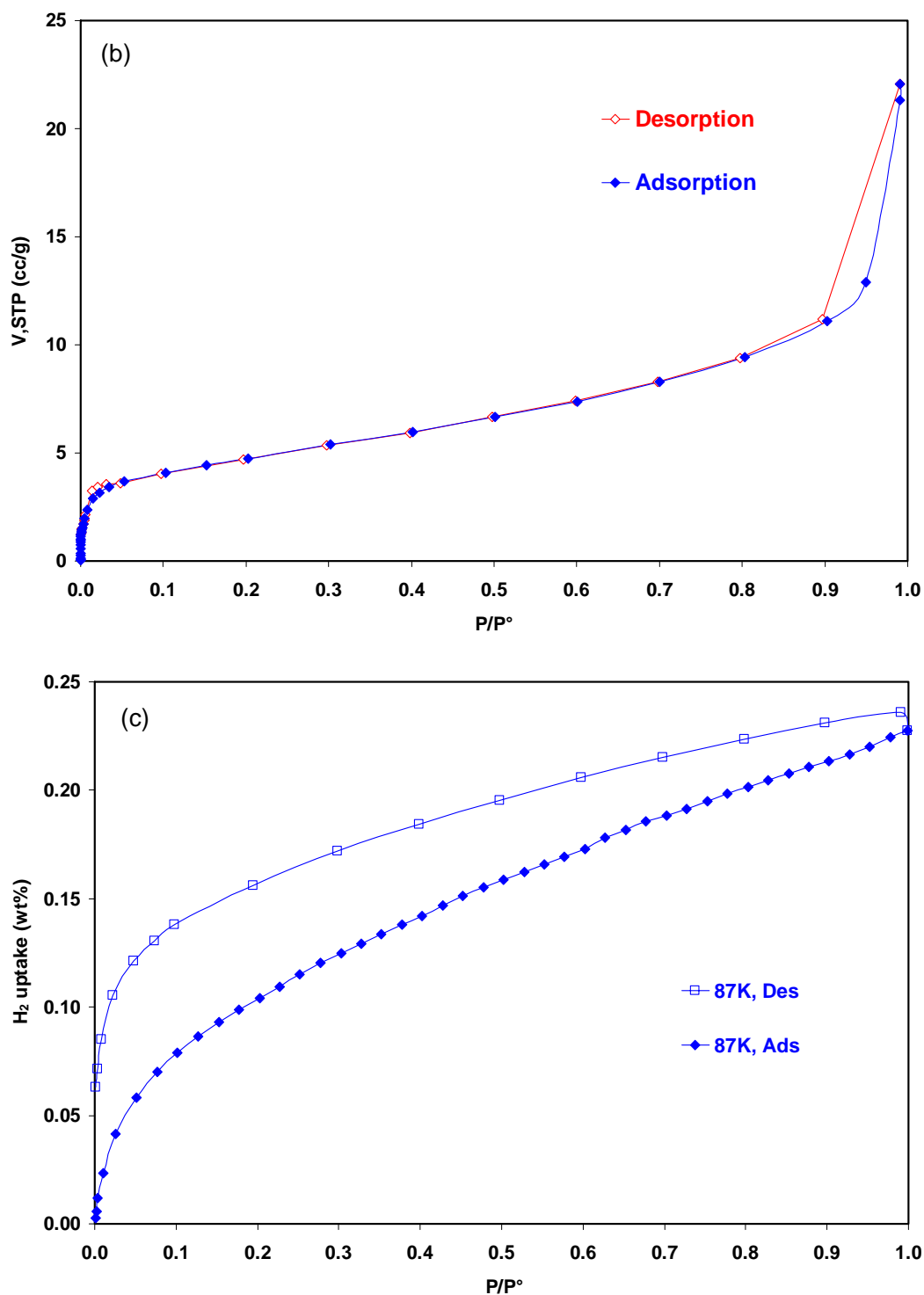
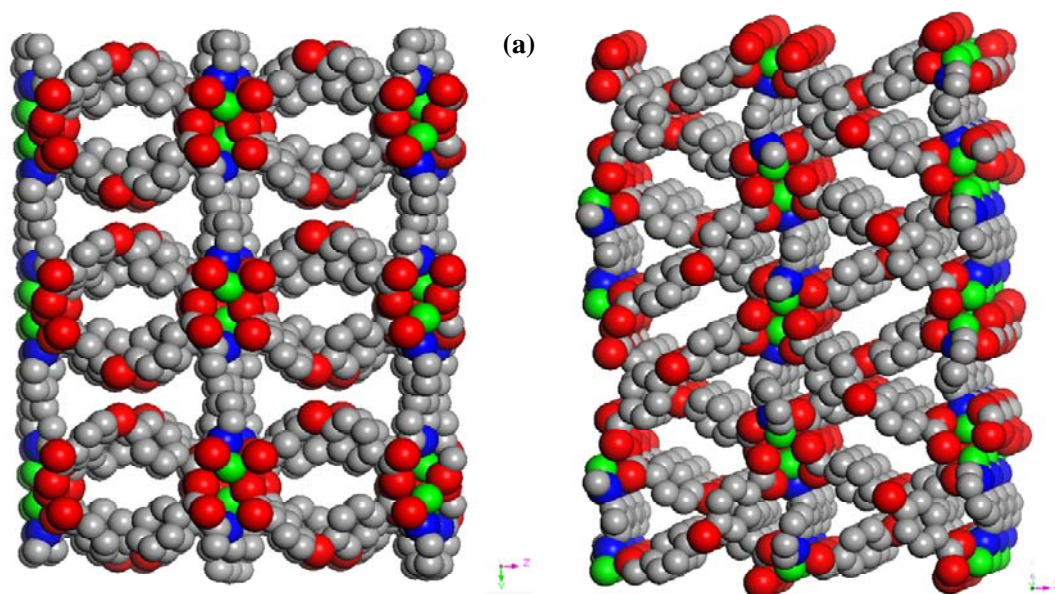


Figure 2.6. (a) The SBU (top) and three dimensional (3D) ultramicrochannel structure (bottom) of $Cu(hfipbb)(H_2hfipbb)_{0.5}$ (**3**). In the figure, Cu is shown in cyan, F is shown in green, O is shown in red, C is shown in gray and H is omitted for clarity. (b) The Argon isotherm at 87K and (c) hydrogen adsorption-desorption isotherms on **3** at 87K.

Gas Sorption of $[\text{Zn}_2(\text{obba})_2(\text{bpy})]\cdot\text{DMF}$ (**4**).

The crystal structure of **4** is shown in Figure 2.7a. There are interconnected channels along the crystal axis *a* (left) and *b* (right) formed by alternating smaller windows in the same fashion as in crystals of **3**. The dimensions of the small windows formed by obba are ~ 5.4 Å (O-O in horizontal direction) and the width of the sand watch shaped pores (left) are ~ 8.8 Å (C-C distant of lateral bpy) calculated based on the van der Waals radius of oxygen and carbon. Due to the concave shape of the sand watch shaped pores, the actual pore size is half of the longer width i.e. ~ 4.4 Å. The dimension of the windows along with *b* axis is ~ 3.6 Å measured from longest C-C distance. Therefore, the pore size of compound **4** is in the range of *ca.* 4~5 Å. As shown in Figure 2.7b, the argon isotherm at 87 K is a typical Type-I isotherm with 0.071cc/g of total pore volume and 58 m²/g of BET surface area.³¹ The hydrogen adsorption-desorption isotherms were collected on **4** at two cryogenic temperatures (77 K and 87 K), after activation at 150°C for 3 hours. The results are plotted in Figure 2.7c. A hysteresis was observed for the 77 K isotherm. This behavior is very different to **1** and **2**, but very similar to that of **3** and most likely a result of similar pore dimensions. The fully reversible uptake and release of hydrogen in the 3~5Å size porous materials would be not favorable.

The hydrogen uptakes are 0.46 wt% at 87 K and 1atm and 0.56 wt% at 77 K and 1atm, respectively. The values are higher than those of **3**. The Q_{st} is 6.2 kJ/mol and higher than that of **3**. Although **3** and **4** showed similar crystal pore sizes, the capability of hydrogen uptake by **4** is higher than that by **3**. This is in agreement with the difference of surface area and total pore volume between **3** and **4**.



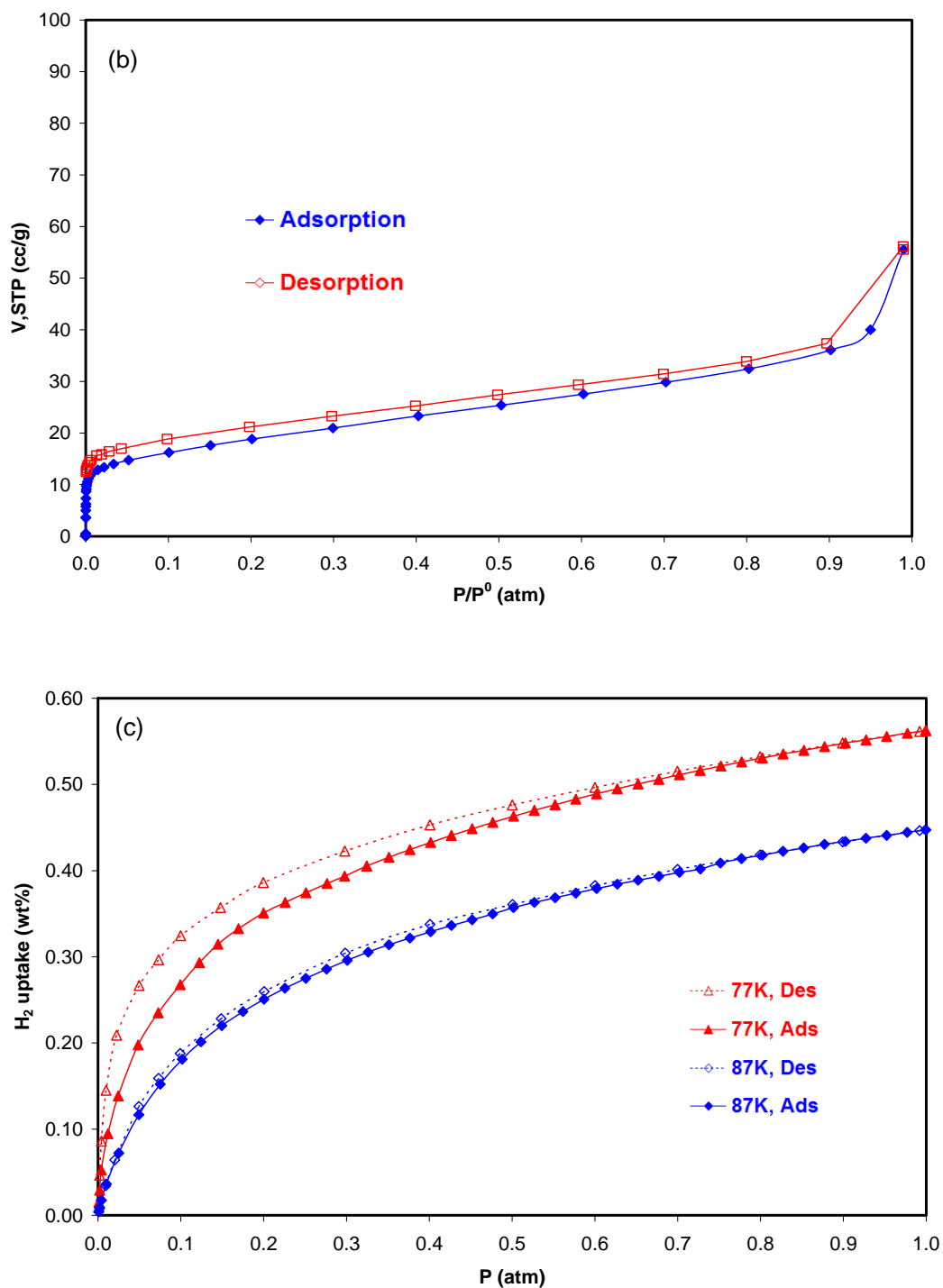


Figure 2.7 (a) The view of 1D open channel of **4**, along with crystal axis a (left) and axis b(right) In the figure, Zn is shown in green, N is shown in blue, O is shown in red, C is shown in gray and H is omitted for clarity. (b) The argon isotherm at 87K and (c) The hydrogen adsorption-desorption isotherms on $[Zn_2(obba)_2(bpy)]$ (**4**) at 77 and 87K.

Gas Sorption of $[\text{Cu}_3(\text{BTC})_2(\text{H}_2\text{O})_3]$ (**5**).

The crystal structure of $[\text{Cu}_3(\text{BTC})_2(\text{H}_2\text{O})_3]$ (**5**) is shown in Figure 2.8. The sorption properties for N_2 , O_2 , CO , CO_2 , N_2O , CH_4 , ethylene, ethane, n-dodecane, as well as water and a simulation study of Ar adsorption on **5** have been reported previously.^{32, 33} The hydrogen sorption study has been reported by us for the first time in 2005.³⁴

The compound **5** was activated at 170°C for 4 hours under vacuum. Before activation, the compound was immersed in dichloromethane (DCM) for 72 hours. The Ar isotherms of **5** were obtained at 87 K at pressures ranging from $p < 10^{-6}$ to $p = 1$ atm. The results are shown in Figure 2.9. Two different types of pores are observed in the Ar sorption isotherm: central channels and outside pockets as claimed by Vishnyakov et al.¹⁴ The pore size distribution data obtained using the H-K method¹⁹ confirm that there are two different pores: ultramicropores, which have diameters of ~ 6 Å, and supermicropores with ~ 8 Å diameters. The pore volume was estimated to be 0.40 cc/g. The hydrogen uptake of **5** are 1.07 wt% at 87 K, 1 atm and 1.44 wt % at 77 K, 1 atm . The 77 K isotherm is compared in Figure 2.10 along with those of 3D MMOFs. The adsorbed hydrogen density is 0.036 g/cc, within the range of liquid hydrogen density, 0.03-0.076 g/cc.²⁹ The extent of gas-solid interactions can be assessed using the isosteric heat of adsorption, Q_{st} , which is based on Clausius-Clapeyron equation.^{35, 36} The calculated isosteric heats of hydrogen adsorption are in the range of 6~7 kJ/mol, which is significantly higher than the enthalpy of vaporization of H_2 (0.99 kJ/mol at its boiling point). They are also similar to those calculated for compound **1** and **2**. This indicates a strong hydrogen-adsorbent interaction within the pores.⁸

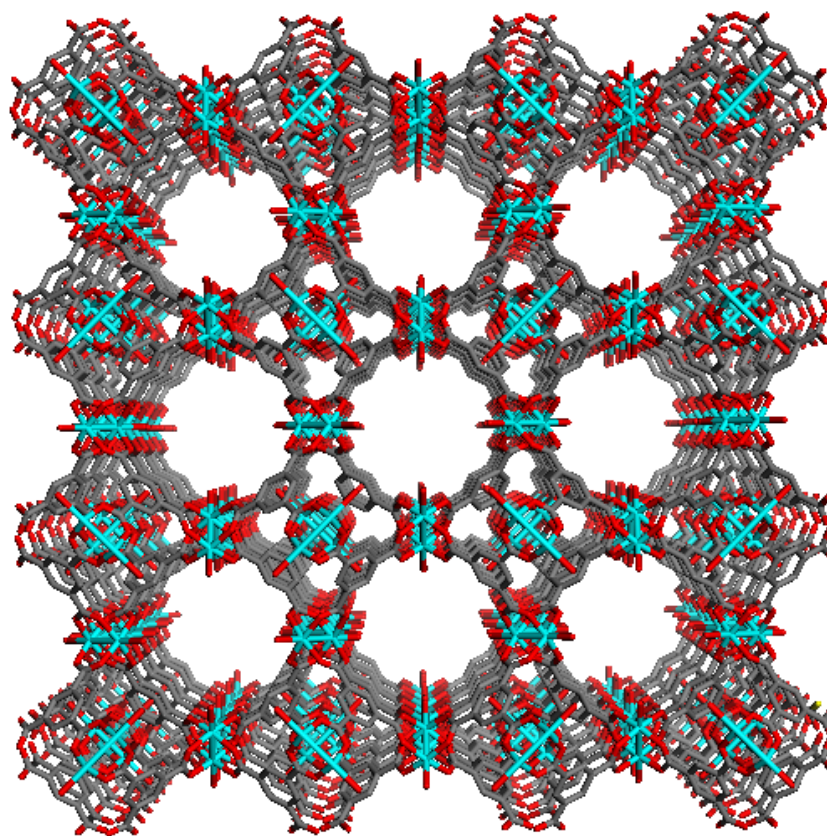


Figure 2.8 The crystal structure of $\text{Cu}_3(\text{BTC})_2(\text{H}_2\text{O})_3$ (**5**). The water molecules were located at the top and bottom of di-copper paddle wheel SBU (see Figure 1.2a) and could be removed by heating around 170°C without structural collapse. This removal of water resulted in open metal sites³⁷ and is confirmed by color change from aqua blue to dark blue. In the figure, Cu is shown in cyan, O is shown in red, C is shown in gray and H is omitted for clarity.

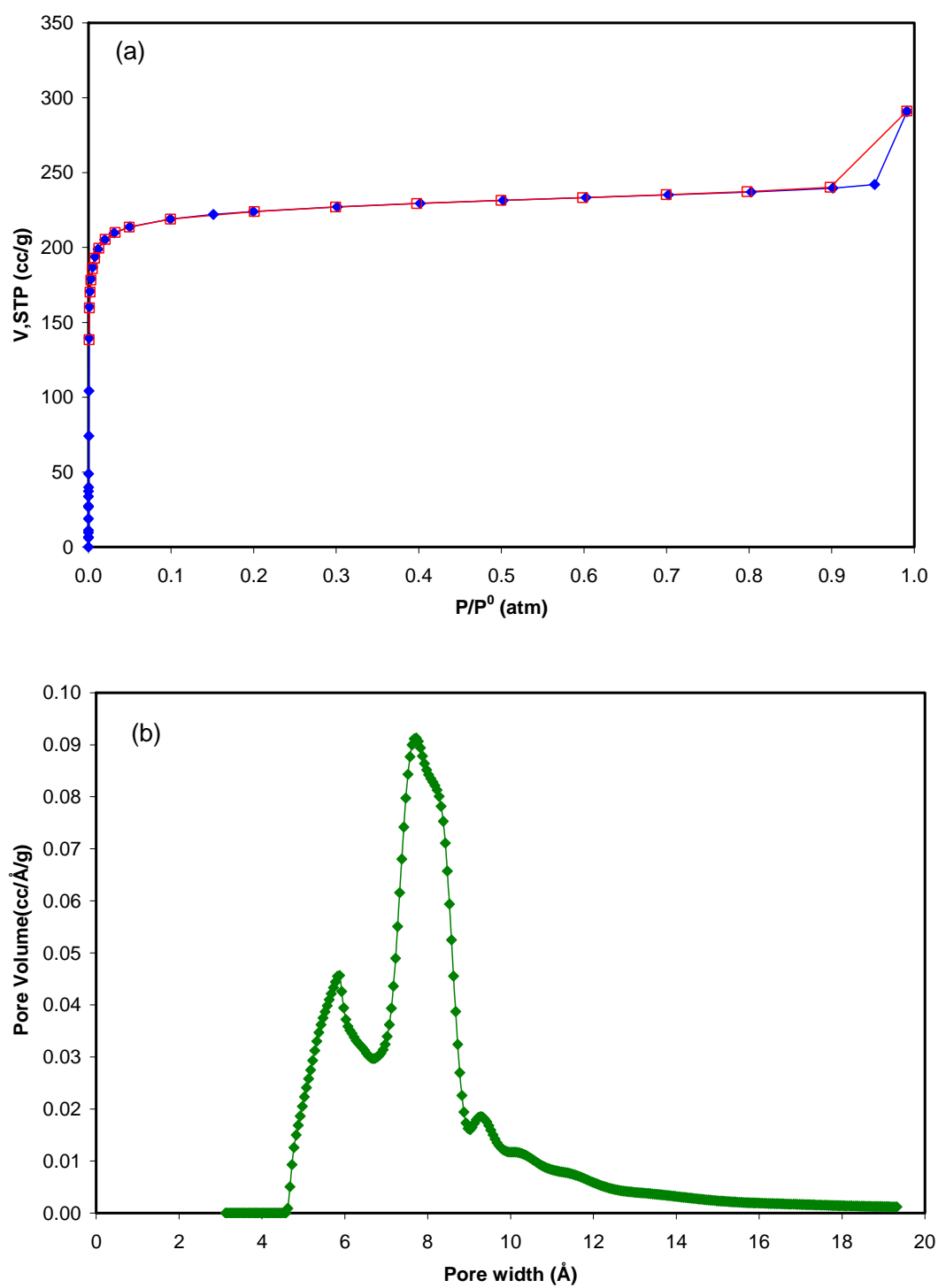


Figure 2.9 (a) The argon adsorption (Blue)-desorption(Red) isotherms of **5** at 87 K and (b) HK pore size distribution showed two different size of pores.^{14, 38}

Gas Sorption of 2D [Co(ox)(bpy)] (**6**) and [Ni(ox)(bpy)] (**7**)

The two-dimensional (2D) iso-structures of **6** and **7** were selected for a gas sorption study and were compared with 3D porous structures. Both structures contain octahedrally coordinated metal centers bonded to two oxalate and two bpy ligands to form a two-dimensional layered network with an interlayer distance of 5.3~5.5 Å.¹⁵

Contrary to the three-dimensional structures **1-2** and **4-5**, compound **6** and **7** demonstrate very low hydrogen sorption capability. The argon sorption on compound **6** showed 5 m²/g of BET surface area. The hydrogen uptakes at 77 K is 0.10 wt% for **6** and 0.16 wt% for **7**, respectively, which is significantly lower than those of **1-5**. The hydrogen adsorption-desorption isotherms measured at 77 K are shown in Figure 2.10, along with those of 3D MMOFs. Note that small pore material of **4** and the short distant layered materials of **6** and **7** exhibit strong hysteresis in their adsorption-desorption isotherms.

The common property of compound **4**, **6**, and **7** is that the pore size or layer distance is smaller than 6 Å. Compound **1**, **2** and **5** have no hysteresis and they have at least 6 Å or bigger size of pores. It clearly shows that pore size is very important for the release of hydrogen from the pore in the desorption process.

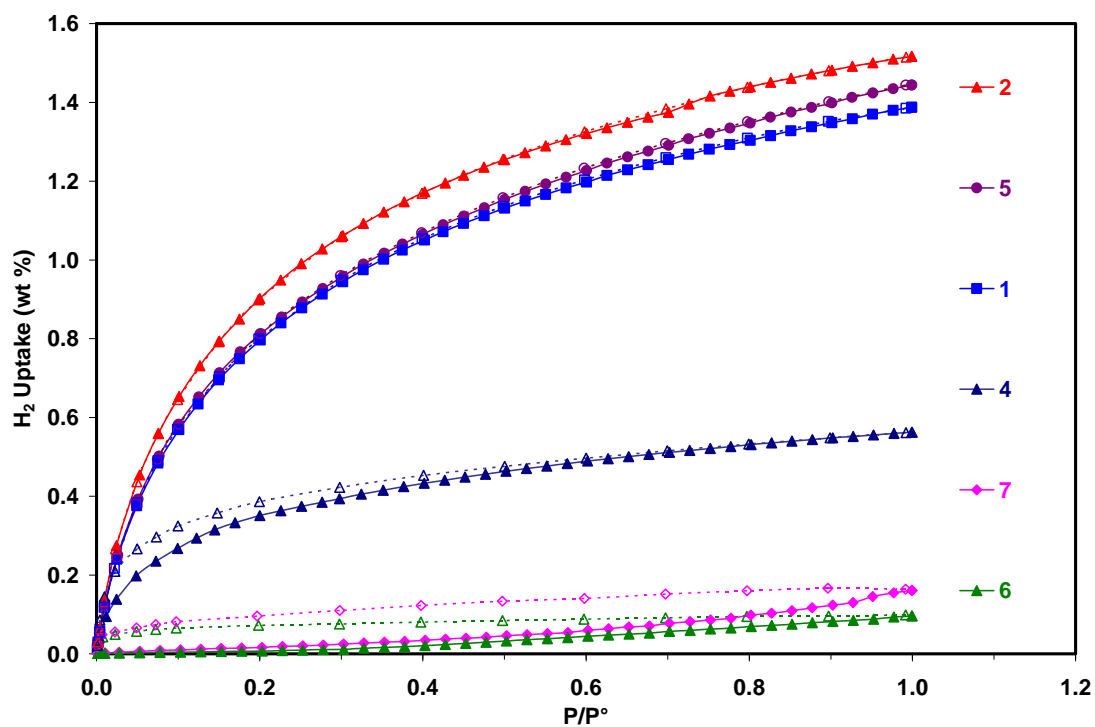


Figure 2.10 The hydrogen adsorption-desorption isotherms on **1-2** and **4-7** at 77 K. All solid marks of each isotherm denote adsorption and empty marks represent desorption.

The volumetric uptake (g/L) of hydrogen can be calculated based on the gravimetric uptake (wt%) of hydrogen using the activated crystal density.

For example for **2**. (at 1 atm, 1.51 wt% , activated crystal density =1.158 g/mL)

$$Volumetric_H_2_uptake = 15.1 \frac{mg}{g} \times 1.158 \frac{g}{mL} = 17.5 \frac{g}{L}$$

The calculated volumetric uptake results for **1 ~ 7** are shown in Figure 2.11. The highest observed value was 18 g/L for **2**. However, these adsorbed hydrogen uptake profiles did not show saturation at 1 atm, therefore, an even higher hydrogen uptake would be expected at higher pressure.

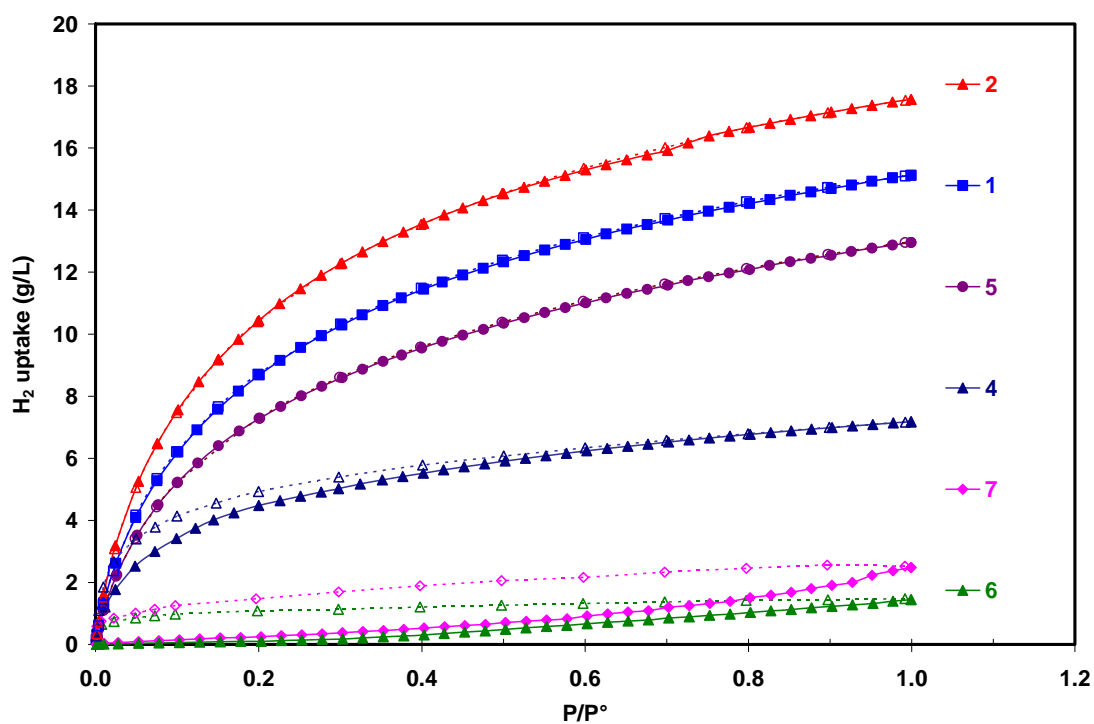


Figure 2.11 The adsorbed hydrogen uptake on **1-2** and **4-7** at 77K. All solid marks of each isotherm denote adsorption and empty marks represent desorption.

2.4 Conclusions

In summary, the investigation of argon and hydrogen adsorption properties of five 3D MMOFs (**1-5**) and two 2D layered structures (**6-7**) at low temperatures has revealed interesting observations.

The hydrogen uptakes (wt%) at 77 K and 1 atm are 1.51 wt%, 1.39 wt% and 1.44 wt% for **1**, **2** and **5**, respectively. This study also suggests that the difference in the H₂ uptake between the two structures can be attributed to their pore volumes (0.32 and 0.38 for **1** and **2**, respectively) as well as the extent of gas–solid interactions, which is indicated by the isosteric heats of adsorption, calculated based on Clausius-Clapeyron equation and reported for the first time⁸ for carboxylate-based metal organic structures. However at least 6 Å size pores are required for reversible adsorption-desorption of hydrogen.

The densities of adsorbed hydrogen at low pressure and low temperature are in a similar range of what we have seen in the literature review in chapter one. The isotherms are not saturated at low pressure and low temperature. This study proposes that high pressure hydrogen studies are necessary to achieve saturated isotherms.

2.5 References

1. DOE(US) Fuel Cells, and Infrastructure Technologies Program in **2002**. (http://www.eere.energy.gov/hydrogenandfuelcells/pdfs/33098_toc.pdf)
2. Wigley, T. M. L.; Richels, R.; Edmonds, J. A., Economic and environmental choices in the stabilization of atmospheric CO₂ concentrations. *Nature* **1996**, 379, (6562), 240-243.
3. Sailor, W. C.; Bodansky, D.; Braun, C.; Fetter, S.; van der Zwaan, B., NUCLEAR POWER: A Nuclear Solution to Climate Change? *Science* **2000**, 288, (5469), 1177-1178.
4. Turner, J. A., A Realizable Renewable Energy Future. *Science* **1999**, 285, (5428), 687-689.
5. Pan, L.; Sander, M. B.; Huang, X.; Li, J.; Smith, M.; Bittner, E.; Bockrath, B.; Johnson, J. K., Microporous metal organic materials: promising candidates as sorbents for hydrogen storage. *J. Am. Chem. Soc.* **2004**, 126, (5), 1308-1309.
6. Han, S. S.; Goddard, W. A., Lithium-Doped Metal-Organic Frameworks for Reversible H₂ Storage at Ambient Temperature. *J. Am. Chem. Soc.* **2007**, 129, (27), 8422-8423.
7. Pan, L.; Liu, H.; Lei, X.; Huang, X.; Olson, D. H.; Turro, N. J.; Li, J., RPM-1: a recyclable nanoporous material suitable for ship-in-bottle synthesis and large hydrocarbon sorption. *Angew. Chem. Int. Ed.* **2003**, 42, (5), 542-546.
8. Lee, J. Y.; Pan, L.; Kelly, S. P.; Jagiello, J.; Emge, T. J.; Li, J., Achieving High Density of Adsorbed Hydrogen in Microporous Metal Organic Frameworks. *Advanced Materials* **2005**, 17, (22), 2703-2706.
9. Spek, A. L., PLATON, An Integrated Tool for the Analysis of the Results of a Single Crystal Structure Determination. In *Acta Cryst. A*, 1990; Vol. 46, pp C-34.
10. Spek, A., Single-crystal structure validation with the program PLATON. In *J. Appl. Cryst.*, 2003; Vol. 36, pp 7-13.
11. Pan, L.; Parker, B.; Huang, X.; Olson, D. H.; Lee, J. Y.; Li, J., Zn(tbip) (H₂tbip= 5-tert-Butyl Isophthalic Acid): A Highly Stable Guest-Free Microporous Metal Organic Framework with Unique Gas Separation Capability. *J. Am. Chem. Soc.* **2006**, 128, (13), 4180-4181.
12. Chui, S. S.; Lo, S. M.; Charmant, J. P.; Orpen, A. G.; Williams, I. D., A chemically functionalizable nanoporous material. *Science* **1999**, 283, (5405), 1148-1150.

13. Schlichte, K.; Kratzke, T.; Kaskel, S., Improved synthesis, thermal stability and catalytic properties of the metal-organic framework compound Cu₃(BTC)₂. *Microporous and Mesoporous Materials* **2004**, 73, (1-2), 81-88.
14. Vishnyakov, A.; Ravikovitch, P. I.; Neimark, A. V.; Bulow, M.; Wang, Q. M., Nanopore Structure and Sorption Properties of Cu-BTC Metal-Organic Framework. *Nano Lett.* **2003**, 3, (6), 713-718.
15. Lu, J. Y.; Lawandy, M. A.; Li, J.; Yuen, T.; Lin, C. L., A New Type of Two-Dimensional Metal Coordination Systems: Hydrothermal Synthesis and Properties of the First Oxalate-bpy Mixed-Ligand Framework [M(ox)(bpy)] (M = Fe(II), Co(II), Ni(II), Zn(II); ox = C₂O₄²⁻; bpy = 4,4'-bipyridine). *Inorg. Chem.* **1999**, 38, (11), 2695-2704.
16. Breck, D. W., *Zeolite Molecular Sieves*. Wiley: New York, 1974.
17. Lowell, S.; Shields, J. E.; Thomas, M. A.; Thommes, M., Characterization of Porous Solids and Powders: Surface Area, Pore Size, and Density. *Characterization of Porous Solids and Powders: Surface Area, Pore Size, and Density* **2004**, 16, Chapter 4.
18. Sing, K. S. W.; Everett, D. H.; Haul, R. A. W.; Moscou, M.; Pierotti, R. A.; Rouquerol, J.; Siemieniowska, T., Reporting Physisorption Data for Gas/Solid Systems with special Reference to the Determination of Surface Area and Porosity. *Pure Appl. Chem* **1985**, 57, (4), 603-619.
19. Horvath, G.; Kawazoe, K., Method for Calculation of Effective Pore Size Distribution in Molecular Sieve Carbon. *J. Chem. Eng. Jpn.* **1983**, 16, (6), 470-475.
20. Dybtsev, D. N.; Chun, H.; Kim, K., Rigid and flexible: a highly porous metal-organic framework with unusual guest-dependent dynamic behavior. *Angew. Chem. Int. Ed.* **2004**, 43, (38), 5033-5036.
21. Dybtsev, D. N.; Chun, H.; Yoon, S. H.; Kim, D.; Kim, K., Microporous manganese formate: a simple metal-organic porous material with high framework stability and highly selective gas sorption properties. *J. Am. Chem. Soc.* **2004**, 126, (1), 32-33.
22. Kaye, S. S.; Long, J. R., Hydrogen Storage in the Dehydrated Prussian Blue Analogues M₃[Co(CN)₆]₂ (M = Mn, Fe, Co, Ni, Cu, Zn). *J. Am. Chem. Soc.* **2005**, 127, (18), 6506-6507.
23. Lee, E. Y.; Jang, S. Y.; Suh, M. P., Multifunctionality and crystal dynamics of a highly stable, porous metal-organic framework [Zn₄O(NTB)₂]. *J. Am. Chem. Soc.* **2005**, 127, (17), 6374-6381.

24. Lee, E. Y.; Suh, M. P., A robust porous material constructed of linear coordination polymer chains: reversible single-crystal to single-crystal transformations upon dehydration and rehydration. *Angew. Chem. Int. Ed.* **2004**, 43, (21), 2798-2801.
25. Rowsell, J. L. C.; Millward, A. R.; Park, K. S.; Yaghi, O. M., Hydrogen Sorption in Functionalized Metal-Organic Frameworks. *J. Am. Chem. Soc.* **2004**, 126, (18), 5666-5667.
26. Nijkamp, M. G.; Raaymakers, J. E. M. J.; van Dillen, A. J.; de Jong, K. P., Hydrogen storage using physisorption – materials demands. *Applied Physics A: Materials Science & Processing* **2001**, 72, (5), 619-623.
27. Weitkamp, J.; Fritz, M.; Ernst, S., Zeolites as media for hydrogen storage. *International Journal of Hydrogen Energy* **1995**, 20, (12), 967-970.
28. Zecchina, A.; Bordiga, S.; Vitillo, J. G.; Ricchiardi, G.; Lamberti, C.; Spoto, G.; Bjorgen, M.; Lillerud, K. P., Liquid Hydrogen in Protonic Chabazite. *J. Am. Chem. Soc.* **2005**, 127, (17), 6361-6366.
29. NIST, <http://www.nist.gov/>.
30. Clark, A., *Theory of Adsorption and Catalysis*. Academic Press: New York, 1970.
31. Brunauer, S.; Emmett, P. H.; Teller, E., Adsorption of Gases in Multimolecular Layers *J. Am. Chem. Soc.* **1938**, 60, (2), 309-319.
32. Wang, Q. M.; Shen, D.; Bülow, M.; Lau, M. L.; Deng, S.; Fitch, F. R.; Lemcoff, N. O.; Semanscin, J., Metallo-organic molecular sieve for gas separation and purification *Microporous and Mesoporous Materials* **2002**, 55, (2), 217-230.
33. Skoulidas, A. I., Molecular Dynamics Simulations of Gas Diffusion in Metal-Organic Frameworks: Argon in CuBTC. *J. Am. Chem. Soc.* **2004**, 126, (5), 1356-1357.
34. Lee, J.; Li, J.; Jagiello, J., Gas sorption properties of microporous metal organic frameworks. *Journal of Solid State Chemistry* **2005**, 178, (8), 2527-2532.
35. Shen, D.; Bülow, M.; Siperstein, F.; Engelhard, M.; Myers, A. L., Comparison of Experimental Techniques for Measuring Isosteric Heat of Adsorption. *Adsorption* **2000**, 6, (4), 275-286.
36. Anson, A.; Callejas, M. A.; Benito, A. M.; Maser, W. K.; Izquierdo, M. T.; Rubio, B.; Jagiello, J.; Thommes, M.; Parra, J. B.; Martinez, M. T., Hydrogen adsorption studies on single wall carbon nanotubes. *Carbon* **2004**, 42, (7), 1243-1248.

37. Chen, B.; Ockwig, N. W.; Millward, A. R.; Contreras, D. S.; Yaghi, O. M., High H₂ Adsorption in a Microporous Metal-Organic Framework with Open Metal Sites. *Angew. Chem. Int. Ed.* **2005**, 44, (30), 4745-4749.
38. Krawiec, P.; Kramer, M.; Sabo, M.; Kunschke, R.; Fröde, H.; Kaskel, S., Improved Hydrogen Storage in the Metal-Organic Framework Cu₃(BTC)₂. *Advanced Engineering Materials* **2006**, 8, (4), 293-296.

CHAPTER THREE

HIGH HYDROGEN ADSORPTION CAPACITY ON $[M(\text{BDC})(\text{TED})_{0.5}] \cdot 2\text{DMF} \cdot 0.2\text{H}_2\text{O}$ ($M=\text{Zn}^{2+}$, Co^{2+} , Ni^{2+} , Cu^{2+}) SYSTEM

3.1. Introduction

Development of porous materials with significantly improved storage and/or separation capability is an extremely important aspect in gas and fuel cell technologies. Recent work on a new type of sorbent materials microporous metal organic frameworks (MMOFs) has illustrated very interesting adsorption properties and has demonstrated technological importance in storage and separation of small gases and hydrocarbon molecules.¹⁻²²

The ability to rationally design and modify the crystal structures of MMOF materials is the key to achieving high adsorption capacity and selectivity to meet specific storage/separation needs and to increasing the potential for commercial applications. A successful strategy in forming porous structures with controlled topology, large pore volume and framework integrity is to make use of secondary building units (SBU) with different shapes, sizes and binding modes. For example, a family of highly porous MOFs have been constructed using $\text{Zn}_4\text{O}(\text{COO})_6$ as the SBU.^{1, 23} The octahedral geometry and 6-fold connectivity of this SBU leads to a cubic structure. The paddle-wheel unit,

$M_2(\text{COO})_4(\text{TED})_2$ ($M = \text{Zn, Co, Ni, and Cu}$), is another SBU with a slightly different topology and connectivity from $\text{Zn}_4\text{O}(\text{COO})_6$, typically resulting in a tetragonal (distorted cubic) structure when the two ligands at apical and equatorial positions are not identical.^{2, 3, 14, 21, 22} By simply varying the length of organic linkers, isostructural compounds with a range of pore space can be obtained with the same SBU.

Recently, we have investigated a number of microporous structures based on several different SBUs. They exhibit unique gas sorption behavior and high selectivity for adsorbing hydrocarbons.²⁴⁻³⁰ In this chapter, the synthesis, crystal growth and structural characterization of four microporous MOFs, $[\text{M}(\text{bdc})(\text{ted})_{0.5}] \cdot 2\text{DMF} \cdot 0.2\text{H}_2\text{O}$ ($M = \text{Zn, Co, Ni and Cu}$) ($\text{bdc} = 1,4\text{-benzenedicarboxylate}$, $\text{ted} = \text{triethylenediamine}$) and their argon, hydrogen sorption properties at cryogenic temperatures will be presented.

3.2 Experimental

Single crystals of $[\text{Zn}(\text{bdc})(\text{ted})_{0.5}] \cdot 2\text{DMF} \cdot 0.2\text{H}_2\text{O}$ (**8**) were grown by solvothermal reaction. A mixture of zinc (II) nitrate hexahydrate (0.156 g, 0.597 mmol), H_2bdc (0.102 g, 0.614 mmol), ted (0.036 g, 0.321 mmol) and 15 mL of DMF were transferred to Teflon-lined autoclave and heated in an oven at 120°C for 2 days. Single crystals of **8** (0.212 g, 83% yield) were isolated after filtering and washing the product by DMF (10 mL \times 3). The large scale samples were prepared by using the same molar ratio. A mixture of zinc (II) nitrate tetrahydrate (1.464 g), H_2bdc (0.960 g), ted (0.432 g) and 120 mL DMF was mixed in a 250 mL beaker. A sonic treatment was given to dissolve all solid chemicals until obtaining a clear solution in warm water bath. Then the solution was transferred into digestion bombs and heated at 150°C for overnight. Colorless single

crystals of $[\text{Zn}(\text{bdc})(\text{ted})_{0.5}] \cdot 2\text{DMF} \cdot 0.2\text{H}_2\text{O}$ (**8**) (1.950 g, 80.5% yield) were isolated after filtering and washing with 10 mL of DMF three times and drying under vacuum at 50°C.

Single crystals of $[\text{Co}(\text{bdc})(\text{ted})_{0.5}] \cdot 2\text{DMF} \cdot 0.2\text{H}_2\text{O}$ (**9**) were grown by solvothermal reactions. A mixture of cobalt (II) chloride hexahydrate (0.176 g, 0.605 mmol), H_2bdc (0.080 g, 0.482 mmol), ted (0.036 g, 0.321 mmol) and 10 mL of DMF were transferred to Teflon-lined autoclave and heated in an oven at 120°C for 2 days. Single crystals of **9** (0.109 g, 42% yield) were isolated after filtering and washing the product three times with 10 mL of fresh DMF. Gram scale of **9** was synthesized at the slightly higher temperature and longer time of reaction condition. A mixture of cobalt (II) chloride hexahydrate (2.160 g), H_2bdc (1.200 g), ted (0.432 g) and 100 mL DMF was mixed in a 250 mL beaker. A sonic treatment was given to dissolve all solid chemicals until obtaining a clear solution in warm water bath. Dark green crystals of $[\text{Co}(\text{bdc})(\text{ted})_{0.5}] \cdot 2\text{DMF} \cdot 0.2\text{H}_2\text{O}$ (**8**) (1.948 g, 50.2 % yield) were isolated after filtering and washing with 10 mL of DMF three times and drying under vacuum at 50°C.

Single crystals of $[\text{Ni}(\text{bdc})(\text{ted})_{0.5}] \cdot 2\text{DMF} \cdot 0.2\text{H}_2\text{O}$ (**10**) were grown by solvothermal reaction. A mixture of hexahydrate nickel (II) chloride hexahydrate (0.144 g, 0.621 mmol), H_2bdc (0.080 g, 0.482 mmol), ted (0.036 g, 0.321 mmol) and 7 mL of DMF were transferred to Teflon-lined autoclave and heated in an oven at 130°C for 2 days. Single crystals of **10** (0.220 g, 52% yield) were isolated after filtering and washing the product three times with 10 mL of fresh DMF. However, the size of single crystal of **10** was too small for single crystal X-ray diffraction study. Therefore the structure of crystal **10** was confirmed by refinement of PXRD analysis.

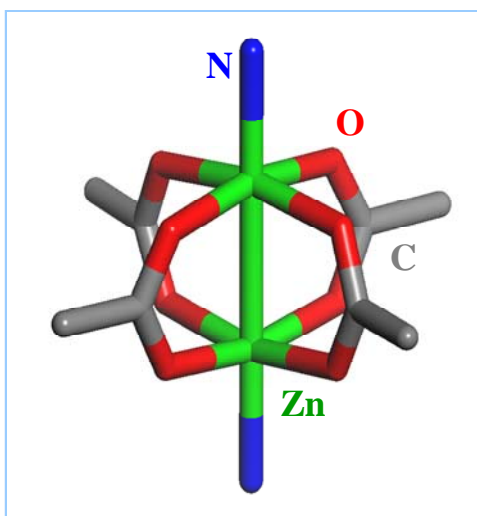
The PXRD analysis also was applied on poly crystal of $[\text{Cu}(\text{bdc})(\text{ted})_{0.5}] \cdot 2\text{DMF} \cdot 0.2\text{H}_2\text{O}$ (**11**) and confirmed that the structure of the powder samples of **11** is identical to that of the single-crystal study. $[\text{Cu}(\text{bdc})(\text{ted})_{0.5}] \cdot 2\text{DMF} \cdot 0.2\text{H}_2\text{O}$ was synthesized by mixing copper nitrate trihydrate (0.740 g), H_2bdc (0.680 g) and ted (0.480 g) with 150 mL of DMF in a 250 mL vessel. The vessel was then covered and heated at 120°C for 36 hours. A blue-colored crystalline powder formed. After filtering and washing with DMF (10mL \times 2), about 0.72 g of **2** (54.9 % yield) was collected.

Single crystal X-ray diffraction data of **8** and **9** were collected at 100 K on a Bruker-AXS Smart APEX CCD system with graphite-monochromatized Mo $\text{K}\alpha$ radiation ($\lambda = 0.71073 \text{ \AA}$). The multi-scan absorption and scaling in Bruker SAINT+ software (SADABS) were used. The structure was solved by direct methods and refined by full-matrix least-squares, using the Bruker SHELXTL package.^{31, 32}

The powder diffraction patterns of compound **10** and **11** were collected on a Rigaku D/M-2200T automated diffraction system (Ultima+) using Cu $\text{K}\alpha$ radiation. Measurements were made in a 2θ range of 5-50° at room temperature. The cell parameters of **10** and **11** were obtained using least-square refinement based on its PXRD pattern in *JADE* software (Version 3.0, 1996). The peak positions of $[\text{Ni}(\text{bdc})(\text{ted})_{0.5}] \cdot 2\text{DMF} \cdot 0.2\text{H}_2\text{O}$ were determined based on the space group and the cell parameters of **9** and those of $[\text{Cu}(\text{bdc})(\text{ted})_{0.5}] \cdot 2\text{DMF} \cdot 0.2\text{H}_2\text{O}$ were determined based on the space group and the cell parameters of **8** as starting parameters. The gas sorption studies were conducted via same procedures described in chapter 2.

3.3 Results and Discussion

Iso-structure of $[\text{Zn}(\text{bdc})(\text{ted})_{0.5}]\cdot 2\text{DMF}\cdot 0.2\text{H}_2\text{O}$ (**8**) and $[\text{Co}(\text{bdc})(\text{ted})_{0.5}]\cdot 2\text{DMF}\cdot 0.2\text{H}_2\text{O}$ (**9**) crystallize in the tetragonal crystal system, space group $P4/ncc$.^{33, 34} Removal of the guest molecules in **8** result in a three-dimensional (3D) porous structure containing interlacing channels of two different sizes (7.5×7.5 Å, 4.8×3.2 Å). The SBU is a paddle-wheel $\text{Zn}_2(\text{COO})_4(\text{ted})_2$ unit as shown in Scheme 1.



Scheme 3.1 The paddle-wheel $\text{Zn}_2(\text{COO})_4(\text{ted})_2$ SBU unit.

Each paddle-wheel SBU is linked by bdc within the layer to form a 2D net parallel to the xy plane, which is further connected by ted molecules to give rise to a 3D framework with a very large solvent accessible volume (61.3 % for **8** and 59.2 % for **9**). The structure, to a large degree, resembles what was originally proposed for a Cu-bdc-ted compound by Seki and Mori,² but the bdc ligands in the 2D nets bend

significantly, resulting in a non-symmetrical grid (with a cross-section of 9.2×5.0 Å, measured between the C atoms and calculated using van der Waals radius), as shown in Figure. 3.1.

The unique portions of the links in **8** are the $\text{Zn}_2(\frac{1}{2}\text{bdc})_4(\frac{1}{2}\text{ted})_2$ vertices along the 4-fold symmetry axis at $(\frac{1}{4}, \frac{1}{4}, z)$. Thus, the ted ligands, which have 3-fold molecular symmetry, are necessarily disordered about the 4-fold axis to yield 12 partially-occupied ethylene sites. At the center of the pore lie the $-\frac{1}{4}, \frac{1}{4}, z$ 4-fold axis and the partially occupied water molecule site, which is surrounded by a quartet of DMF molecules that

are additionally disordered about their C1-N1 bond. The disorder of sorbed DMF and water molecules is expected in the very porous structure of **8**. It is interesting that the more hydrophobic portion of the DMF molecules point away from the 1,4-bdc linkers and in toward the center of the pore, and further, that a water molecule can be accommodated in the center of the hydrophobic pore, surrounded only by methyl groups.

The structural features of the overall network were first described by Kim, *et al.* in their *I4/mcm* phase³ which are similar, but not identical to our *P4/ncc* phase of **8**. These two structures represent apparently two different phases and contain some noteworthy differences in molecular structure, as a result of significantly different site symmetries at the vertices. On going from the *I4/mcm* (Kim's phase) to *P4/ncc* (Compound **8**), the high degree of symmetry for the Zn paddlewheel; the porous region; and the overall framework, is noticeably reduced, and is shifted by ($\frac{1}{4}$ $\frac{1}{4}$ 0+ δ). In our *P4/ncc* phase of **8**, there is still a twisted $\text{Zn}_2(\text{bdc})_4$ paddlewheel group, but the "unusually bent bdc linker" of Kim's *I4/mcm* structure is replaced in our structure with a less-bent bdc ligand with twisted COO groups (torsions of 11 and 14°, compared to 2° in the *I4/mcm* phase). The more linear Zn-bdc motif found in our *P4/ncc* phase of **8** (out-of-plane distance of the C atom in COO^- is 0.07 Å, compared to 0.20 Å in the *I4/mcm* phase) matches the guest-free and benzene-containing analogs of **8** in Kim's work, and is the more expected (linear) motif for the rigid (bdc) linker. Twisting of the COO group by more than 10° is observed in several other benzyl mono- and di-carboxylates in metal paddlewheel structures.^{35, 36}

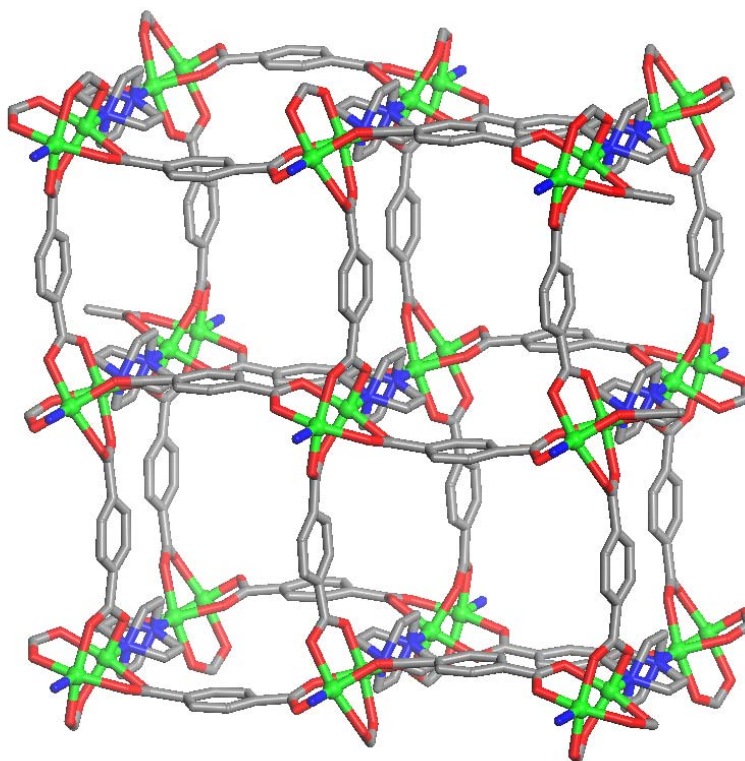


Figure 3.1 Views of the crystal structure of $[M(bdc)(ted)_{0.5}] \cdot 2DMF \cdot 0.2H_2O$ ($M = Zn, Co, Ni$ and Cu). Metal Cations (green), O (red), N (blue), and C (gray). For clarity, solvent molecules are omitted.

Perhaps the most noteworthy contrast between the *P4/ncc* and *I4/mcm* phases is that the lower point group symmetry in the *P4/ncc* phase of **8** contains a small offset in *z* ($\delta = 0.012\text{\AA}$ with respect to the *I4/mcm* phase) for the linked units at $\frac{1}{4} \frac{1}{4} z$ and $-\frac{1}{4} \frac{1}{4} z$, meaning the frameworks are not perfectly square in the *P4/ncc* phase, but slightly puckered. The importance of this feature (e.g., symmetrical vs. non-symmetrical networks) is expected to be manifested in a variation of adsorption properties, that may be rationally modified in the lab.

$[\text{Ni}(\text{bdc})(\text{ted})_{0.5}] \cdot 2\text{DMF} \cdot 0.2\text{H}_2\text{O}$ (**10**) and $[\text{Cu}(\text{bdc})(\text{ted})_{0.5}] \cdot 2\text{DMF} \cdot 0.2\text{H}_2\text{O}$ (**11**) appear to be isostructural to **8** and **9**, with the tetragonal crystal system and unit cell parameters $a = 15.155(2) \text{\AA}$, $c = 18.672(3) \text{\AA}$ for **10** and $a = 15.118(6) \text{\AA}$, $c = 19.274(5) \text{\AA}$ for **11** verified by powder X-ray diffraction refinement analysis as plotted in Figure 3.2. Upon removal of the guest molecules, the bdc ligand in four compounds becomes linear and the frameworks become porous. There are two types of channels. The first type is along the *c*-axis with a cross section $7.5 \times 7.5 \text{\AA}$ (measured between the carbon atoms in the two lateral bdc ligands, taking into consideration of VDW's radius of carbon). The second type is along the *a*- and *b*-axes with a cross section of $4.8 \times 3.2 \text{\AA}$ (measured between C-C and H-H atoms).

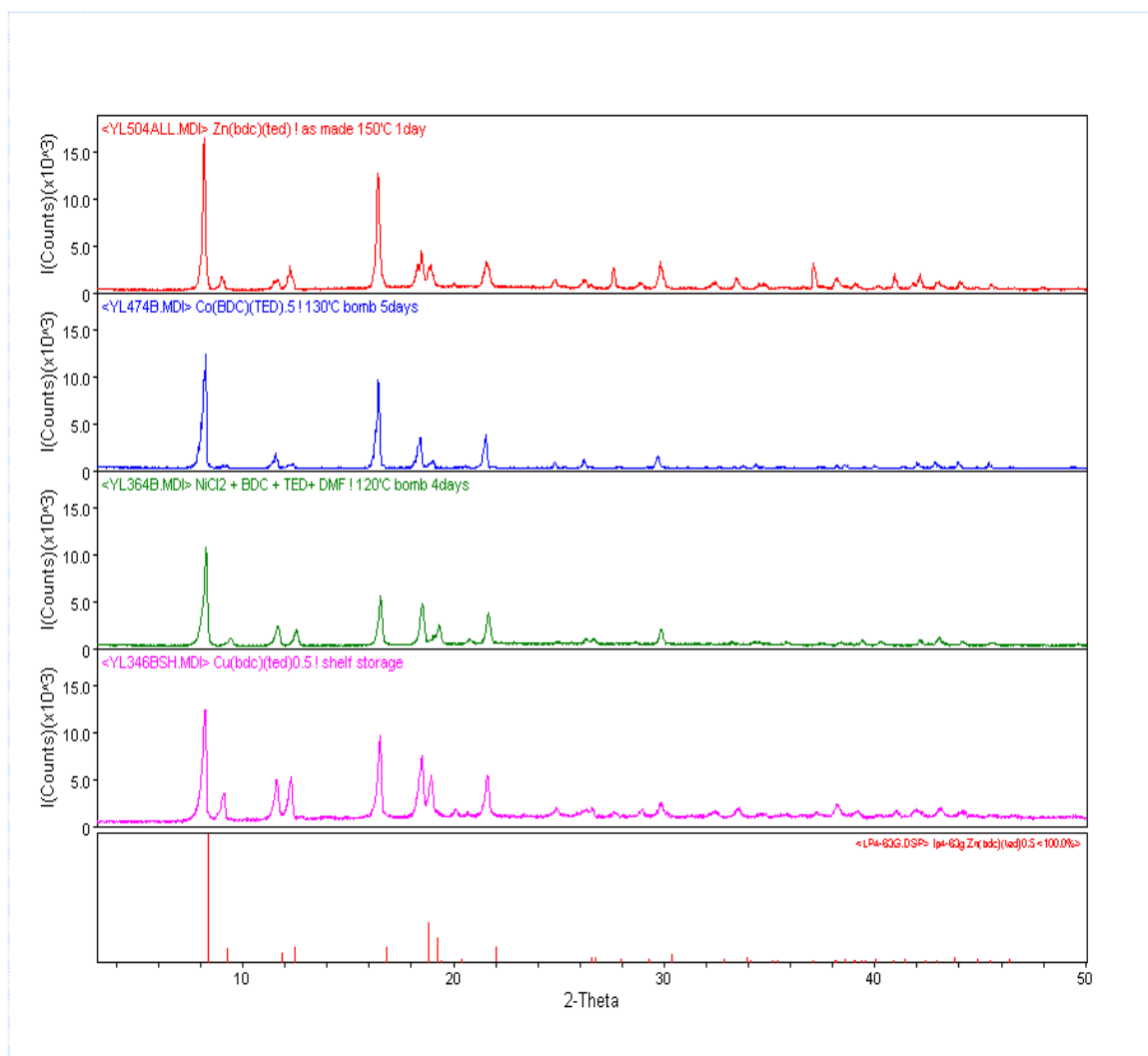


Figure 3.2 PXRD patterns of **8** ~ **11** (Zn, Co, Ni, Cu order from top to bottom) compared with the simulated pattern from the single crystal data of **8**.

As shown in Table 3.1, the thermal stability and the amount of guest molecules of all compounds were evaluated by thermogravimetric analysis (TGA). The TGA results indicated that all guest molecules can be removed around 170 °C and the resulting structures were stable to 282 °C for **8** and to 429 °C for **10**. The structural integrity of all compounds was examined by PXRD after removal of guest molecules. The permanent porosity of the guest-free crystals was confirmed by the argon adsorption data.

Table 3.1 TGA results of $[M(\text{bdc})(\text{ted})_{0.5}] \cdot 2\text{DMF} \cdot 0.2\text{H}_2\text{O}$

Crystal	M	Weight loss (%)		Decomposition Start (°C)
		Theo.	Exp.	
8	Zn	34.62	34.55	282
9	Co	35.03	32.03	320
10	Ni	35.05	34.63	429
11	Cu	34.61	33.78	280

The high resolution argon sorption isotherms were collected at 87K. The adsorption-desorption isotherms on both compounds showed a typical Type I behavior.³⁷ The calculated pore size distribution, determined by the HK method,³⁸ are shown in Figure 3.3. As shown in Table 3.2, the pore size was calculated by the HK method in the micropore range (i.e. pore size < 20 Å). These data clearly indicate that all structures have a very similar pore size distribution between 6.6 Å and 8.8 Å with a peak centered

at ca. 7.8 Å, and the results are in excellent agreement with the values calculated from the single crystal structure. The high pore volume also calculated based on DA method and the values are in the range of 0.84 ~ 0.63 cc/g. All crystals showed high surface area and they were estimated to be 1888 m²/g for **8**, 1881 m²/g for **9**, 1783 m²/g, for **10**, 1497 m²/g for **11**, respectively. As shown in Table 3.2, there were some differences in surface area and pore volume between **8**, **9** and **10**, **11**. As **8** and **9** compounds were obtained in single crystal quality and **10** and **11** compounds were obtained in polycrystalline powder, the crystal quality of **11** and **12** is lower than that of **8** and **9**.

Table 3.2 Porosity of [M(bdc)(ted)_{0.5}] based on Ar sorption isotherm at 87K.

Crystal	M	Surface Area (m ² /g)		Pore Size (Å)		V _p (cc/g) ^c
		BET	Langmuir	Max ^a	Avg. ^b	
8	Zn	1888	2174	7.9	7.8	0.84
9	Co	1881	2133	7.9	7.8	0.83
10	Ni	1783	2000	7.7	7.8	0.74
11	Cu	1497	1839	7.7	7.8	0.63

^a. H-K Pore size at maximum intensity

^b. H-K Pore size at center of the peak at half intensity

^c. D-A micro Pore Volume

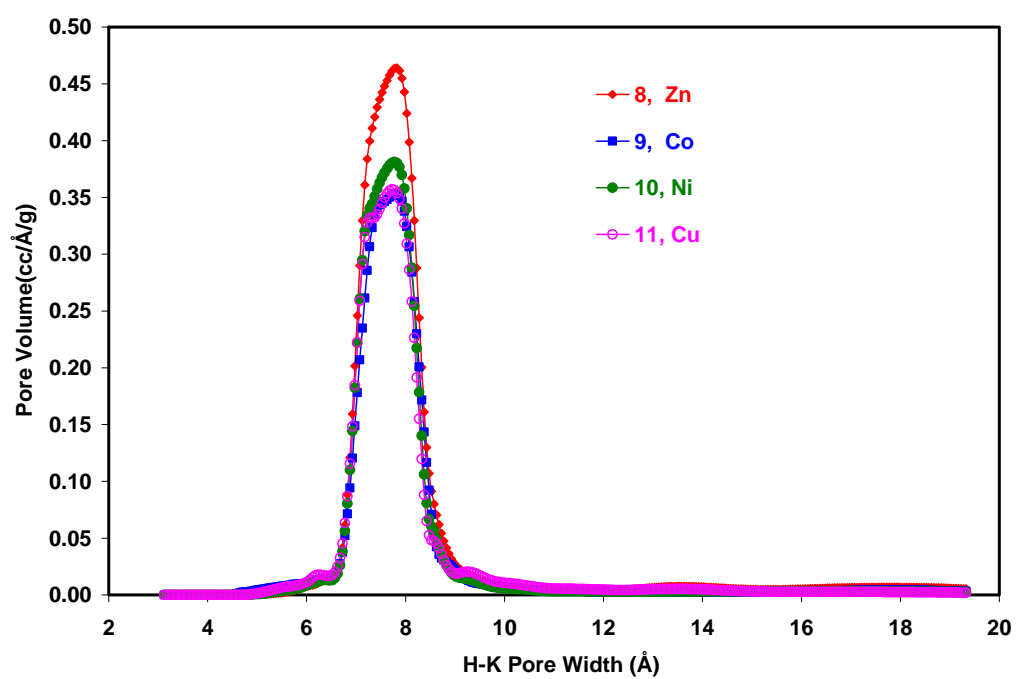


Figure 3.3 The HK Pore size distribution for **8 ~ 11** calculated from Ar sorption isotherms at 87 K.

The hydrogen adsorption-desorption isotherms were measured for all compounds at 77 K and 87 K as a function of relative pressure in the range of 10^{-4} to 1 atm. No hysteresis was observed in these isotherms throughout the entire pressure region, as shown in Figure 3.4. As presented in Table 3.3, higher H₂ uptake was observed in the Zn Co, Ni compounds at 77K and 87 K. At 87 K and 1 atm, the values are ca. 1.1~1.2 wt% and at 77 K, they are 2.1~1.8 wt%, respectively. These values are among the highest reported thus far under the same conditions.^{3, 14, 20} The value for **8** at 77K also matches well with the previously reported data.³

Table 3.3 The Q_{st} results of $[M(bdc)(ted)_{0.5}] \cdot 2DMF \cdot 0.2H_2O$

Crystal	M	H ₂ Uptake (%)		Q_{st} (kJ/mol)	
		77K	87K	Max	(0.02 ~ 0.3 wt%)
8	Zn	2.1	1.2	6.5	5.2 ~ 5.0
9	Co	2.1	1.2	7.6	5.6 ~ 5.0
10	Ni	2.1	1.2	7.8	6.0 ~ 5.0
11	Cu	1.9	1.1	7.4	6.2 ~ 5.0
1	Zn	HK Pore size ~ 6.5 Å		7.3	7.3 ~ 6.2
2	Co	HK Pore size ~ 6.9 Å		7.1	7.1 ~ 6.6
[Zn(tbip)] ³⁰		HK Pore size ~ 6.3 Å		7.4	6.9 ~ 6.6

The extent of sorbent-sorbate interactions between hydrogen and MOF was assessed by isosteric heats of hydrogen adsorption, Q_{st} . The maximum values of Q_{st} are in range between 6.5~7.8 kJ/mol. As shown in Figure. 3.4b, they are saturated around 5.0 kJ/mol at higher coverage (0.3 wt% <).

Although the Q_{st} at high coverage region ($0.3\text{wt}\% <$) are same for all compound, those values between coverage of $0.02 \sim 0.3\text{wt}\%$ showed a reverse trend with respect to their pore volume. These differences in Q_{st} value at lower coverage would be attributed to the existence of different cations in the $[\text{M}(\text{bdc})(\text{ted})_{0.5}]$ frameworks.^{16, 39}

Note that the overall values in coverage between $0.02 \sim 0.3 \text{ wt}\%$ are slightly lower than those reported for the RPM-1²⁸ and $\text{Zn}(\text{tbip})$ ^{28, 30} structures which have smaller pore and low pore volume (see Table 3.3).

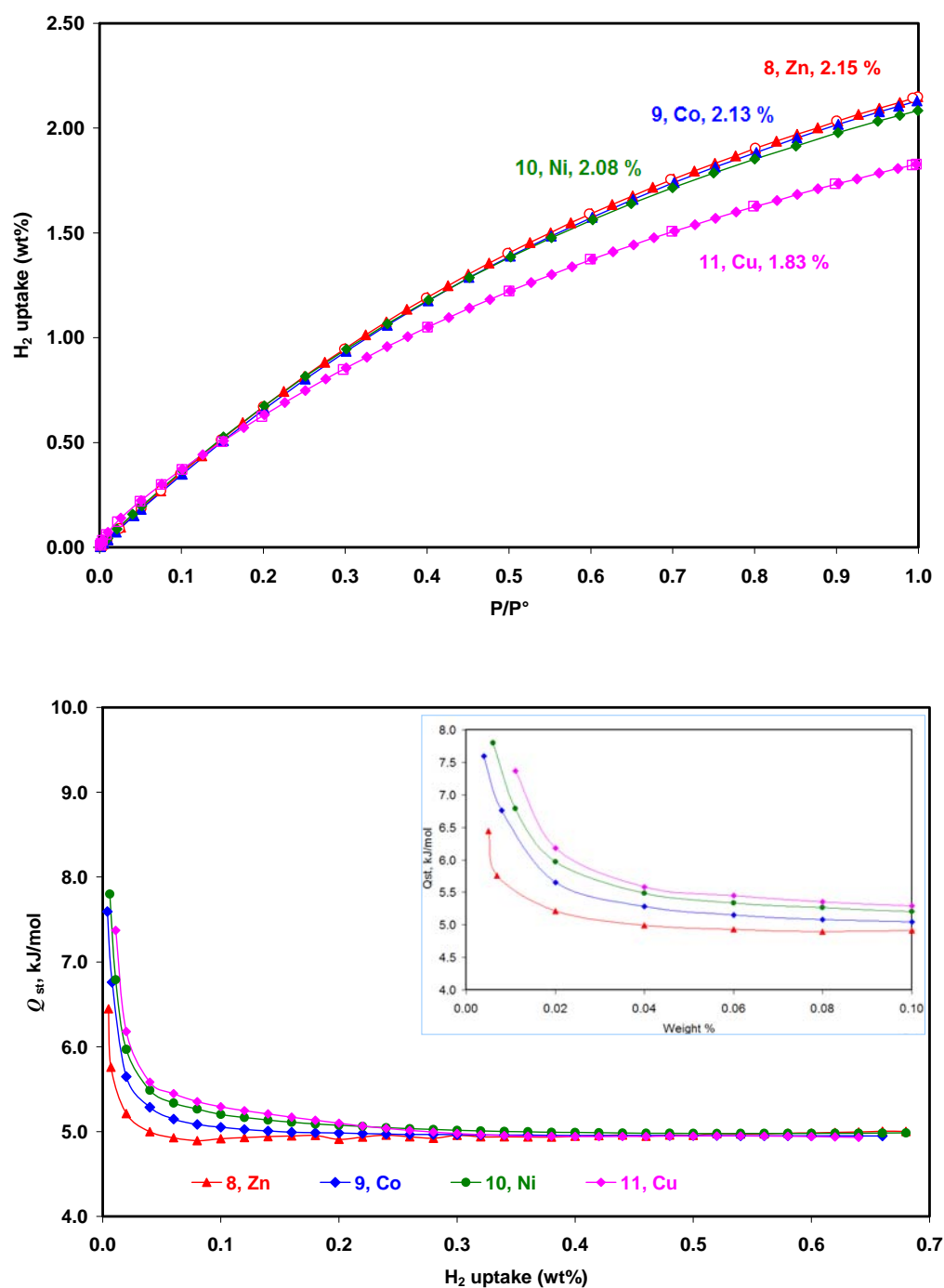


Figure 3.4 (a) Hydrogen sorption isotherms of **8-11** at 77 K (solid marks for adsorption and open marks for desorption) and (b) Isosteric heat of adsorption, Q_{st} as a function of hydrogen loading.

3.4 Conclusions

Four isostructural compounds $[M(\text{bdc})(\text{ted})_{0.5}] \cdot 2\text{DMF} \cdot 0.2\text{H}_2\text{O}$ [$M = \text{Zn}(\mathbf{8})$, $\text{Co}(\mathbf{9})$, $\text{Ni}(\mathbf{10})$, $\text{Cu}(\mathbf{11})$] have been synthesized and structurally characterized. Their pore properties were investigated via gas sorption studies at cryogenic temperatures. The pore characteristics of four compounds were analyzed based on the argon adsorption-desorption isotherms. Ar sorption studies confirm that all compounds are highly porous with a pore volume of 0.63 and 0.84 cc/g for **11** and **8**, respectively.

A hydrogen uptake of 2.1 wt% was achieved at 77 K and 1 atm for **8**, **9**, **10** and 1.8 wt% for **11**, respectively, placing them among the group of MOFs demonstrating the highest H_2 sorption capacity at the given temperature and pressure. Although overall Q_{st} values at high loading (0.3 wt% <) of hydrogen sorption are very close to each other, small differences in Q_{st} were observed at low loading region (0.02 ~ 0.3 wt% H_2 uptake) with different metal cations in the order of $\text{Cu} > \text{Ni} > \text{Co} > \text{Zn}$. Assuming similar sample and crystal quality this seems to suggest that magnitude of interaction between metal and hydrogen is slightly different in the $[M(\text{bdc})(\text{ted})_{0.5}]$ system, since all compounds have the same paddle wheel SBU.

3.5 References

1. Eddaoudi, M.; Kim, J.; Rosi, N.; Vodak, D.; Wachter, J.; O'Keeffe, M.; Yaghi, O. M., Systematic design of pore size and functionality in isoreticular MOFs and their application in methane storage. *Science* **2002**, 295, (5554), 469-72.
2. Seki, K.; Mori, W., Syntheses and Characterization of Microporous Coordination Polymers with Open Frameworks. *J. Phys. Chem. B* **2002**, 106, (6), 1380-1385.
3. Dybtsev, D. N.; Chun, H.; Kim, K., Rigid and flexible: a highly porous metal-organic framework with unusual guest-dependent dynamic behavior. *Angew. Chem. Int. Ed.* **2004**, 43, (38), 5033-5036.
4. Pan, L.; Adams, K. M.; Hernandez, H. E.; Wang, X.; Zheng, C.; Hattori, Y.; Kaneko, K., Porous Lanthanide-Organic Frameworks: Synthesis, Characterization, and Unprecedented Gas Adsorption Properties. *J. Am. Chem. Soc.* **2003**, 125, (10), 3062-3067.
5. Matsuda, R.; Kitaura, R.; Kitagawa, S.; Kubota, Y.; Belosludov, R. V.; Kobayashi, T. C.; Sakamoto, H.; Chiba, T.; Takata, M.; Kawazoe, Y.; Mita, Y., Highly controlled acetylene accommodation in a metal-organic microporous material. *Nature* **2005**, 436, (7048), 238-241.
6. Rosi, N. L.; Eckert, J.; Eddaoudi, M.; Vodak, D. T.; Kim, J.; O'Keeffe, M.; Yaghi, O. M., Hydrogen storage in microporous metal-organic frameworks. *Science* **2003**, 300, (5622), 1127-1129.
7. Rowsell, J. L. C.; Millward, A. R.; Park, K. S.; Yaghi, O. M., Hydrogen Sorption in Functionalized Metal-Organic Frameworks. *J. Am. Chem. Soc.* **2004**, 126, (18), 5666-5667.
8. Dinca, M.; Long, J. R., Strong H₂ Binding and Selective Gas Adsorption within the Microporous Coordination Solid Mg₃(O₂C-C₁₀H₆-CO₂)₃. *J. Am. Chem. Soc.* **2005**, 127, (26), 9376-9377.
9. Kesanli, B.; Cui, Y.; Smith, M. R.; Bittner, E. W.; Bockrath, B. C.; Lin, W., Highly Interpenetrated Metal-Organic Frameworks for Hydrogen Storage. *Angew. Chem. Int. Ed.* **2005**, 44, (1), 72-75.
10. Rowsell, J. L. C.; Yaghi, O. M., Strategies for Hydrogen Storage in Metal-Organic Frameworks. *Angew. Chem. Int. Ed.* **2005**, 44, (30), 4670-4679.
11. Zhao, X.; Xiao, B.; Fletcher, A. J.; Thomas, K. M.; Bradshaw, D.; Rosseinsky, M. J., Hysteretic Adsorption and Desorption of Hydrogen by Nanoporous Metal-Organic Frameworks. *Science* **2004**, 306, (5698), 1012-1015.

12. Lee, E. Y.; Jang, S. Y.; Suh, M. P., Multifunctionality and crystal dynamics of a highly stable, porous metal-organic framework [Zn₄O(NTB)₂]. *J. Am. Chem. Soc.* **2005**, 127, (17), 6374-6381.
13. Kubota, Y.; Takata, M.; Matsuda, R.; Kitaura, R.; Kitagawa, S.; Kato, K.; Sakata, M.; Kobayashi, T. C., Direct Observation of Hydrogen Molecules Adsorbed onto a Microporous Coordination Polymer. *Angew. Chem. Int. Ed.* **2005**, 44, (6), 920-923.
14. Chun, H.; Dybtsev, D. N.; Kim, H.; Kim, K., Synthesis, X-ray Crystal Structures, and Gas Sorption Properties of Pillared Square Grid Nets Based on Paddle-Wheel Motifs: Implications for Hydrogen Storage in Porous Materials. *Chemistry - A European Journal* **2005**, 11, (12), 3521-3529.
15. Dybtsev, D. N.; Chun, H.; Yoon, S. H.; Kim, D.; Kim, K., Microporous manganese formate: a simple metal-organic porous material with high framework stability and highly selective gas sorption properties. *J. Am. Chem. Soc.* **2004**, 126, (1), 32-33.
16. Kaye, S. S.; Long, J. R., Hydrogen Storage in the Dehydrated Prussian Blue Analogues M₃[Co(CN)₆]₂ (M = Mn, Fe, Co, Ni, Cu, Zn). *J. Am. Chem. Soc.* **2005**, 127, (18), 6506-6507.
17. Férey, G.; Latroche, M.; Serre, C.; Millange, F.; Loiseau, T.; Percheron-Guégan, A., Hydrogen adsorption in the nanoporous metal-benzenedicarboxylate M(OH)(O₂C-C₆H₄-CO₂)(M = Al³⁺, Cr³⁺), MIL-53. *Chem. Comm.* **2003**, 24, 2976 - 2977.
18. Dubinin, M. M.; Astakhov, V. A., D-A method. *Adv.Chem.Series* **1970**, 102, 69.
19. Li, Y.; Yang, R. T., Significantly Enhanced Hydrogen Storage in Metal-Organic Frameworks via Spillover. *J. Am. Chem. Soc.* **2006**, 128, (3), 726-727.
20. Wong-Foy, A. G.; Matzger, A. J.; Yaghi, O. M., Exceptional H₂ Saturation Uptake in Microporous Metal-Organic Frameworks. *J. Am. Chem. Soc.* **2006**, 128, (11), 3494-3495.
21. Eddaoudi, M.; Kim, J.; Wachter, J. B.; Chae, H. K.; O'Keeffe, M.; Yaghi, O. M., Porous metal-organic polyhedra: 25 Å cuboctahedron constructed from 12 Cu₂(CO₂)₄ paddle-wheel building blocks. *J. Am. Chem. Soc.* **2001**, 123, (18), 4368-4369.
22. Ni, Z.; Yassar, A.; Antoun, T.; Yaghi, O. M., Porous metal-organic truncated octahedron constructed from paddle-wheel squares and terthiophene links. *J. Am. Chem. Soc.* **2005**, 127, (37), 12752-12753.
23. Li, H.; Eddaoudi, M.; O'Keeffe, M.; Yaghi, O. M., Design and synthesis of an exceptionally stable and highly porous metal-organic framework *Nature* **1999**, 402, 276-279.

24. Pan, L.; Liu, H.; Lei, X.; Huang, X.; Olson, D. H.; Turro, N. J.; Li, J., RPM-1: a recyclable nanoporous material suitable for ship-in-bottle synthesis and large hydrocarbon sorption. *Angew. Chem. Int. Ed.* **2003**, 42, (5), 542-546.
25. Pan, L.; Liu, H.; Kelly, S. P.; Huang, X.; Olson, D. H.; Li, J., RPM-2: a recyclable porous material with unusual adsorption capability: self assembly via structural transformations. *Chem Commun (Camb)* **2003**, (7), 854-855.
26. Pan, L.; Sander, M. B.; Huang, X.; Li, J.; Smith, M.; Bittner, E.; Bockrath, B.; Johnson, J. K., Microporous metal organic materials: promising candidates as sorbents for hydrogen storage. *J. Am. Chem. Soc.* **2004**, 126, (5), 1308-1309.
27. Lee, J.; Li, J.; Jagiello, J., Gas sorption properties of microporous metal organic frameworks. *Journal of Solid State Chemistry* **2005**, 178, (8), 2527-2532.
28. Lee, J. Y.; Pan, L.; Kelly, S. P.; Jagiello, J.; Emge, T. J.; Li, J., Achieving High Density of Adsorbed Hydrogen in Microporous Metal Organic Frameworks. *Advanced Materials* **2005**, 17, (22), 2703-2706.
29. Pan, L.; Olson, D. H.; Ciemmolonski, L. R.; Heddy, R.; Li, J., Separation of Hydrocarbons with a Microporous Metal-Organic Framework. *Angew. Chem. Int. Ed.* **2006**, 45, (4), 616-619.
30. Pan, L.; Parker, B.; Huang, X.; Olson, D. H.; Lee, J. Y.; Li, J., Zn(tbip) (H₂tbip= 5-tert-Butyl Isophthalic Acid): A Highly Stable Guest-Free Microporous Metal Organic Framework with Unique Gas Separation Capability. *J. Am. Chem. Soc.* **2006**, 128, (13), 4180-4181.
31. Bruker(2003), **SAINT+ (Version 6.45)**, , SMART (Version 5.629) and SHELXTL (Version 6.14). Bruker AXS Inc.,Madison, Wisconsin,, USA.
32. Site, disorder includes equivalent 4-fold positions for the ted ligand [with both N atoms on the same ($\frac{1}{4}$, $\frac{1}{4}$, z) axis as the Zn atoms] and non-equivalent 2-fold positions (85:15) for the DMF site (near 1, 0, $\frac{1}{2}$); water is only present at about the 10% level (at $-\frac{1}{4}$, $\frac{1}{4}$, $\frac{1}{4}$); non-hydrogen atoms were refined with anisotropic displacement parameters except for the disordered C atoms of the ted [a single Uiso value for all 6 C atoms with 0.25 site occupancy refined to 0.015(1)], the minor (15%) component of the DMF, and the water O atom; all H atoms at calculated positions; largest residuals after refinement were less than 0.5 e/Å³.
33. Crystal Data for [Zn(bdc)(ted)_{0.5}]•2DMF•0.2H₂O. : Mw = 432.69, Tetragonal, P4/ncc (no. 130), *a* = 14.8999(3), *c* = 19.1369(2)Å, *V* = 4248.4(2) Å³, *Z* = 8, *T* = 100 K, Density(calculated) = 1.353 Mg/m³, MoKα radiation, μ = 11.91 cm⁻¹, Colorless block, Crystal size = 0.13 x 0.11 x 0.03 mm³, Total number of reflections 24 335 [3119 unique *R*(int) = 0.055], *R*1=0.044 [2113 data with *I* > 2σ(*I*)], *wR*2= 0.1368 [all data], GOF = 1.008 [all data]. CCDC 240928 contains the supplementary crystallographic data for this

paper. These data can be obtained free of charge via www.ccdc.cam.ac.uk/conts/retrieving.html (or from the Cambridge Crystallographic Data Centre, 12, Union Road, Cambridge CB21EZ, UK; fax: (+44) 1223-336-033; or deposit@ccdc.cam.ac.uk).

34. Crystal Data for $[\text{Co}(\text{bdc})(\text{ted})_{0.5}] \cdot 2\text{DMF} \cdot 0.2\text{H}_2\text{O}$. : Mw = 855.15, Tetragonal, P4/ncc (no. 130), $a = 15.0500(6)$, $c = 18.9029(10)\text{\AA}$, $V = 4281.6(3)\text{\AA}^3$, $Z = 4$, $T = 293\text{ K}$, Density(calculated) = 1.327 Mg/m^3 , MoKa radiation, $\mu = 11.91\text{ cm}^{-1}$, Dark blue block, Crystal size = $0.11 \times 0.21 \times 0.05\text{ mm}^3$, Total number of reflections 35442 [1974 unique $R(\text{int}) = 0.059$], $R1 = 0.055$ [1235 data with $I > 2\sigma(I)$], $wR2 = 0.1943$ [all data], $\text{GOF} = 1.297$ [all data].

35. Bourne, S. A.; Lu, J.; Mondal, A.; Moulton, B.; Zaworotko, M. J., Self-Assembly of Nanometer-Scale Secondary Building Units into an Undulating Two-Dimensional Network with Two Types of Hydrophobic Cavity. *Angew. Chem. Int. Ed.* **2001**, 40, (11), 2111-2113.

36. Kitaura, R.; Iwahori, F.; Matsuda, R.; Kitagawa, S.; Kubota, Y.; Takata, M.; Kobayashi, T. C., Rational Design and Crystal Structure Determination of a 3-D Metal-Organic Jungle-Gym-like Open Framework. *Inorg. Chem.* **2004**, 43, (21), 6522-6524.

37. Sing, K. S. W.; Everett, D. H.; Haul, R. A. W.; Moscou, M.; Pierotti, R. A.; Rouquerol, J.; Siemieniewska, T., Reporting Physisorption Data for Gas/Solid Systems with special Reference to the Determination of Surface Area and Porosity. *Pure Appl. Chem* **1985**, 57, (4), 603-619.

38. Horvath, G.; Kawazoe, K., Method for Calculation of Effective Pore Size Distribution in Molecular Sieve Carbon. *J. Chem. Eng. Jpn.* **1983**, 16, (6), 470-475.

39. Dinca, M.; Long, J. R., High-Enthalpy Hydrogen Adsorption in Cation-Exchanged Variants of the Microporous Metal-Organic Framework $\text{Mn}_3[(\text{Mn}_4\text{Cl})_3(\text{BTT})_8(\text{CH}_3\text{OH})_{10}]_2$. *J. Am. Chem. Soc.* **2007**, 129, (36), 11172-11176.

CHAPTER FOUR

EXCEPTIONAL HIGH HYDROGEN UPTAKE ON MICROPOROUS METAL-ORGANIC FRAMEWORKS AND THEIR METHANE STORAGE CAPACITY

4.1. Introduction

Two of current hydrogen storage technologies are achieved by either liquefaction of H₂ gas at very low temperature (-253°C) or compression of hydrogen gas at extremely high pressure (~350 atm or higher).¹⁻³ As described earlier in this thesis, the DOE has set technical targets for on-board hydrogen storage system to have 6 wt% of gravimetric storage capacity and 45 g/L of volumetric uptake by Year 2010. Notably, the target of maximum delivery pressure from storage tank has been set around 100 atmosphere (see Table 1.1). However, hydrogen storage capacity on microporous MOFs has been primarily investigated at low pressure range as described in Table 1.2 in Chapter One. Very little data have been reported on hydrogen adsorption at higher pressure, and thus, the research in this area is still at the very early stage. Recently, Wong-Foy *et al.* reported 7.5 wt% of hydrogen uptake at 77 K and ~70 bar and Dinca *et al.* claimed 60 g/L of volumetric hydrogen uptake at 77 K, 90 bar, placing them the highest uptake values to this date.^{4,5} As high pressure gas adsorption analyzer is now available in our research group, extensive studies are being conducted on the selected MOF materials.

This instrument was developed by VTI cooperation mainly for characterization of mesoporous materials. As our materials are microporous and have different properties, detail measurement conditions will be presented as well as hydrogen sorption data. This study shows the correlation of hydrogen storage with surface area and pore volume at high pressure and the high volumetric uptake up to 36 g/L and high gravimetric uptake up to 5.48 wt% at 77 K. This study also presents the first experimental assessments of the cycle life of hydrogen on MMOF materials under high pressure condition. In addition, a promising separation property of methane and hydrogen will also be discussed.

4.2 Experimental

4.2.1 Sample Preparations

Preparation of $[\text{Zn}_3(\text{bpdc})_3\text{bpy}]\cdot 4\text{DMF}\cdot \text{H}_2\text{O}$ (1) A gram scale of single crystals of **1** were grown by solvothermal reaction. A mixture of zinc (II) nitrate hexahydrate (1.020 g, 3.43 mmol), H_2bpdc (0.960 g, 3.96 mmol), bpy (0.639 g, 4.09 mmol) were dissolved in 90 mL of DMF in 250mL beaker. The solution was sonicated in warm tap water bath until solution became clear then the solution transferred into Teflon-lined autoclaves and heated in an oven at 150°C for overnight. Single crystals of **1** (1.398 g, 88% yield) were isolated after filtering and washing the product by DMF (10 mL \times 3).

Preparation of $[\text{Co}_3(\text{bpdc})_3\text{bpy}]\cdot 4\text{DMF}\cdot \text{H}_2\text{O}$ (2) The large scale samples were prepared by using the same molar ratio of single crystal growth reaction. A mixture of cobalt (II) nitrate hexahydrate (0.720 g, 2.47 mmol), H_2bpdc (0.900 g, 3.72 mmol), bpy (0.576 g, 3.69 mmol) were dissolved in 120 mL of DMF in 250mL beaker. The solution was treated by ultrasonic in warm tap water bath until solution became clear then the solution transferred into Teflon-lined autoclaves and heated in an oven at 150°C for 72 hours. Single crystals of **2** (0.896 g, 80% yield) were isolated after filtering and washing the product with 10 mL of fresh DMF three times.

Preparation of $[\text{Cu}(\text{hfipbb})(\text{H}_2\text{hfipbb})_{0.5}]$ (3) A gram scale single crystal samples of **3** were synthesized from hydrothermal reaction of $\text{Cu}(\text{NO}_3)_2\cdot 3\text{H}_2\text{O}$ (0.288 g, 1.2 mmol) with excess H_2hfipbb (1.464, 3.7 mmol) in 60 mL of deionized water at 160°C for 3 days. Excess H_2hfipbb was removed by repeatedly washing of the product with 10 mL of fresh

DMF five times. Single crystals of **3** (0.673 g, 86% yield) were isolated after filtering followed by drying the product in the oven at 50°C under vacuum for five minute.

Preparation of $[\text{Cu}_3(\text{BTC})_2(\text{H}_2\text{O})_3] \cdot n\text{H}_2\text{O}$ (5) A gram scale single crystal samples of **5** were synthesized from a reaction of $\text{Cu}(\text{NO}_3)_2 \cdot 3\text{H}_2\text{O}$ (2.610 g, 10.8 mmol) dissolved in 30 mL of de-ionized water and BTC (0.666 g, 3.12 mmol) dissolved in 30 mL of ethanol. Two solutions were mixed in the 250 mL beaker then 2 mL of DMF was added. After 5 minutes sonication treatment, the solution mixture was transferred into a Teflon-lined autoclave and heated in an oven at 80°C for 19 hours. The products were isolated after filtering and washing with 10 mL of ethanol three times and dried under vacuum at 50°C. The aqua blue crystals were immersed in DCM (Dichloromethane) solution for 4 days to exchange guest molecules. After first 24 hour, the upper clear solution was decant and fresh 50 mL of DCM solution in every 24 hours for next three days. After drying under vacuum at 50°C for five minute, the product was collected (1.328 g, 41% yield overall reaction) and activated at 170°C for overnight.

Preparation of $[\text{Zn}(\text{bdc})(\text{ted})_{0.5}] \cdot 2\text{DMF} \cdot 0.2\text{H}_2\text{O}$ (8) A mixture of zinc (II) nitrate tetrahydrate (1.464 g, 5.6 mmol), H_2bdc (0.960 g, 5.8 mmol), ted (0.432 g, 3.9 mmol) and 120 mL DMF was mixed in a 250 mL beaker. After mixing of all chemicals the solution became cloudy suspension and nitric acid was added approximate ratio of *ca.* one drop of nitric acid per 10 mL of DMF solution. An ultrasonic treatment was given to dissolve all solid chemicals until obtaining a clear solution in warm tap water bath. Then the solution was transferred into digestion bombs and heated at 150°C for overnight. Colorless single

crystals of $[\text{Zn}(\text{bdc})(\text{ted})_{0.5}] \cdot 2\text{DMF} \cdot 0.2\text{H}_2\text{O}$ (**8**) (2.152 g, 89% yield) were isolated after filtering and washing with 10 mL of DMF three times and drying under vacuum at 50°C.

Preparation of $[\text{Co}(\text{bdc})(\text{ted})_{0.5}] \cdot 2\text{DMF} \cdot 0.2\text{H}_2\text{O}$ (9**)** Gram scale of **9** was synthesized at the slightly higher temperature and longer time of reaction condition. A mixture of cobalt (II) chloride hexahydrate (2.160 g, 9.1 mmol), H_2bdc (1.200 g, 7.2 mmol), ted (0.540 g, 4.8 mmol) and 100 mL DMF was mixed in a 250 mL beaker. After mixing of all chemicals, the solution became cloudy suspension and then nitric acid was added approximate ratio of *ca.* one drop of nitric acid per 10 mL of DMF solution. A sonic treatment was given to dissolve all solid chemicals until obtaining a clear solution in warm tap water bath. Then the solution was transferred into digestion bombs and heated at 130°C for 6 days. Dark green crystals of $[\text{Co}(\text{bdc})(\text{ted})_{0.5}] \cdot 2\text{DMF} \cdot 0.2\text{H}_2\text{O}$ (**8**) were isolated (1.948 g, 50.2% yield) after filtering and washing with 10 mL of DMF three times and drying under vacuum at 50°C.

Preparation of $[\text{Ni}(\text{ndc})(\text{ted})_{0.5}] \cdot 3\text{DMF} \cdot \text{H}_2\text{O}$ (12**)** Light green crystals of **12** were grown by solvothermal reactions. A mixture of nickel (II) nitrate hexahydrate (0.870 g, 3.0 mmol), 2,6- H_2ndc (0.588 g, 2.7 mmol), ted (0.672 g, 6.0 mmol) and 60 mL of DMF was mixed in a 250 mL beaker. After mixing of all chemicals, the solution became cloudy suspension. An ultrasonic treatment was given to dissolve all solid chemicals until obtaining a clear solution in green color. Then the solution was transferred into Teflon-lined autoclaves and heated in an oven at 135°C for 3 days. Single crystals of **12**

(1.277 g, 75% yield) were isolated after filtering and washing the product three times with 10 mL of fresh DMF.

Structure Characterization of $[\text{Ni}(\text{ndc})(\text{ted})_{0.5}] \cdot 3\text{DMF} \cdot \text{H}_2\text{O}$ (12**)** The crystals of **12** were examined under microscope with polarized light, confirmed that they were single crystals as shown in Figure 4.1.

However the green crystals of **12** did not diffract well for CCD single crystal X-ray diffraction study. Therefore, the formula was proposed based on elemental analysis (EA) and TGA and powder X-ray diffraction study. The calculated compositions of **12** are: C (50.94%), H (6.19) and N (9.90%), in well agreement with elemental analysis (EA) data: C (50.94%), H (6.12) and N (9.74%). Therefore the pores contain three DMF and one water as guest molecules.

The powder diffraction pattern of compound **12** was collected on a Rigaku D/M-2200T automated diffraction system (Ultima+) using Cu $K\alpha$ radiation. Measurements were made in a 2θ range of 3-50° at room temperature. As the framework connectivity is very close to crystal **8**, the tetragonal primitive symmetry was applied to refine the unit cell of **12**. The PXRD refinement generated the following unit cell parameters for **12**, $a = 18.60 \text{ \AA}$, $c = 18.92 \text{ \AA}$, and $\alpha = \beta = \gamma = 90^\circ$ and 21 peaks out of 22 experimental peaks were matched. (Figure 4.2) The unit cell volume was calculated to be 6545.6 \AA^3 and it is about 1.5 times larger than that of the crystal **8**.

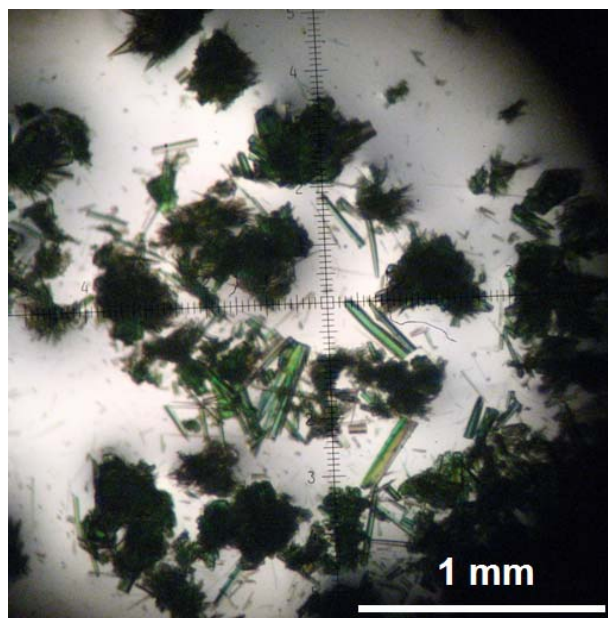


Figure 4.1 The photograph of green crystal of $[\text{Ni}(\text{ndc})(\text{ted})_{0.5}] \cdot 3\text{DMF} \cdot \text{H}_2\text{O}$ was taken under microscope with polarized light.

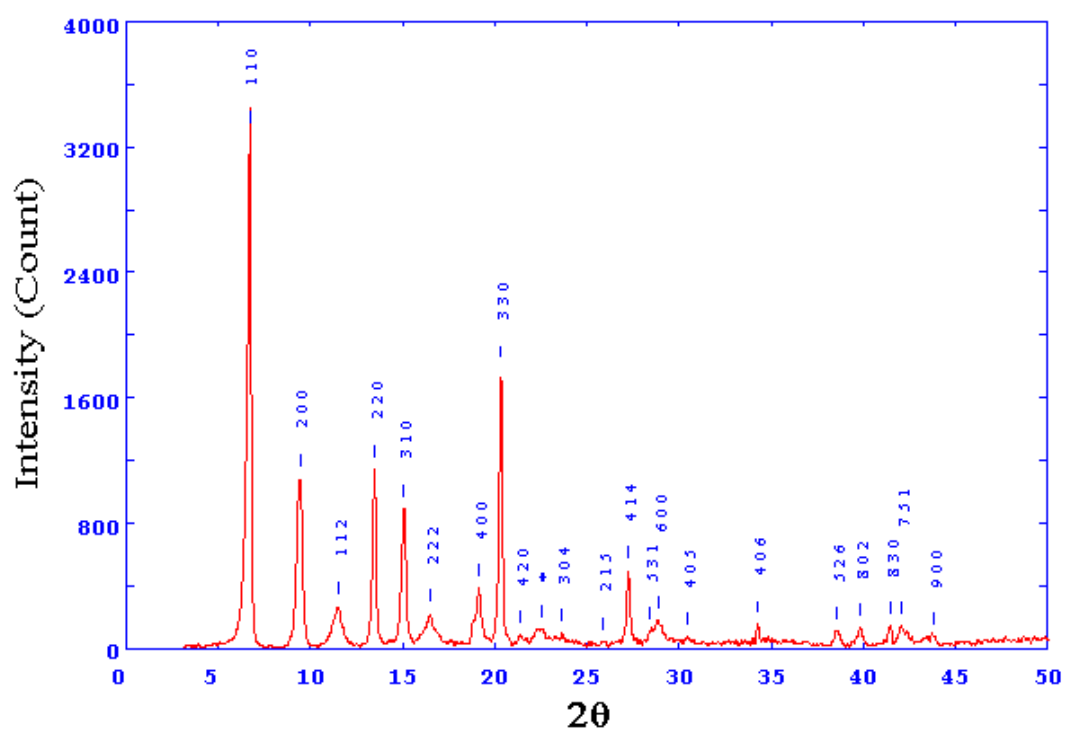
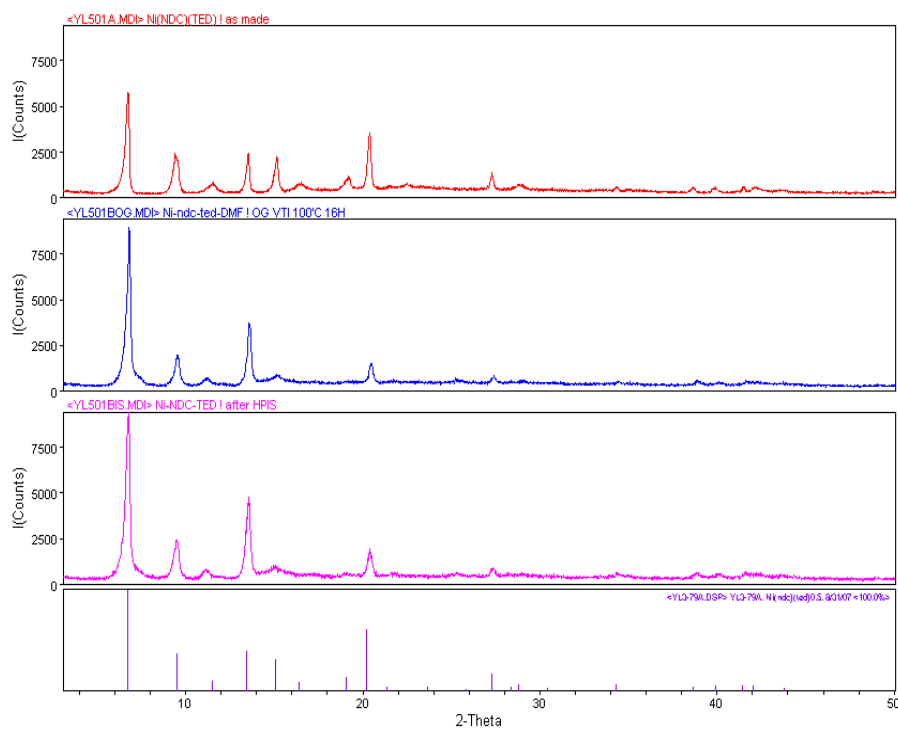


Figure 4.2 The simulated powder X-ray diffraction pattern of $[\text{Ni}(\text{ndc})(\text{ted})_{0.5}]\cdot 3\text{DMF}\cdot \text{H}_2\text{O}$ (**12**) in a 2θ range of $3 \sim 50^\circ$.

Table 4.1 Simulated peak position data of **12** by PXRD refinement.

H	K	L	2Theta (Exp.)	2Theta (Calc.)	2Theta (Diff.)	d (Exp.)	d (Calc.)	Intensity (Exp.)
1	1	0	6.69500	6.71500	-0.02000	13.19151	13.15218	3274.29
2	0	0	9.42700	9.50200	-0.07500	9.37363	9.30000	1089.12
1	1	2	11.49000	11.51300	-0.02300	7.69512	7.67976	266.40
2	2	0	13.47500	13.45400	0.02200	6.56562	6.57609	1148.50
3	1	0	15.08200	15.05000	0.03200	5.86949	5.88183	893.82
2	2	2	16.48800	16.40300	0.08400	5.37216	5.39962	220.66
4	0	0	19.15400	19.07100	0.08400	4.62987	4.65000	385.47
3	3	0	20.33100	20.23900	0.09200	4.36445	4.38406	1779.80
4	2	0	21.38000	21.34700	0.03300	4.15265	4.15909	88.87
3	0	4	23.66200	23.64000	0.02200	3.75716	3.76058	99.00
2	1	5	25.89300	25.84600	0.04700	3.43824	3.44436	47.64
4	1	4	27.25400	27.29700	-0.04200	3.26947	3.26450	496.31
5	3	1	28.44000	28.35100	0.09000	3.13578	3.14548	110.92
6	0	0	28.87300	28.77600	0.09700	3.08977	3.10000	179.65
4	0	5	30.45700	30.43100	0.02600	2.93258	2.93500	71.55
4	0	6	34.28100	34.33300	-0.05300	2.61372	2.60983	151.34
5	2	6	38.58200	38.63200	-0.04900	2.33164	2.32878	109.80
8	0	2	39.84500	39.89600	-0.05200	2.26062	2.25781	132.40
8	3	0	41.45000	41.44500	0.00500	2.17672	2.17696	145.86
7	5	1	42.03600	42.02500	0.01100	2.14770	2.14822	141.67
9	0	0	43.79600	43.76800	0.02800	2.06539	2.06667	75.86



Rutgers University - Camden

cvs Friday, Aug 31, 2007 10:09:32a

Figure 4.3 The PXRD pattern of $[\text{Ni}(\text{ndc})(\text{ted})_{0.5}] \cdot 3\text{DMF} \cdot \text{H}_2\text{O}$ depends on experimental stages; as made (red), after outgassing (blue) and after high pressure isotherms (pink) comparing with simulated peak (purple sticks were generated based on the data from Table 4.1)

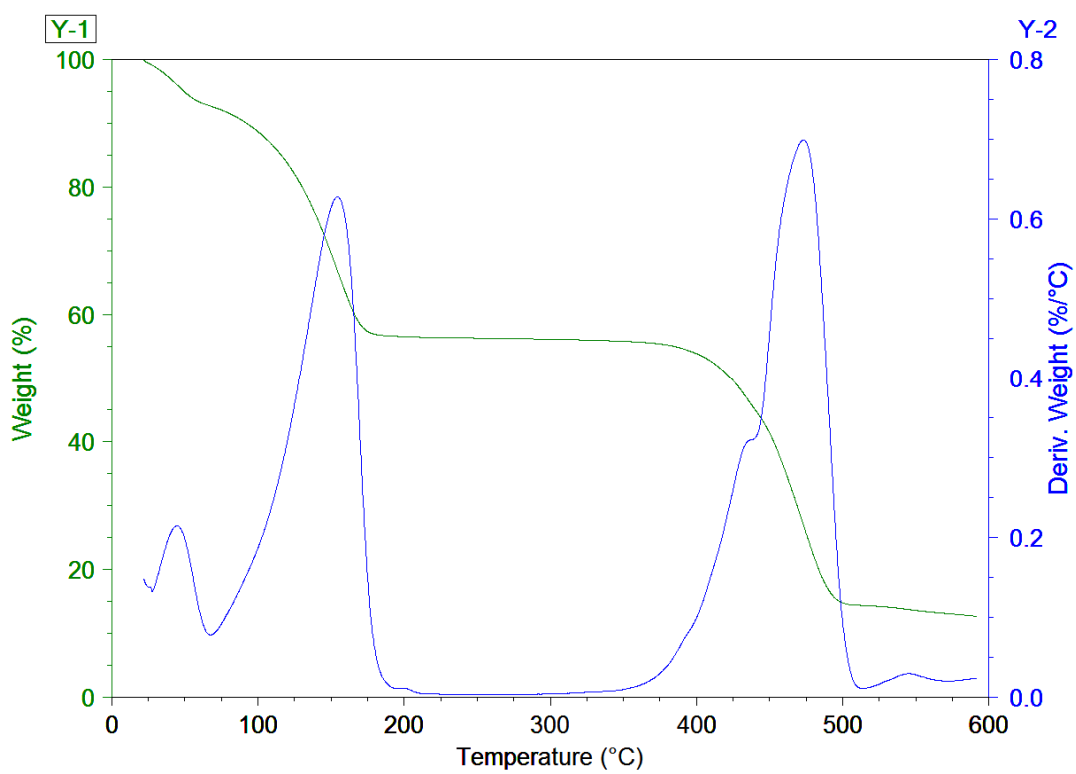


Figure 4.4 The TG and derivative curve of $[\text{Ni}(\text{ndc})(\text{ted})_{0.5}] \cdot 3\text{DMF} \cdot \text{H}_2\text{O}$ (**12**)

Preparation of [Zn(tbip)] (13) Hydrothermal reaction of $\text{Zn}(\text{NO}_3)_2 \cdot 4\text{H}_2\text{O}$ (0.692 g, 2.65 mmol), H_2tbip (0.584 g, 2.62 mmol) with mixture solution of 48 mL H_2O and 8 mL ethylene glycol at 180°C for 3 days generated uniform brown column crystals of **13** (0.552 g, 73% yield) after filtering and washing by distilled water (3×30 mL), followed by ethanol (3×30 mL) and drying under vacuum at 50°C . IR (cm^{-1}): 3448(br), 2994 (vs), 2974(s), 1621(vs), 1544(vs), 1433(s), 1417(s), 1376(vs), 1307(s), 1514(s), 1258(m), 1188(s), 1111(s), 935(s), 910(m), 804(m), 771(vs), 743(m), 714(vs), 694(s), 641(m), 575(s), 534(m), 506(s). PXRD of the bulk samples was in excellent agreement with the simulated PXRD pattern.

4.2.2 Sorption Study and Experimental Conditions

Ar adsorption at 87 K

The low temperature high-resolution gas adsorption-desorption measurements were performed using an automated micropore gas analyzer, Autosorb-1 MP (Quantachrome Instruments) based on the procedure described in the chapter two. The same samples used for argon sorption studies were used for low pressure hydrogen sorption studies and hydrogen sorption isotherms were collected in a relative pressure range from 10^{-4} to 1 atm at 77 K and 87 K. A total analysis time was ca. 9~10 hours for hydrogen sorption. The results of low pressure argon and hydrogen sorption were summarized on the Table 4.2

Table 4.2 Summary of the pore properties of argon and hydrogen sorption at low pressure and cryogenic temperatures.

<i>materials</i>	V_{acc} (%)	d_{og} (g/cm ³)	<i>H-K Pore</i> <i>Size (Å)</i>	<i>H-K V_p</i> (cc/g)	<i>Surface Area (m²/g)</i>		<i>H₂ (wt%)</i> <i>77K</i>	d_{H_2} (g/L)	Q_{st} (kJ/mol)
					<i>BET</i>	<i>LANG.</i>			
1	40.7	1.090	6.7	0.29	793	971	1.4	12.8	7.3
2	40.6	1.158	6.9	0.33	779	1129	1.5	13.0	7.1
3	11.6	1.619	5.8	0.01	20	53	0.2	3.7	4.2
5	69.5	0.879	6.0/7.9	0.36	1014	1227	1.4	16.0	7.3
8	56.7	0.893	7.8	0.69	1888	2177	2.1	24.1	7.1
9	59.2	0.830	7.8	0.67	1881	1983	2.1	27.6	7.6
12	(71.0) ^a	-	9.3	0.82	2307	2453	1.7	-	7.7
13	17.7	1.483	6.3	0.11	278	400	0.8	5.4	7.4

^a. estimated from the average ratio of pore size, V_p and SA between **9** and **12** (71.0=59.2 ×1.2)

Hydrogen adsorption under high pressure

The high pressure hydrogen isotherm experiments were conducted using high pressure gas analyzer, HPVA-100, from the VTI corporation and NIST gas behavior model was used for data analysis with automated software HPA (VERSION 11). The pressures of manifold and the sample cell were monitored by two electronic Bourdon gauge-type transducers (Mensor), separately. The transducers could read the pressure to 1500 psi with 0.010 % of accuracy. The high vacuum ($\sim 10^{-6}$ mbar) was controlled by turbomolecular pump from Pfeiffer in both units. Ultra high purity He (UHP 5.0) was used to determine dead space of the sample cell and ultra high purity H₂ (UHP 5.0) was used for analysis, respectively. The outgassing procedure was same as low pressure experiment, but 300 - 800 mg of activated samples were used for high pressure analysis. The cryogenic temperatures were controlled using liquid argon for 87 K and liquid nitrogen for 77 K as baths, respectively. The constant room temperature was controlled by computer controlled water bath from Polyscience Co.

Experimental Conditions for High Pressure Measurement

A. Sample amount

Typically, powder sample is loaded to the neck of a 2 cc-capacity sample holder. To secure reproducibility of the data, around 300 to 800 mg of activated sample was used for high pressure analysis. In general, large pore (pore size 6 - 10 Å) MOF materials have very low density and are highly porous. These materials can be charged around 300 - 400 mg in the sample holder. However for small pore materials with pore size less than 6 Å, at least 500 to 800 mg of activated samples are required.

B. Sample weight measurement

High accuracy in sample weight is crucial for low pressure measurement for it uses only a small amount of sample, ~50-90 mg. As high pressure measurement used ~10 times larger sample amount, it is less crucial, however, accurate sample weight is still very important to obtain accurate hydrogen uptake value. For this study, initially each sample holder was sonicated in acetone bath for half an hour. Then sample holder was washed with fresh acetone three times, followed by drying in the vacuum oven at 50°C for half an hour. After cooling it down to room temperature, the weight of empty sample holder was measured three times for every 3 minutes. The average was taken to be the weight of the empty sample holder. The sample weight was obtained by weighing the sample with holder immediately after activation. The completion of the activation was achieved by monitoring vacuum level to reach a pressure below 10^{-6} mbar and weight loss based on the TGA data.

C. Shape of the sample

As described in the sample preparation section, all of the samples were single crystals. Initially, powders of samples were pressed into pellet to prevent clogging of gas tube line. About 250 mg of sample was made into pellet with 2~3 metric tons of pressure (Carver Press). However, it dramatically decreased hydrogen uptake capacity, as shown in Figure 4.5. Therefore, powder sample was used and a filter (60 micron mesh) was placed between the sample holder and manifold.

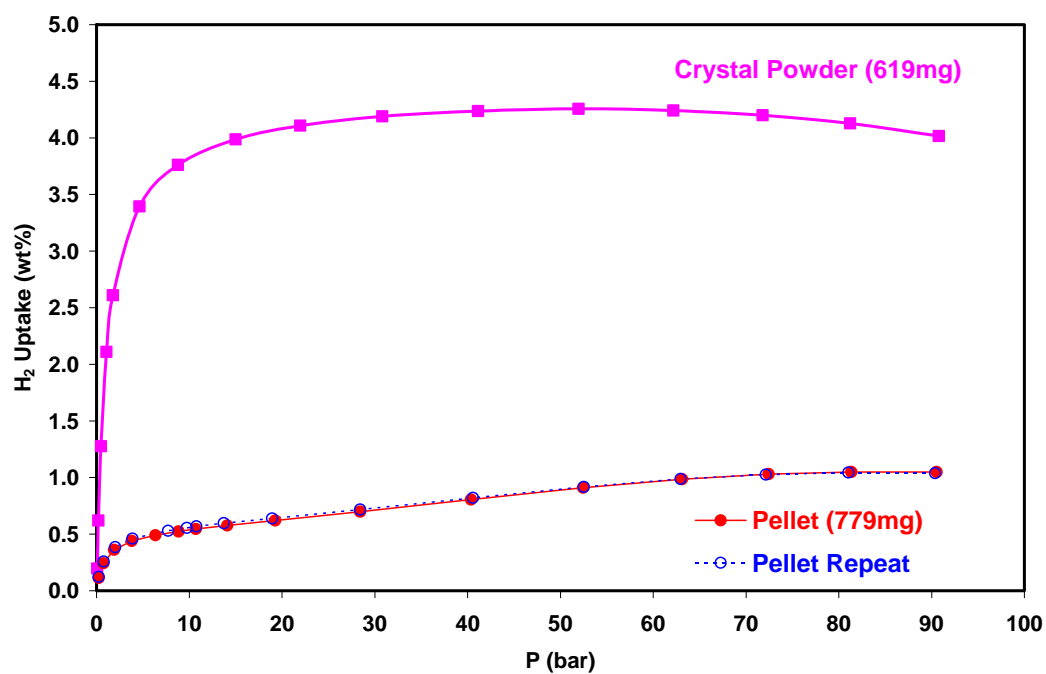


Figure 4.5 Effect of sample shape on hydrogen isotherm on $[\text{Zn}(\text{bdc})(\text{ted})_{0.5}]$ at 77 K.

D. Equilibrium time

As the samples were prepared as single crystals and have an average size of $\sim 0.1 \times 1$ mm, adequate equilibrium time was sought to find optimal conditions. Because 3 ~ 4 minutes of equilibrium time was used for low pressure measurement, 5 and 10 minute condition were tested for high pressure measurement and the results are shown in Figure 4.6. The saturation values of each isotherm were the same for both conditions on crystals of Cu-BTC (**5**). The saturation was reached at relatively low pressure with longer equilibrium time.

A same experiment was performed on relatively larger pore (~ 9.6 Å) material such as [Ni(ndc)(ted)_{0.5}]. As shown in Figure 4.6 (bottom), 5 minute equilibrium shows relatively lower isotherm values than those of 10 and 15 minute condition isotherms up to 70 bar. However, there was no big difference in the saturation value between 5 minute (5.36 wt%) and 15 minute condition (5.35 wt%), even though 10 minute condition shows highest saturation value (5.48 wt%). Therefore, 5 to 15 minute equilibrium condition was used depend on the pore size. In general, small pore materials and bigger crystals require longer equilibrium time.

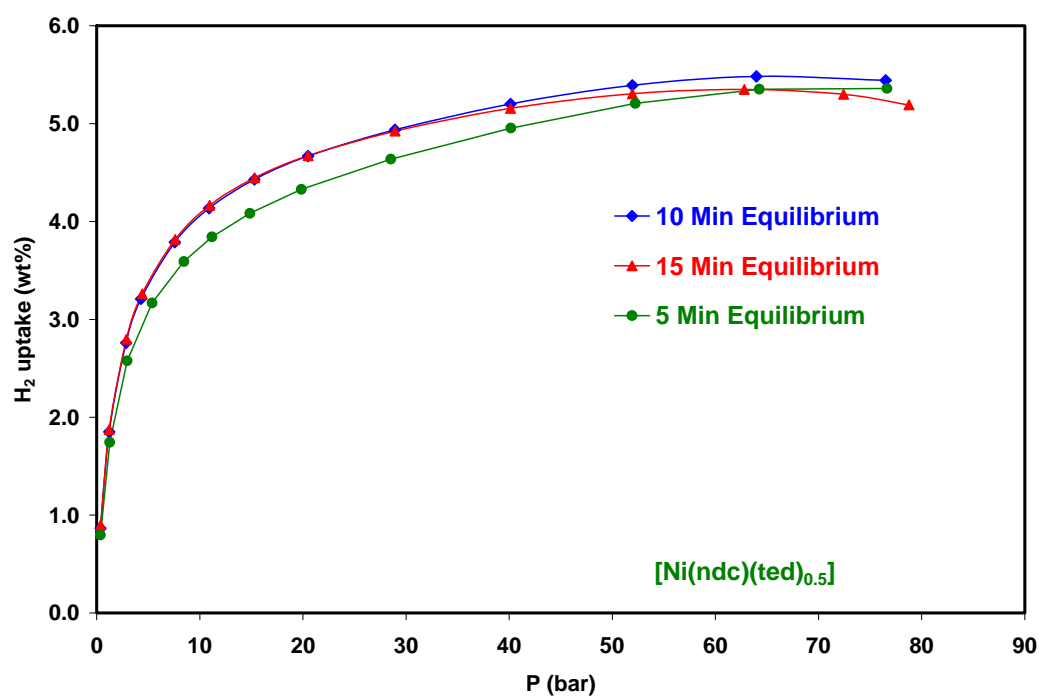
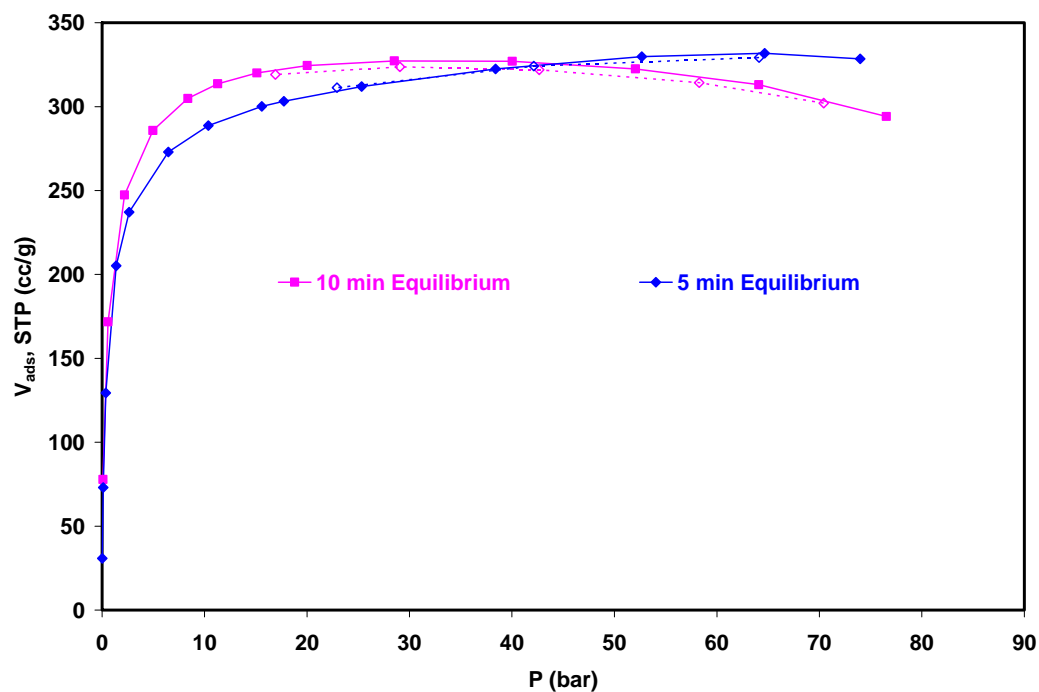


Figure 4.6 Effect of equilibrium time on hydrogen isotherm on Cu-BTC (top) and $[\text{Ni}(\text{ndc})(\text{ted})_{0.5}]$ (bottom) at elevated pressure. (Solid marks for adsorption and open marks for desorption)

4.3 Results and Discussion

The high pressure hydrogen adsorption-desorption isotherms on selected materials were collected at 77 K, 87 K and room temperature. The result was shown in Table 4.3.

Table 4.3 The hydrogen uptake at elevated pressure and different temperatures.

<i>materials</i>	<i>Gravimetric uptake (wt%)</i>			<i>Volumetric uptake (g/L)</i>		
	<i>77K</i>	<i>87K</i>	<i>RT</i>	<i>77K</i>	<i>87K.</i>	<i>RT</i>
1	2.29	2.10	0.46	25	23	5
2	2.39	2.29	0.49	28	27	6
3	0.56	-	-	9	-	-
5	2.95	-	0.49	26	-	4
8	4.06	3.70	0.53	36	33	5
9	3.91	3.73	0.72	32	31	6
12	5.48	4.72	0.78	-	-	-
13	1.31	1.06	0.22	19	16	3

As illustrated in Figure 4.7, most of the isotherms were saturated around 40 bar, but the isotherm of **12** showed saturation around 70 bar. As **12** has larger pore and 20 % larger pore volume than that of **9**, it required higher pressure for saturation. However, no saturation was observed in the small pore material, **3**. Because of the relatively low free space (~12 %) and small size pore (~3.5 Å), compound **3** could take 0.56 wt% of hydrogen around 70 bar. All isotherms showed no hysteresis over the entire pressure range which confirms fast adsorption and desorption by physisorption. As **1** and **2** have very similar structure, their capacities of hydrogen uptake are also similar, 2.29 wt% for **1** and 2.39 wt% for **2**, respectively. As expected, larger pore materials **5**, **8** and **9** showed higher hydrogen uptake than **1** and **2**, and the observed value was 2.95 wt% for **5**.

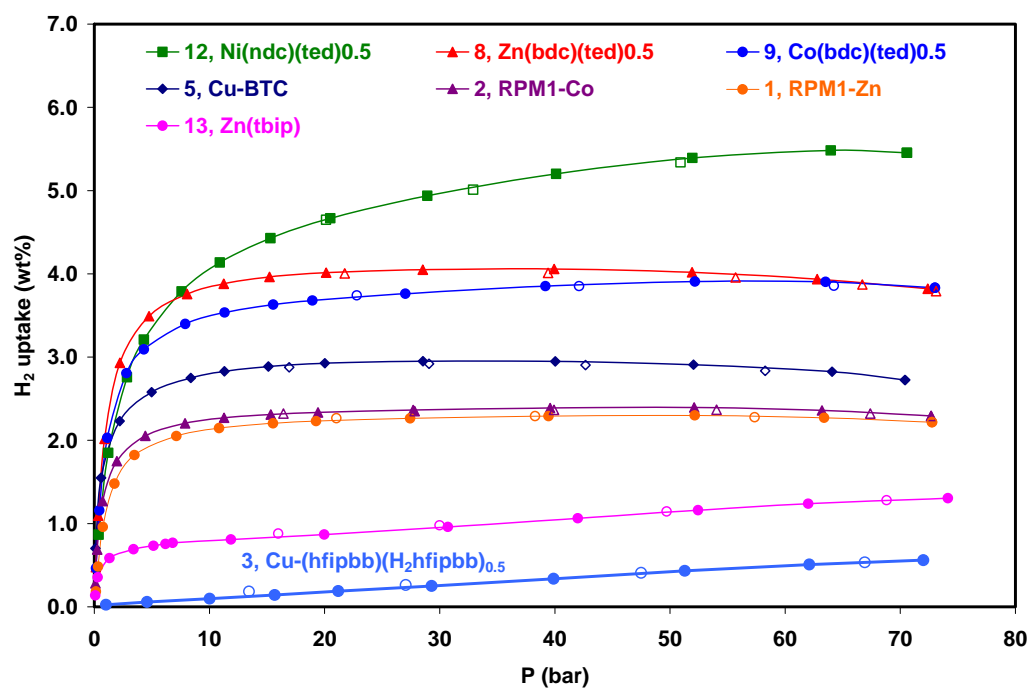


Figure 4.7 High pressure hydrogen isotherms at 77 K on selected MOF materials in gravimetric scale (wt%) as a function of pressure. Solid symbols denote adsorption isotherm and empty markers represent desorption. The solid line is provided for eye guidance.

For the same reason, isostructural **8** and **9** showed very similar results, 4.06 wt% for **8** and 3.91 wt% for **9**, respectively. There was small difference of isotherm behavior of **8** and **9** below 40 bar, and it may be explained as relatively higher free volume (59.2 % of unit cell volume) of **9** than that of **8** (56.7 % unit cell volume).

The highest hydrogen uptake was observed with $[\text{Ni}(\text{ndc})(\text{ted})_{0.5}]$ (**12**) and the saturation value of hydrogen is 5.48 wt% at around 60 bar. This is one of the highest values of hydrogen uptake among the reported value and the saturation was observed at relatively lower pressure than reported values at around 70 ~ 90 bar.^{4, 5}

Because of the practical limit of the tank volume to store hydrogen gas, the volumetric capacity is as important as gravimetric density and was also studied on the same samples. This volumetric uptake of hydrogen in the same samples are plotted in Figure 4.8, along with a simulated isotherm (green dashed line) for **12** using the density of activated crystal of **9** (the crystallographic density of **12** is not available at this point).

Interesting volumetric uptake results were observed with crystal **8** and **9** and the values were 36 g/L and 32 g/L, respectively. 36 g/L is the second highest value among the reported values, thus far (34 g/L for IRMOF-20 and 60 g/L for Mn-MOF).^{4, 5} The volumetric uptake on **12** was simulated to be less than 45 g/L shown in Figure 4.8. Although the low pressure (1 atm) uptake (1.7 wt%) of **12** was lower than those (2.1 wt%) of **8** and **9**, highest gravimetric uptake was observed with compound **12** at elevated pressure. Therefore, it is proposed that the evaluation of the hydrogen storage capability should be made using both gravimetric and volumetric capacity at elevated pressure condition at the same time.

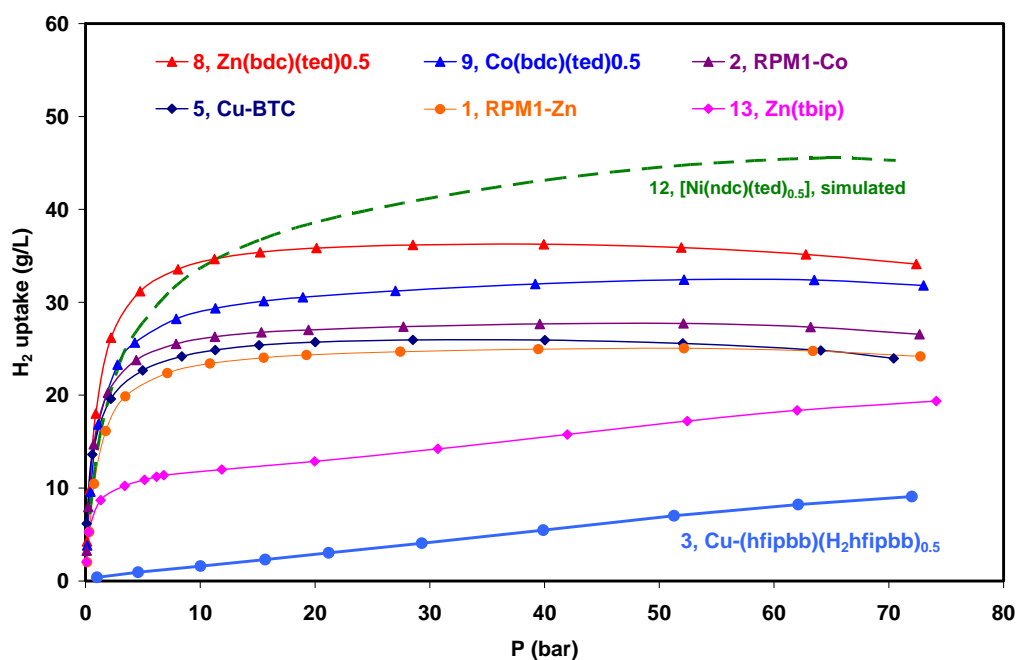


Figure 4.8 High pressure hydrogen adsorption isotherms at 77K on selected MOF materials in volumetric uptake (g/L) as a function of pressure. For dashed green line is simulated volumetric isotherm for **12** using activated density of **9** for comparison purpose.

The room temperature hydrogen sorption ability of the same MOF materials was also evaluated and illustrated in Figure 4.9. All adsorption isotherms show a linear dependence on pressure up to 70 bar and no saturation is observed. Among very few reported values at room temperature, one reproducible result is 0.4wt % on MOF-5,^{6,7} in comparison with 0.39 wt% based on this study. Two MOF structures, **9** and **12**, show higher values 0.72 wt% and 0.78 wt%, respectively. Other structures show 0.46 - 0.53 wt% of room temperature hydrogen uptake and small pore crystal **13** takes only 0.2 wt%. Although the gravimetric uptake for **12** at 298 K is only 0.78 wt%, it is twice of that of MOF-5.

One of the important but unexplored characteristics to utilize hydrogen on MOF materials is a cycle life property. The cycle ability on hydrogen sorption at high pressure and 77K condition was performed on [Zn(bdc)(ted)_{0.5}] as shown in Figure 4.10. For cycle property, adsorption/desorption isotherm was obtained up to 40bar for saturation isotherm. And the highest point in the every adsorption isotherm was taken to represent each cycle. No outgassing was conducted between the cycles. The initial hydrogen uptake value of compound **8** was 4.00 wt% which is reproducible for 4.06 wt% on the same compound. (see Table 4.3) No severe capacity drop was observed up to 30 cycles and 98% of initial capacity was maintained.

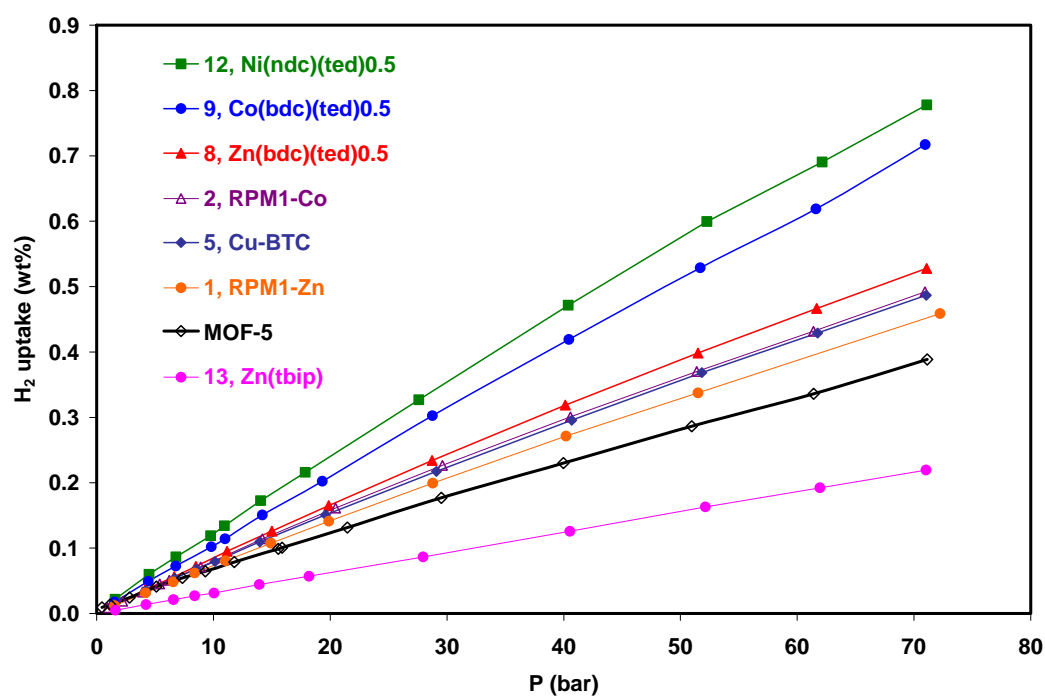


Figure 4.9 High pressure hydrogen adsorption isotherms at 298 K on selected MOF materials in gravimetric scale (wt%) as a function of pressure. Solid symbols denote adsorption isotherm. The solid line is provided for eye guidance.

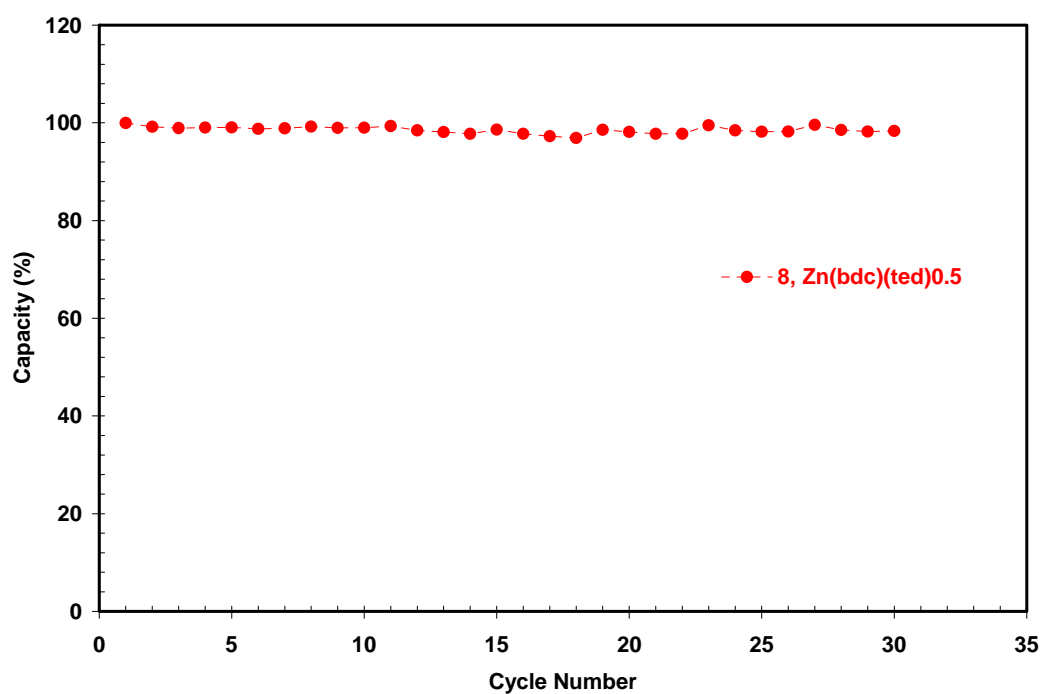


Figure 4.10 High pressure dihydrogen sorption at 77 K as a function of the number of adsorption/desorption cycles. One cycle is a set of adsorption-desorption isotherm. Each point represent maximum uptake in adsorption isotherm

High pressure methane adsorption properties were evaluated at 298 K on these selected MOF materials and the results are depicted in Figure 4.11 (top). All methane adsorption isotherms follow Langmuir behavior and no hysteresis was observed in the pore range of 6-9 Å. The high amount of methane adsorbed per weight around 40 bar is increase with pore size from 5.5 Å to 7.8 Å in **8** and decreased with larger pore size 9.3Å in **12** indicating good agreement of optimal pore size for methane storage is ~8 Å.^{8, 9}

The observed value for **8** is 242 cc/g at 42 bar (or 17.3 wt%) as high as the highest reported value, 240 cc/g at 36 atm, on IRMOF-6¹⁰ and 271 cc/g at 35 bar simulated on IRMOF-14.¹¹ On the basis of gravimetric uptake, the amount of methane stored in **8**, 17.3 wt% at 42 bar, corresponds with almost double amount of methane stored in the compressed cylinder, 9.9 wt% at 165 bar, under relatively low pressure. This result of methane adsorption study shows that MOFs are indeed promising candidates as storage media. The methane uptakes of selected MOFs are also compared in Figure 4.11(bottom) with room temperature hydrogen uptake of **8**, which indicates excellent capability of separation between H₂ and CH₄ gases.

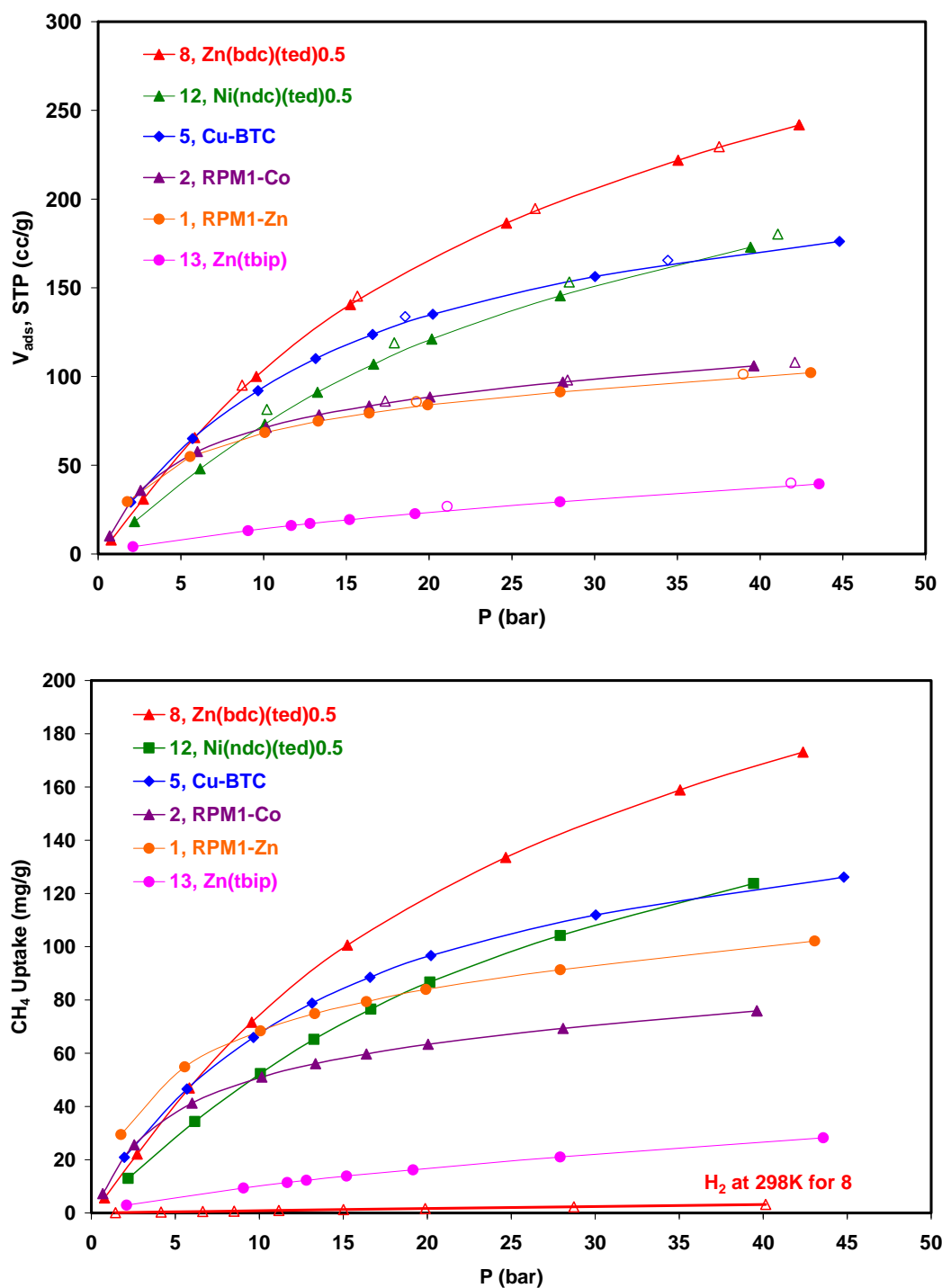


Figure 4.11 High pressure methane isotherms at 298K in volumetric scale (STP, cc/g, top) and their separation capability (mg/g, bottom). A thick red line in the bottom plot indicate hydrogen uptake on 8 at 298K. Solid symbols denote adsorption isotherm and empty markers represent desorption. The solid line is provided for eye guidance.

4.4 Conclusions

High pressure hydrogen and methane sorption studies were successfully conducted on selected MOF materials and modified synthetic procedure for gram scale sample production. High gravimetric hydrogen uptake, 5.48 wt%, is achieved at 77K and ~60 bar for **12** and thus far, second highest volumetric uptake, 36 g/L, also observed for **8** at the same temperature. The saturation values of hydrogen uptakes show strong correlation with surface area. Crystals of **8** exhibit highest methane storage capability at 298K, as well as separation capability between hydrogen and methane gas, as several other selected MOF materials.

4.5 References

1. Ogden, J. M., Prospects for building a hydrogen energy infrastructure. *Annual Review of Energy and the Environment* **1999**, 24, (1), 227-279.
2. Ritter, J. A.; Ebner, A. D.; Wang, J.; Zidan, R., Implementing a hydrogen economy. *Materials Today* **2003**, 6, (9), 18-23.
3. Züttel, A., Materials for hydrogen storage. *Materials Today* **2003**, 6, (9), 24-33.
4. Wong-Foy, A. G.; Matzger, A. J.; Yaghi, O. M., Exceptional H₂ Saturation Uptake in Microporous Metal-Organic Frameworks. *J. Am. Chem. Soc.* **2006**, 128, (11), 3494-3495.
5. Dinca, M.; Dailly, A.; Liu, Y.; Brown, C. M.; Neumann, D. A.; Long, J. R., Hydrogen Storage in a Microporous Metal-Organic Framework with Exposed Mn²⁺ Coordination Sites. *J. Am. Chem. Soc.* **2006**, 128, (51), 16876-16883.
6. Li, Y.; Yang, R. T., Significantly Enhanced Hydrogen Storage in Metal-Organic Frameworks via Spillover. *J. Am. Chem. Soc.* **2006**, 128, (3), 726-727.
7. Panella, B.; Hirscher, M.; Pütter, H.; Müller, U., Hydrogen Adsorption in Metal-Organic Frameworks: Cu-MOFs and Zn-MOFs Compared. *Adv. Funct. Mater.* **2006**, 16, (4), 520-524.
8. Cracknell, R. F.; Gordon, P.; Gubbins, K. E., Influence of pore geometry on the design of microporous materials for methane storage. *J. Phys. Chem* **1993**, 97, (2), 494-499.
9. Matranga, K. R.; Stella, A.; Myers, A. L.; Glandt, E. D., Molecular Simulation of Adsorbed Natural Gas. *Separation Science and Technology* **1992**, 27, (14), 1825 - 1836.
10. Eddaoudi, M.; Kim, J.; Rosi, N.; Vodak, D.; Wachter, J.; O'Keeffe, M.; Yaghi, O. M., Systematic design of pore size and functionality in isorecticular MOFs and their application in methane storage. *Science* **2002**, 295, (5554), 469-72.
11. Düren, T.; Sarkisov, L.; Yaghi, O. M.; Snurr, R. Q., Design of New Materials for Methane Storage. *Langmuir* **2004**, 20, (7), 2683-2689.

CHAPTER FIVE

SUMMARY OF THE STUDY

This study has demonstrated a synthesis of metal-organic frameworks and their tunable pore property and permanent porosity with low and high pressure gas sorption study. At low pressure high resolution argon and hydrogen sorption studies show that reversible hydrogen adsorption/desorption is achieved with larger than 6 Å size pore.

As shown in Figure 5.1, hydrogen uptake increases as a function of pore size and surface area. It is also provided evidence of capability of hydrogen storage in terms of gravimetric and volumetric uptake at low temperature. In addition, it is also presented ~60% of high porosity in MOF and separation capability of between methane and hydrogen gas. The interaction between hydrogen and MOF materials is analyzed in terms of isosteric heat of adsorption and it is proved that physisorption is main driving force of hydrogen adsorption on the surface of MOF materials.

However, the high hydrogen uptake is achieved at only cryogenic temperatures and room temperature performance of hydrogen storage is still far below than DOE targets. As the result of high pressure research in this area is limitedly conducted thus far and still at an early stage, it will be continued to comprehensive understanding of the hydrogen behavior in metal-organic frameworks.

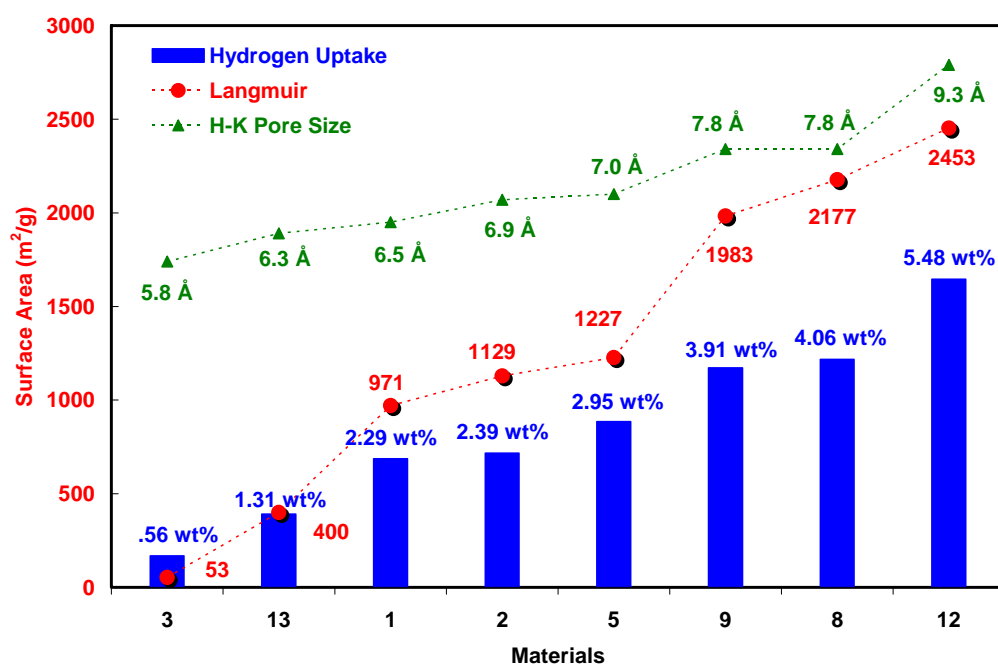


Figure 5.1 The summary of correlation between hydrogen uptake, pore size and surface area based on argon sorption studies at 87 K and high pressure hydrogen studies at 77 K.

APPENDICES

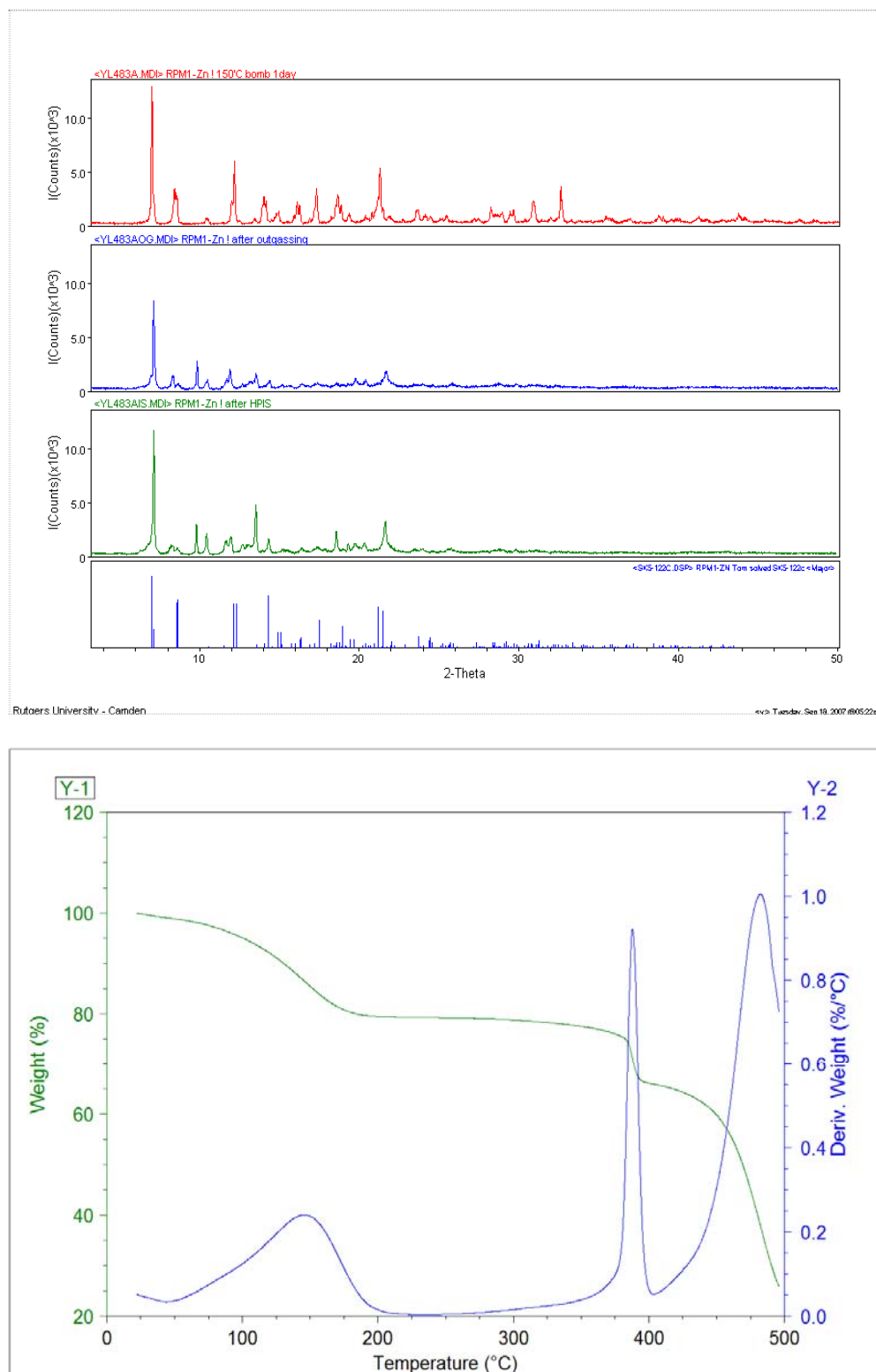


Figure A.1 (Top) The PXRD pattern of **1** depends on experimental stages; as made (red), after outgassing (blue) and after high pressure isotherms (green) comparing with simulated peak . (Bottom) The TG and derivative curve of **1**.

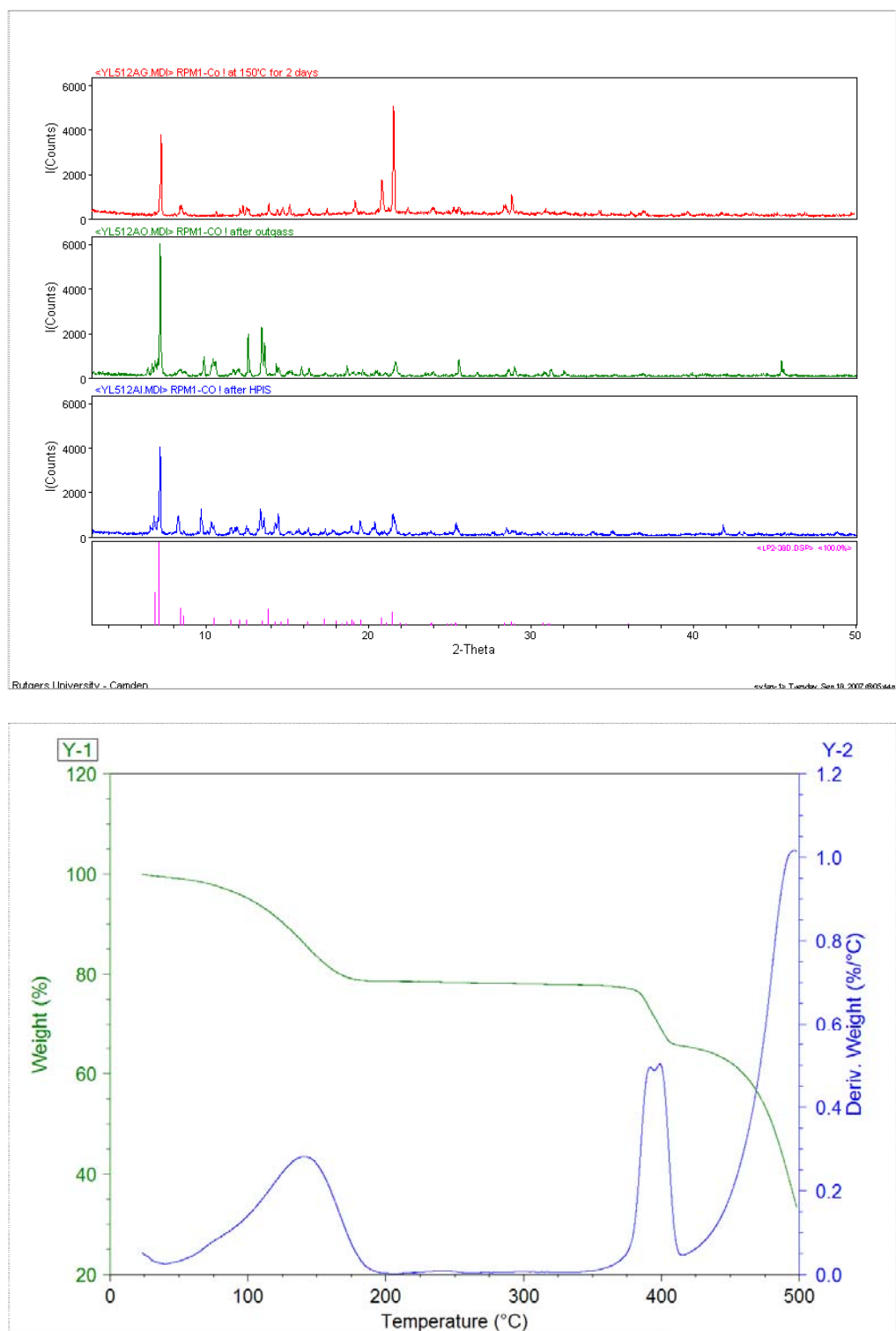


Figure A.2 (Top) The PXRD pattern of **2** depends on experimental stages; as made (red), after outgassing (green) and after high pressure isotherms (blue) comparing with simulated peak . (Bottom) The TG and derivative curve of **2**.

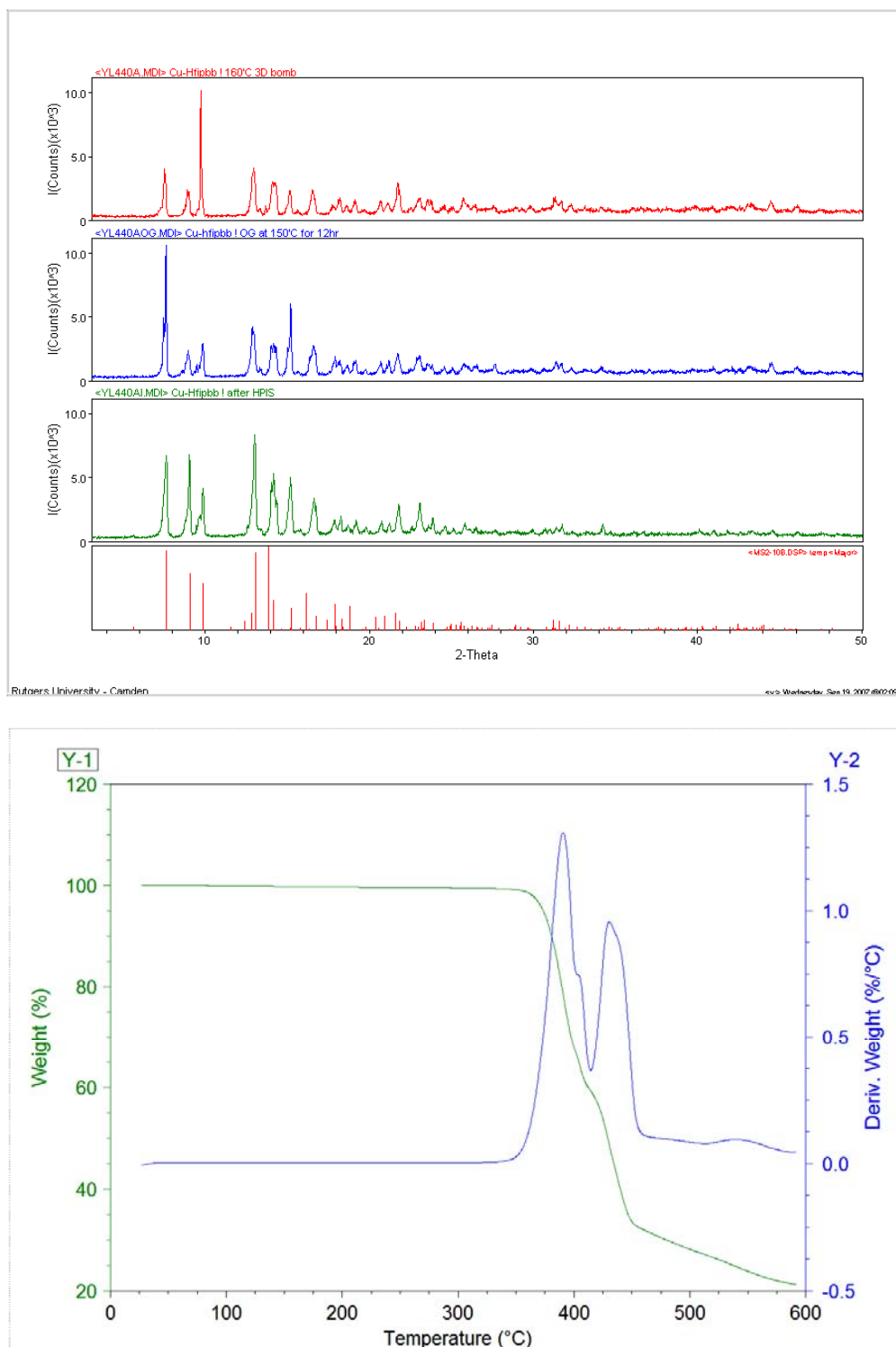


Figure A.3 (Top) The PXRD pattern of **3** depends on experimental stages; as made (red), after outgassing (blue) and after high pressure isotherms (green) comparing with simulated peak. (Bottom) The TG and derivative curve of **3**.

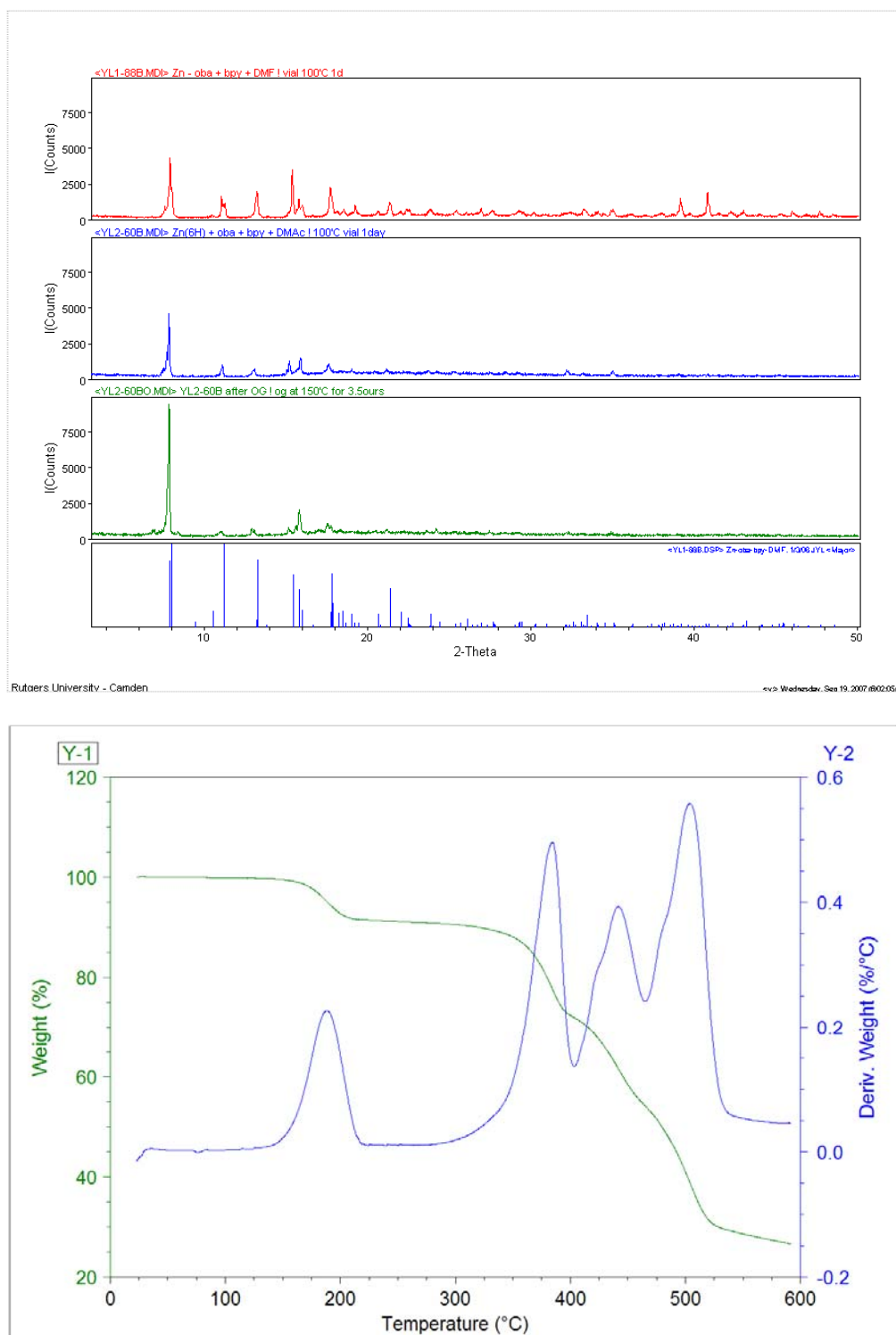


Figure A.4 (Top) The PXRD pattern of **4** depends on experimental stages; as made (red, **4** and blue, **4'**), after outgassing (green) comparing with simulated peak. (Bottom) The TG and derivative curve of **4**.

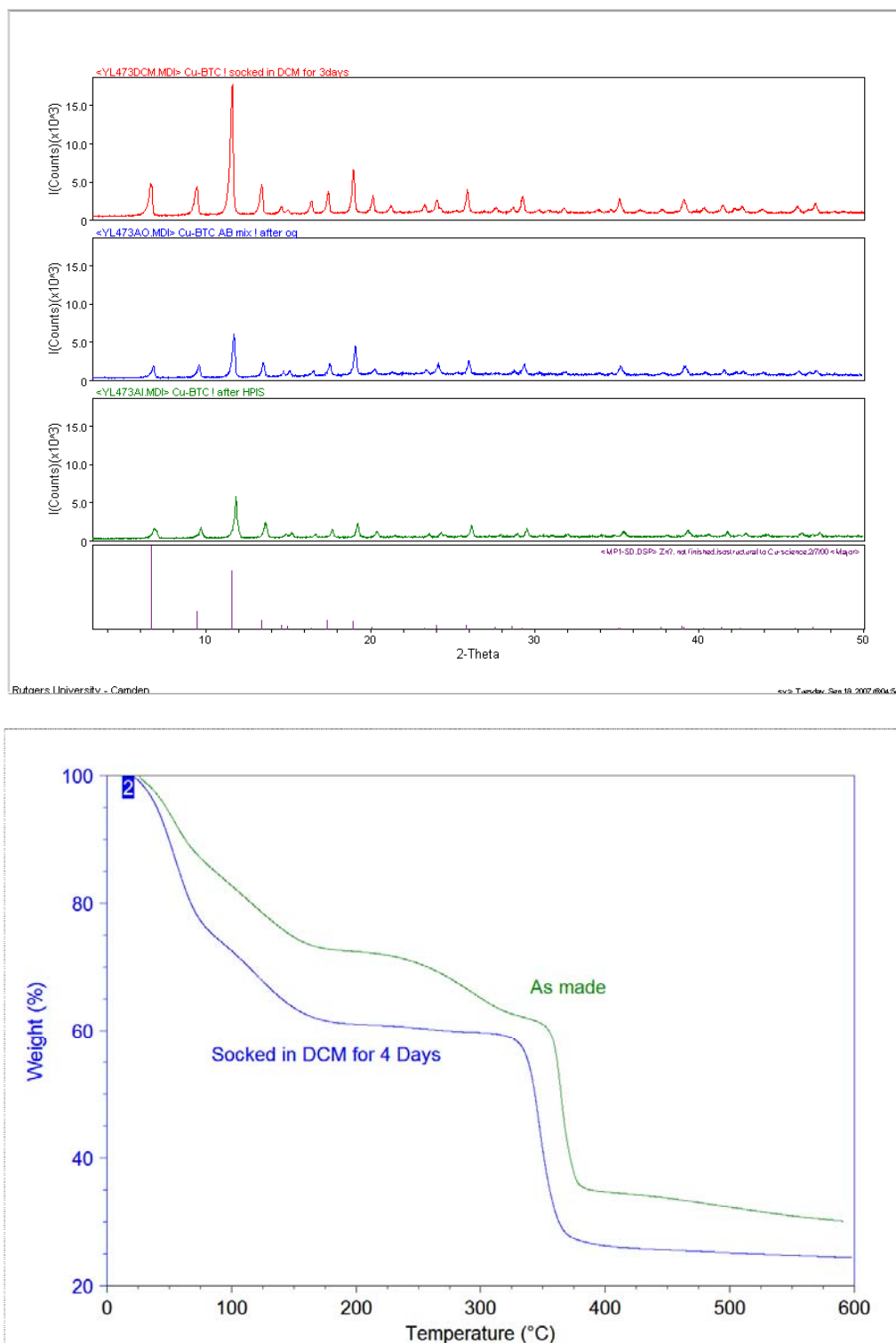


Figure A.5 (Top) The PXRD pattern of **5** depends on experimental stages; as made in DCM (red), after outgassing (blue) and after high pressure isotherms (green) comparing with simulated peak . (Bottom) The TG curve of **5** and after solvent exchange with DCM for four days.

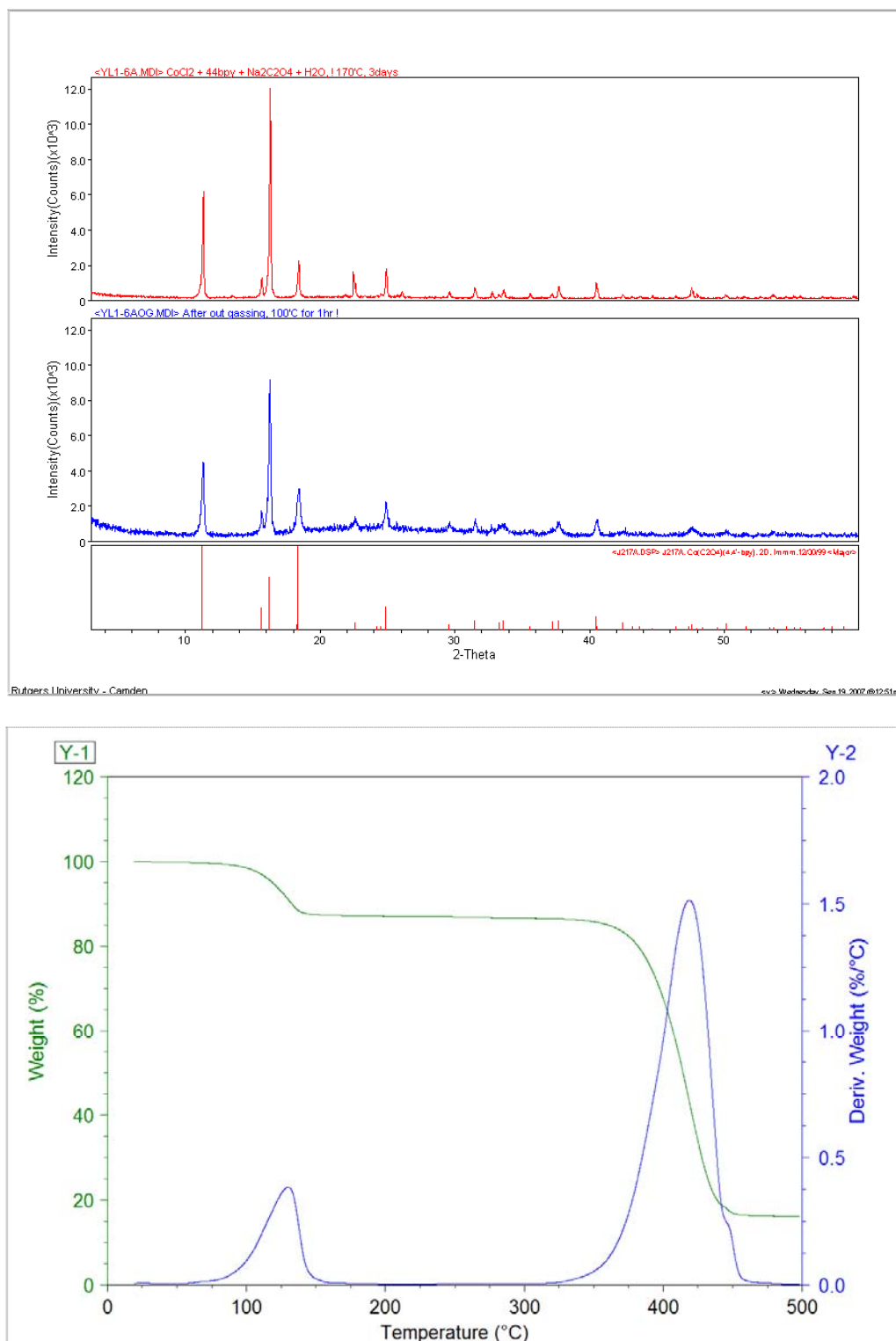


Figure A.6 (Top) The PXRD pattern of **6** depends on experimental stages; as made (red) and after outgassing (blue) comparing with simulated peak . (Bottom) The TG and derivative curve of **6**.

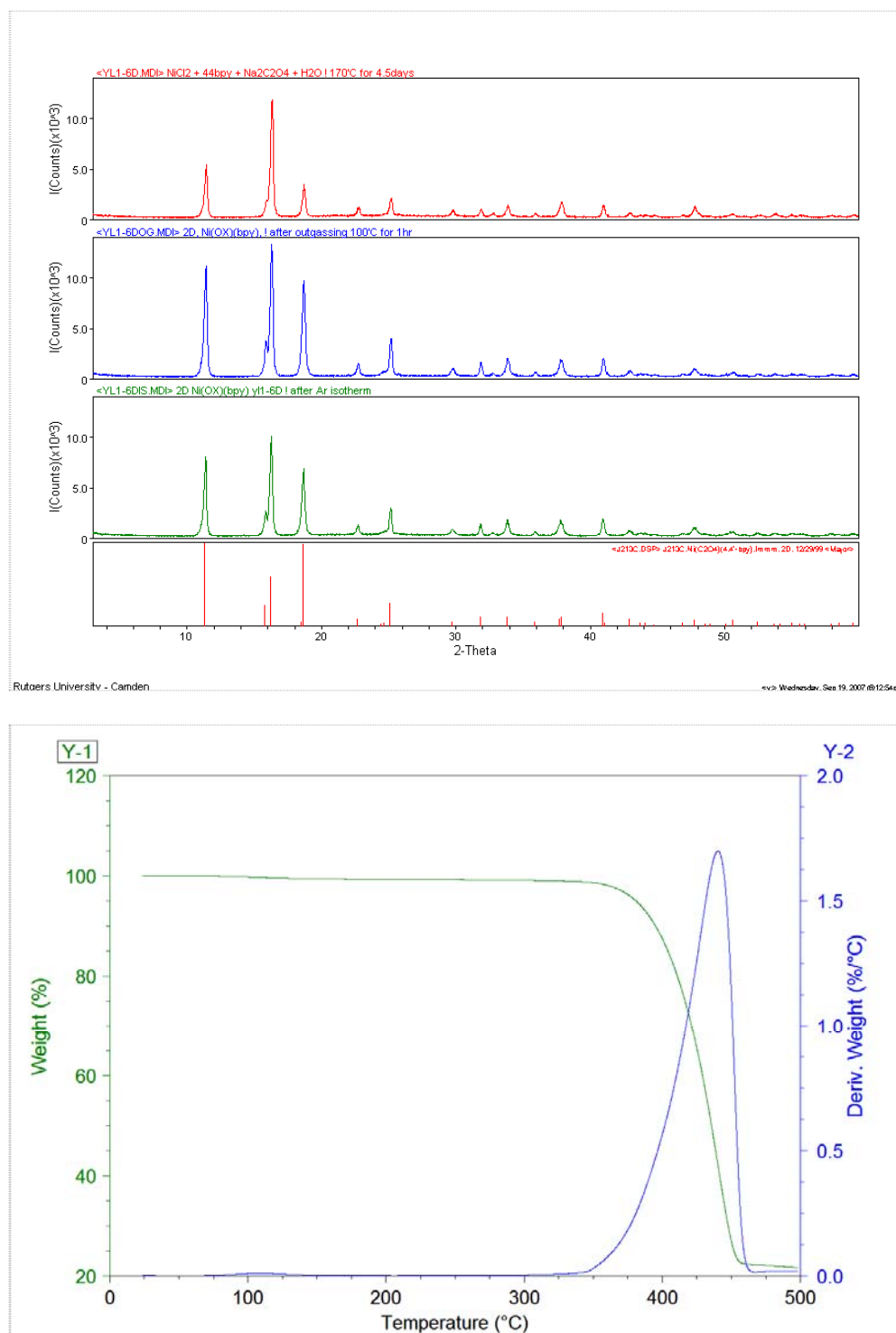


Figure A.7 (Top) The PXRD pattern of **7** depends on experimental stages; as made (red), after outgassing (blue) and after isotherms (green) comparing with simulated peak . (Bottom) The TG and derivative curve of **7**.

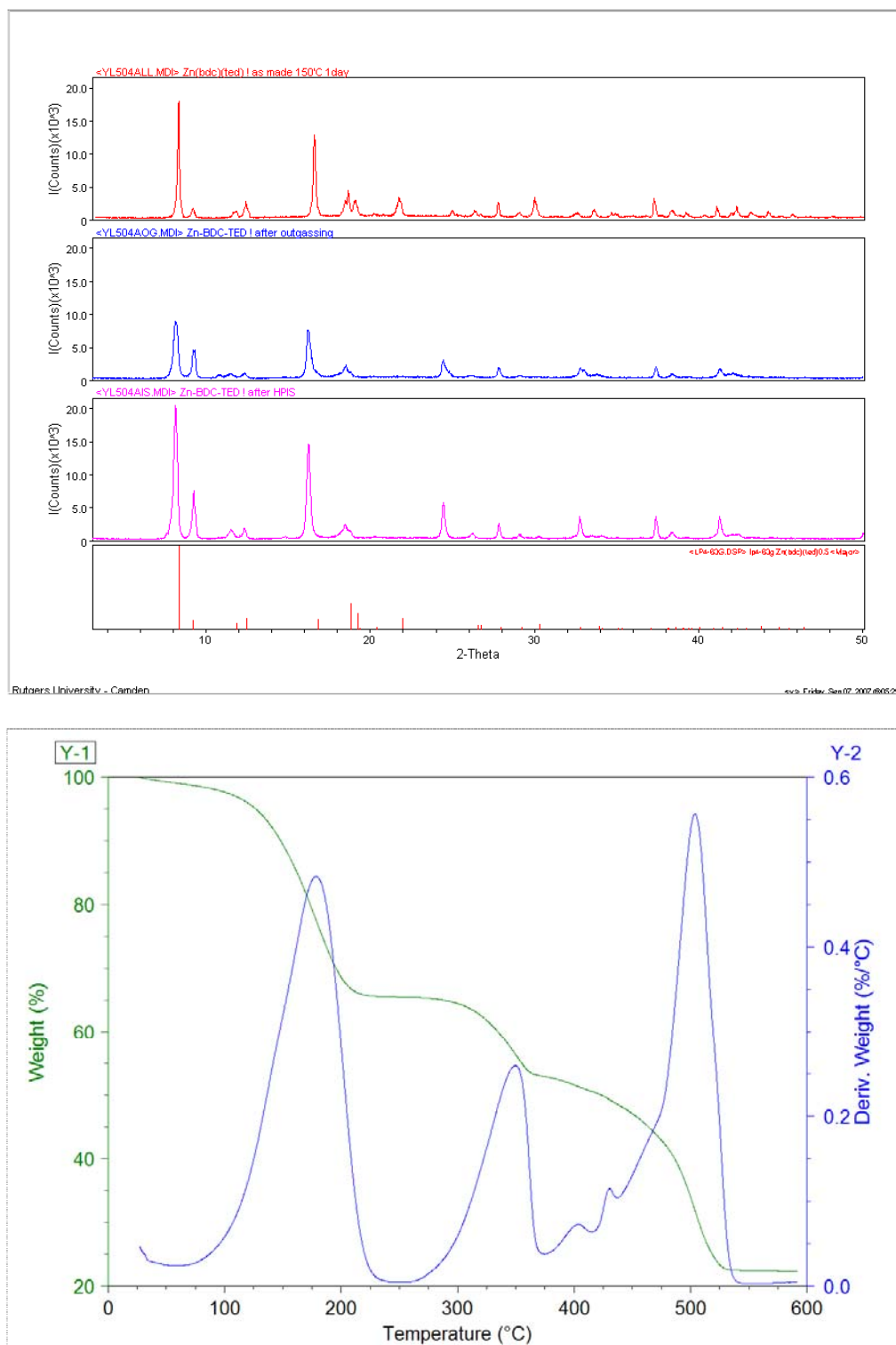


Figure A.8 (Top) The PXRD pattern of **8** depends on experimental stages; as made (red), after outgassing (blue) and after high pressure isotherms (pink) comparing with simulated peak. (Bottom) The TG and derivative curve of **8**.

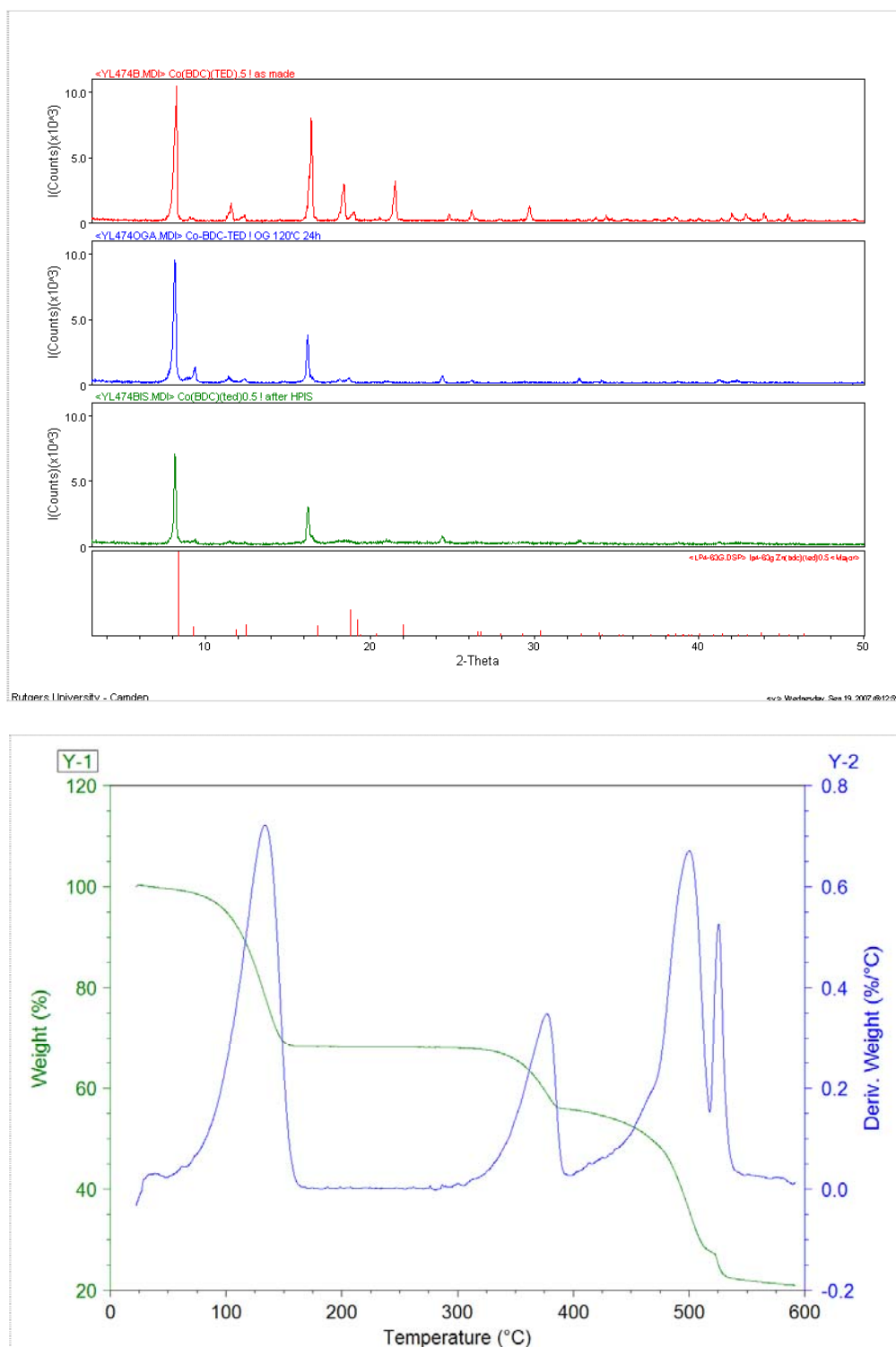


Figure A.9 (Top) The PXRD pattern of **9** depends on experimental stages; as made (red), after outgassing (blue) and after high pressure isotherms (green) comparing with simulated peak . (Bottom) The TG and derivative curve of **9**.

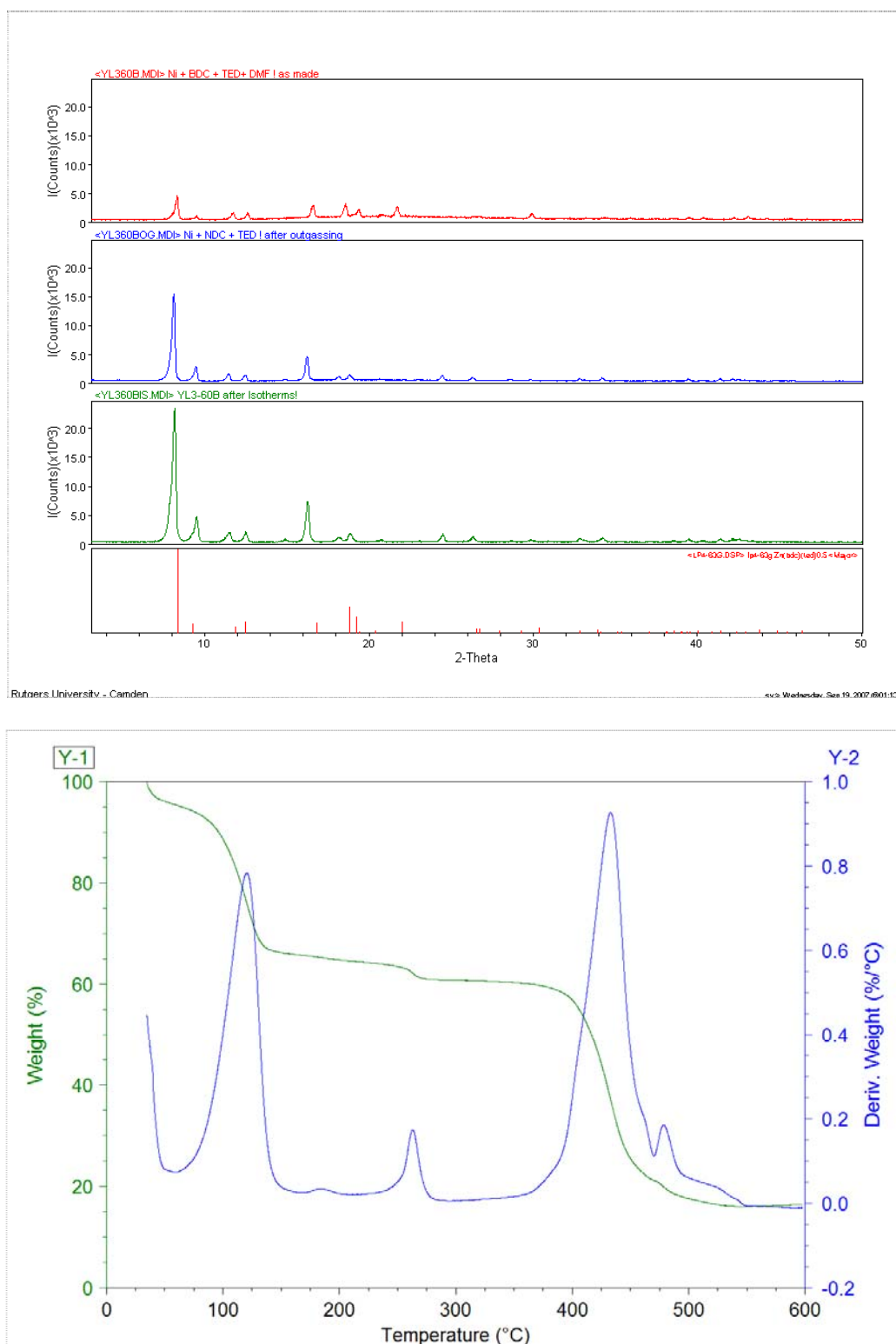


Figure A.10 (Top) The PXRD pattern of **10** depends on experimental stages; as made (red), after outgassing (blue) and after isotherms (green) comparing with simulated peak. (Bottom) The TG and derivative curve of **10**.

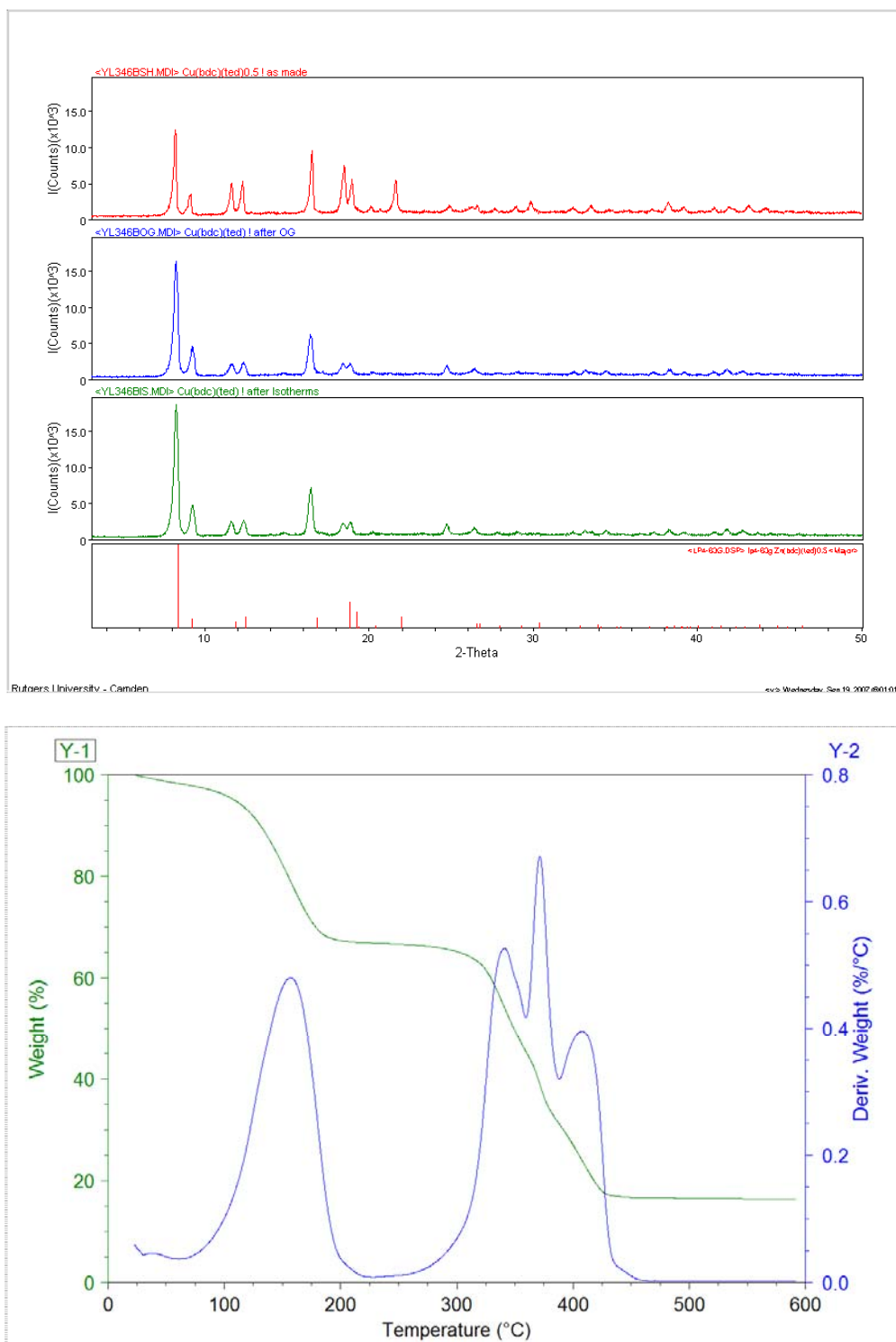


Figure A.11 (Top) The PXRD pattern of **11** depends on experimental stages; as made (red), after outgassing (blue) and after high pressure isotherms (green) comparing with simulated peak . (Bottom) The TG and derivative curve of **11**.

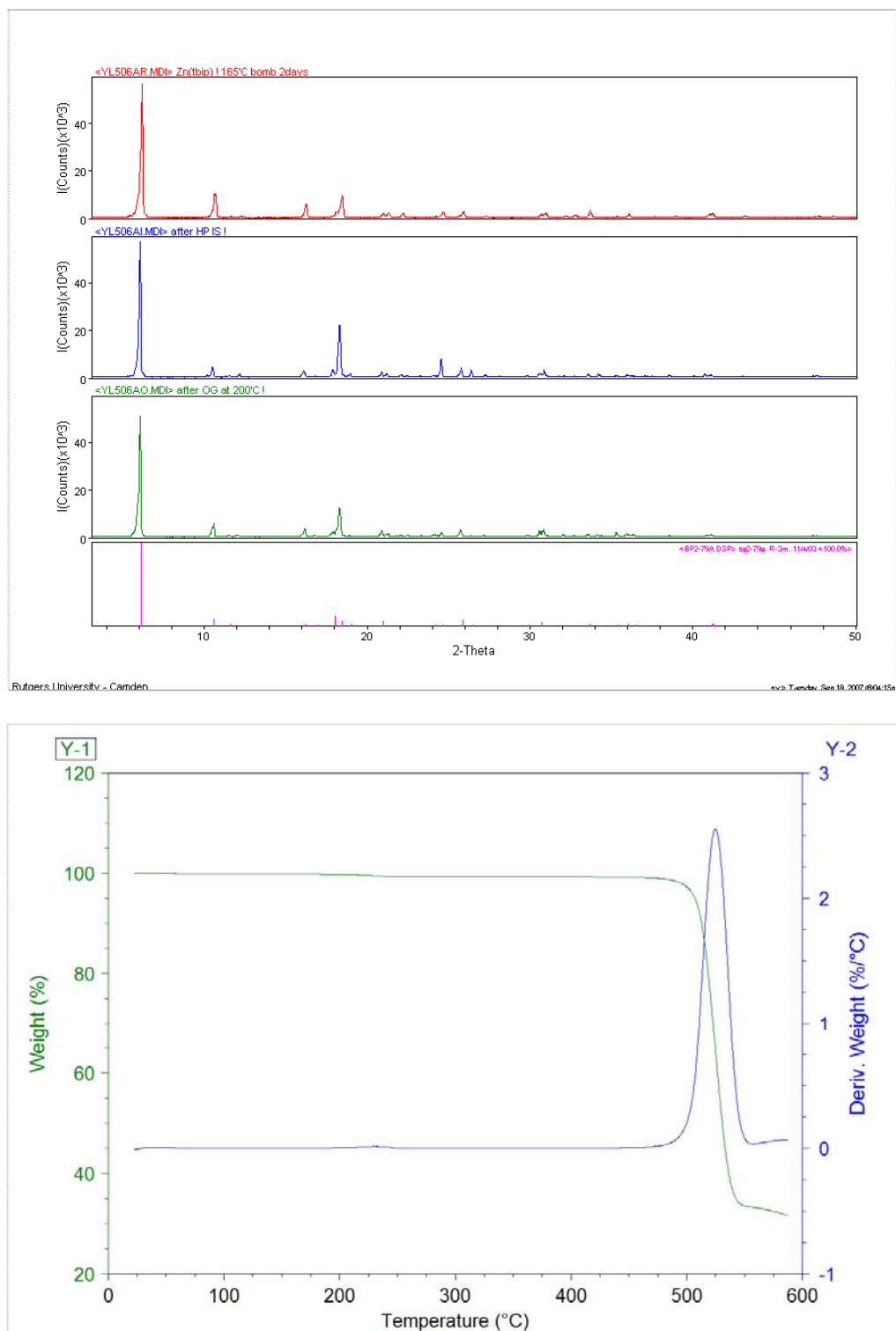


Figure A.12 (Top) The PXRD pattern of **13** depends on experimental stages; as made (red), after outgassing (blue) and after high pressure isotherms (green) comparing with simulated peak. (Bottom) The TG and derivative curve of **13**.

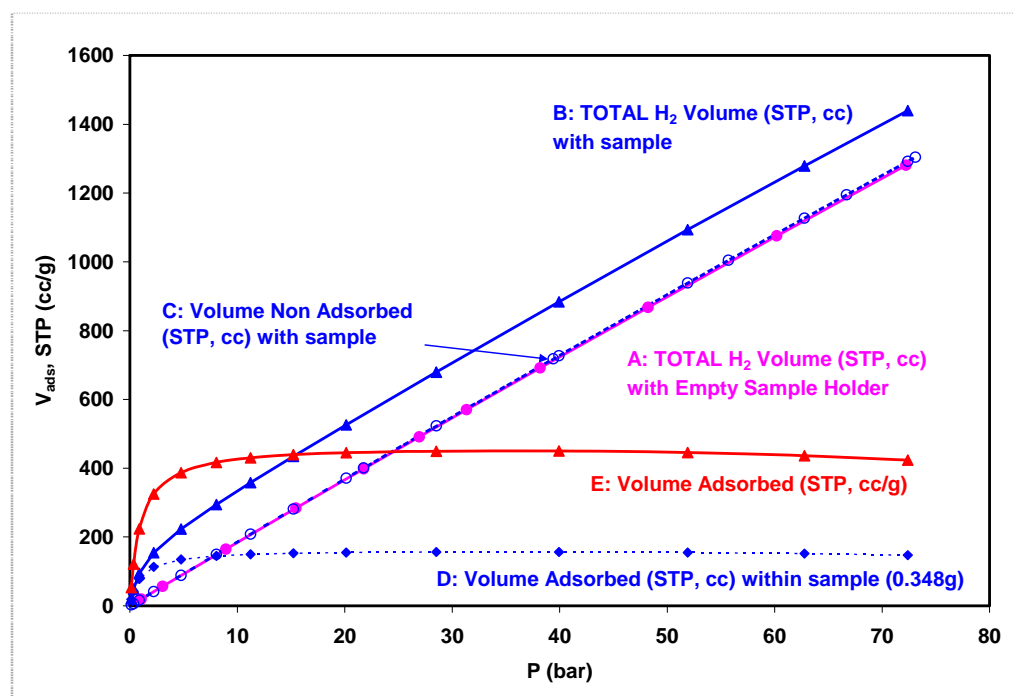


Figure A.13 The proof of hydrogen uptake by the porous MOF structure, $[\text{Zn}(\text{bdc})(\text{ted})_{0.5}]$, compared with amount of compressed hydrogen in the empty sample holder at 77K. A is the amount of hydrogen stored in the empty sample holder. B is the total amount of hydrogen stored in the MOF and empty space of the sample holder. C is the amount of the hydrogen stored in the dead space not occupied by MOF materials. D is the actual amount of hydrogen stored in the MOF materials ($D = B - C$). E is the hydrogen uptake per gram sample, STP, cc/g.

CURRICULUM VITA

Jeongyong Lee

EDUCATION AND EXPERIENCE

- 2002~2007 Ph.D. in Chemistry, Department of Chemistry and Chemical Biology
Rutgers, The State University of New Jersey, New Brunswick, USA
- 1996~2001 Researcher/Assistant Manager
R&D in Mobile Energy Team at SAMSUNG SDI Co. LTD., KOREA
- 1994~1996 M.S. in Chemistry
Department of Chemistry, Yonsei University, Korea
- 1987~1994 B.S. in Chemistry
Department of Chemistry, Yonsei University, Korea
- 1989~1991 A Sergeant (Military Service)

ACADEMIC HONORS AND AWARDS

- Chemistry Departmental Fellowship Award at Rutgers University in 2006~2007
- Raid Graduate Fellowship Award at Rutgers University in 2005~2006
- Best practice award in R&D at SAMSUNG SDI Co. in 1998
- Best Teaching Assistant award in the Graduate School at Yonsei University in 1995
- 4-Year full scholarship at Chemistry Department in Yonsei University in 1987.

PUBLICATIONS

- **J. Y. Lee**, D. H. Olson, L. Pan, T. J. Emge and J. Li, “ Microporous Metal Organic Frameworks with High Gas Sorption and Separation Capacity”, *Adv. Funct. Mater.* **17** (2007) 1255
- V. Krungleviciute, K. Lask, L. Heroux, A. D. Migone, **J. Y. Lee**, J. Li, and A. Skoulidas, “Argon adsorption on $\text{Cu}_3(\text{BTC})_2(\text{H}_2\text{O})_3$ (BTC=Benzene-1,3,5-tricarboxylate) metal-organic framework”, *Langmuir*, **23** (2007) 3106

- H. Park, J. F. Britten, U. Mueller, **J. Y. Lee**, J. Li, “Synthesis, Structure Determination and Hydrogen Sorption Studies of New Metal-Organic Frameworks using Triazole and Naphthalene dicarboxylic Acid”, *Chem. Mater.*, **19** (2007) 1302
- L. Pan, B. Parker, X. Huang, D. H. Olson, **J. Y. Lee**, J. Li, “Zn(tbip) (H₂tbip= 5-tert-Butyl Isophthalic Acid): A Highly Stable Guest-Free Microporous Metal Organic Framework with Unique Gas Separation Capability”, *J. Am. Chem. Soc.*, **128** (2006) 4180
- **J. Y. Lee**, L. Pan, S.P. Kelly, J. Jagiello, T.J. Emge, J Li, “Achieving High Density of Adsorbed Hydrogen in Microporous Metal Organic Frameworks”, *Advanced Materials*, **17** (2005) 2703
- **J. Y. Lee**, J. Li, and J. Jagiello, “Gas sorption properties of microporous metal organic frameworks”, *Journal of Solid State Chemistry*, **178** (2005) 2527
- L. Pan, N. Ching, X.-Y.Huang, **J. Y. Lee**, J.Li, T.Yuen, and C.L. Lin, and J.Zan, “The Effect of Terminal Ligands on the Dimensionality and Topology of Metal Dicarboxylate Coordination Structures”, *MRS Symposium Proceedings*, **848** (2004) 145-150
- **J. Y. Lee**, G. J. Lee, H. S. Kim, S. H. Lee, D. H. Lee, C. H. Yo, K. H. Kim and K.S.Ahn, “Electrical and magnetic properties of the Sn⁴⁺ substituted spinel ferrite, ZnSn_xFe_{2-4x/3}O₄(0.00 ≤ X ≤ 0.30)”, *Materials Chemistry and Physics*, **52** (1998) 267-271
- H. S. Kim, G. J. Lee, **J. Y. Lee**, D. H. Lee and K. H. Kim, “Processing parameters and bond nature of (Sm_xBi_{1-x})SrCaCuO superconductor”, *Materials Chemistry and Physics*, **49** (1997) 12
- B. C. Kwak, G. J. Lee, **J. Y. Lee**, H. S. Kim, D. H. Lee and K. H. Kim, “Electrical conductivity of the Solid solution xTiO₂+(1-x)Lu₂O₃;0.05≤ x ≤0.15”, *Materials Chemistry and Physics*, **47** (1997), 146-150
- D. H. Lee, H. S. Kim, **J. Y. Lee**, C. H. Yo and K. H. Kim, “Characterization of the magnetic properties and transport mechanisms of Co_xFe_{3-x}Co₄ spinel”, *Solid State Communications*, **96** (1996) 445-449